

Ben-Gurion University of the Negev  
Faculty of Engineering Sciences  
Department of Mechanical Engineering



# Fluid and Charged Particles Flow Under the Influence of an Electric Field

Thesis submitted in partial fulfillment of the requirements  
for the M.Sc. degree

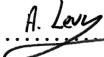
By: Arnon Ratzabi

Supervised by: Prof. Avi Levy

Dr. Yuri Feldman

Author: .....  .....

Date: 30/9/20

Supervisor: .....  .....

Date: 30/9/20

Supervisor: .....  .....

Date: 30/9/20

Chairman of Graduate Studies Committee: .....

Date: 30/9/20

September 2020

## Abstract

The goal of this report is to present the final project conducted in order to fulfill the requirements of the M.Sc. degree at the Department of Mechanical Engineering, Ben-Gurion University (BGU) of the Negev. The project comprises theoretical research investigating the multiphase flow of charged solid particles in an electrolyte subjected to an electric field. The research motivation comes from a number of fundamental problems revealed when operating laser printers produced by the HP Indigo company. The present work is a continuation of Michael Hagayev's project [1], which included a literature survey, formulation of a simplified physical model, and performance of a numerical study simulating the dynamics of an uncharged single phase.

The main objective of this project is to develop a comprehensive numerical methodology that is capable of theoretical multiphase flow modeling under the action of an electric field, by means of standard techniques of computational fluid dynamics. HP-BGU collaboration is planned to continue next year.

This report contains:

- A modular background about HP Indigo's components of interest.
- A comprehensive literature review surveying methods for the simulation of multiphase flow and electrically-driven flow models. Additionally, the literature review includes the theory behind physical phenomena related to electrically-driven flow between two bounding electrodes subjected to an electrical voltage.
- Extended objectives of the performed research.
- A comprehensive two-way coupled physical model, including the governing equations, definitions, constitutive laws, and dimensional analysis.
- A comparison between analytical solutions and results obtained by 2D numerical simulations utilizing a significantly simplified physical model. The considered configurations are: single-phase Couette-Poiseuille flow, two uncharged phases flow, and two-phase flow containing charged particles subjected to a constant electric field.
- A solution of the fully (two-way) coupled physical model utilizing computational fluid dynamics (CFD) software, verification, and electro-osmotic flow characterization of a strongly non-symmetric electrolyte.
- A physical model relevant to the setup used in HP Indigo's laser printers: dimensions, data, assumptions, and simulation results.
- A summary, conclusions, and recommendations for possible future work.

**KEYWORDS:** Electrically-driven flow; Poisson-Nernst-Planck equations; Electroconvection; Electroconvective instability; Symmetric binary electrolyte, Strongly non-symmetric electrolyte.

## Acknowledgements

I would like to take this opportunity to express my immense gratitude to all those who have given their invaluable support and assistance. In particular, I am profoundly indebted to my supervisors, Prof. Avi Levy and Dr. Yuri Feldman, for their professional and knowledgeable support in the physical, computational, and numerical fields. Their great contribution to this research, from their laboratory's computing equipment, through the collaboration process with the HP Indigo company, and to the countless hours of meetings and advice at any time, is remarkable. Especially, I would like to thank Dr. Yuri Feldman for his close supervision during the writing of a scientific manuscript.

My sincere thanks also go to Mr. Tal Eluk from HP Indigo's engineering team. Tal motivated and navigated the project according to Indigo's requirements, managed Indigo's known and unknown data applicable to this study, conducted several sets of experiments that were compared to my simulation results, and was in charge of the HP-BGU weekly meetings and periodic presentations. Besides Tal, I would like to thank the rest of the Indigo members who participated in these periodic presentations, especially Mr. Boaz Tagansky for the verification of several of our simulation results and for his valuable advice.

Additionally, I would like to thank Dr. Yoav Green and Dr. Arik Yochelis who generously contributed their time and assisted me with their theoretical background.

The research for this thesis was financially supported by HP Indigo in addition to a student scholarship provided by the Faculty of Engineering Sciences of Ben-Gurion University of the Negev. These sources of support contributed much to the success of the study.

In this section, I would like to include my colleagues from the Group of Computational Physics Lab founded by my supervisor, Dr. Yuri Feldman, for their discussions and technical support.

It is also appropriate to thank for spiritual support, so I would also like to thank my family and friends for their interest and encouragement along the way. Especially, my dear wife who was always willing to listen and advise throughout the process of accomplishing my master studies.

# Contents

Abstract .....	a
Acknowledgements .....	b
Contents.....	c
List of Figures.....	e
List of Tables.....	h
Nomenclature .....	i
1. Introduction.....	1
2. Background.....	2
2.1 Main Units of LEP Printers .....	4
3. Literature Review .....	8
3.1 Methods for Solving the Multiphase Flows .....	8
3.1.1 Eulerian-Eulerian Method.....	8
3.1.2 Eulerian-Lagrangian Method .....	9
3.1.3 Mixture Method .....	10
3.1.4 Multiphase Flows Solving Methods: Pros and Cons .....	13
3.2 Electrically-Driven Flow (EDF) Models .....	14
3.2.1 Poisson-Nernst-Planck (PNP) Model .....	14
3.2.2 Poisson-Boltzmann (PB) Model .....	15
3.2.3 Debye-Hückel (DH) Model .....	16
3.2.4 EDF Models: Pros and Cons .....	16
3.3 Physical Phenomena Relating to Bounding Electrolyte Subjected to Electric Potential Difference.....	17
4. Research Objectives.....	20
5. The Physical Model .....	21
5.1 Dimensional Analysis .....	24
5.1.1 First Configuration .....	25
5.1.2 Second Configuration.....	26
5.1.3 Non-Dimensional Numbers .....	28
6. Solution of a Simplified Physical Model .....	33
6.1 Analytical Approach .....	33

6.1.1 One Phase Couette-Poiseuille Flow .....	33
6.1.2 Mixture Flow Through a Curved Duct Without the Action of an Electric Field .....	35
6.1.3 Mixture Flow Through a Curved Duct Under the Action of Constant Electric Field Approximated by a Given Expression .....	37
6.2 Numerical Approach .....	39
6.2.1 Ansys Fluent Program .....	41
6.2.2 Comparison Between Analytical and Numerical Results .....	41
7. Solution of the Two-Way Coupled Physical Model .....	45
7.1 CFD Software .....	45
7.2 Verification .....	46
7.2.1 Permselective Membrane-Bulk Configuration .....	48
7.2.2 Two Electrodes Configuration .....	51
7.3 Electro-Osmotic Flow Characterization of a Strongly Non-Symmetric Electrolyte .....	53
7.3.1 Analysis of 1D Configuration .....	54
7.3.2 Analysis of 2D Configuration .....	59
7.3.2.1 Analysis of Current Density .....	59
7.3.2.2 Analysis of Concentration Fields .....	63
8. HP Indigo Case .....	72
8.1 Geometric Dimensions and Mixture Properties .....	72
8.2 Assumptions .....	82
8.3 QoM Simulations .....	85
8.4 BID Simulations .....	94
9. Summary and Conclusions .....	99
9.1 Conclusions .....	100
9.2 Future Work .....	102
Bibliography .....	103
Appendix A – Dimensional Analysis .....	I
Appendix B – Conservation Equations in Cartesian and Cylindrical Coordinates .....	V
Appendix C – Analytical Approach .....	VII

## List of Figures

Figure 1: Screening effect caused by the generation of EDL [7].....	2
Figure 2: ISOPAR L mixture composition [9]. .....	3
Figure 3: Indigo industrial LEP technology printer – main units [10].....	4
Figure 4: HP Indigo digital press printing cycle [11-12].....	4
Figure 5: BID unit section [13].....	6
Figure 6: Schematic of the gap between the ME and DR in which the ink flows [13]. .....	7
Figure 7: Schematic of space charge density of symmetric binary electrolyte subjected to different electrical voltages. [35].....	18
Figure 8: Schematic of different current regimes as a function of membrane-reservoir applied voltage. [42].....	19
Figure 9: Gouy-Chapman model for EDL. Electric potential decays exponentially when moving away from the charged surface.....	30
Figure 10: Schematic description of Couette-Poiseuille flow between two parallel plates. ....	34
Figure 11: Analytical velocity profile of a fully developed Couette-Poiseuille flow between two parallel plates, for different pressure gradient values. ....	35
Figure 12: Normalized particle concentration as a function of the duct radius for different $G$ values.....	39
Figure 13: $x$ velocity component of the fully developed Couette-Poiseuille flow between two parallel plates. Analytical and numerical results. ....	42
Figure 14: Tangential velocity component of a fully developed mixture-flow through a curved duct. Analytical and numerical results.....	43
Figure 15: Concentration profile of particle species obtained by numerical simulation in the fully developed region in the absence of an electric field. ....	44
Figure 16: Schematic of (a) permselective membrane-bulk configuration and (b) two electrodes configuration. ....	47
Figure 17: Non-dimensional steady state $I_y - V$ dependence. Comparison between the presently obtained and independent [35] results obtained for 1D and 2D configurations. The results are obtained for $N = 2$ , $\epsilon = 10^{-3}$ , and $V \in [0 \div 120]$ . For the 2D configuration the values of $AR = 6$ , $Sc = 10^3$ , and $Pe = 0.5$ were used. ....	49
Figure 18: Grid independence test by means of transient current density obtained by rheoTool 2D simulations of the membrane-bulk configuration. Results are obtained for $N = 2$ , $V = 25$ , $\epsilon = 10^{-3}$ , $AR = 6$ , $Sc = 10^3$ , and $Pe = 0.5$ . Insets: Close-up on the ECI onset represented by two consecutive abrupt peaks of the current density response including accurate values obtained by employing Richardson extrapolation based on G2 and G3 grids. ....	50
Figure 19: Comparison between 1D results provided by the specifically written Matlab script and 2D results provided by the rheoEfoam solver for the two electrodes configuration operating in the limiting regime: (a) concentration of the anion species, $c^-$ ; (b) concentration of the cation	

species,  $c^+$ ; (c) electric potential field,  $\Psi$ ; (d) magnitude of the electric field,  $|\vec{E}|$ . Results are obtained for the values  $V=40$ ,  $\epsilon \in [10^{-3} \div 10^{-2}]$ , and for the 2D case  $AR=6$ ,  $Sc=10^3$ , and  $Pe=0.45$  at  $t=0.01$ . Solid lines and circles correspond to the results provided by the Matlab script and the rheoEfoam solver, respectively. ....52

Figure 20: Distribution of absolute value of the space charge density,  $\rho_E$ , obtained for 1D ionic transport between the two open electrodes. The results are obtained for the values of  $\epsilon = 2.5 \times 10^{-4}$ ,  $t = 1.7 \times 10^{-6}$ , and for 3 species  $c_r = 10^{-4}$ . The results corresponding to the symmetric binary electrolyte and to the strongly non-symmetric electrolyte are denoted by the dashed and the solid lines, respectively. ....55

Figure 21: Spatial distribution of the terms  $|z_i|c_i$  ( $i = 1, 2, 3$ ) contributing to the space charge density  $\rho_E$ . The results are obtained for the values of  $\epsilon = 2.5 \times 10^{-4}$ ,  $c_r = 10^{-4}$ , and  $t = 1.7 \times 10^{-6}$ . ....56

Figure 22: Spatial distribution of the electric field magnitude,  $|\vec{E}|$ , for different  $c_r$  values. The results are obtained for the value of  $\epsilon = 2.5 \times 10^{-4}$  and  $t = 1.7 \times 10^{-6}$ . ....58

Figure 23: Time evolution of the current density obtained by the numerical simulations of ionic transport within 2 or 3 species electrolytes for 1D and 2D configurations. The results are obtained for the value of  $c_r = 2 \times 10^{-5}$  and for the values of: (a)  $\epsilon = 2.5 \times 10^{-4}$ ; (b)  $\epsilon = 5 \times 10^{-4}$ ; (c)  $\epsilon = 10^{-3}$ ; (d)  $\epsilon = 2 \times 10^{-3}$ . ....60

Figure 24: Time evolution of the current density obtained by the numerical simulations of ionic transport within a 3 species electrolyte for 2D configuration. The results are obtained for the value of  $\epsilon = 5 \times 10^{-4}$  and three different values of  $c_r$ . Close-up is of the ECI onset. ....63

Figure 25: ECI patterns of cation and anion species a short time after its generation, including 1D charge concentration curve of each species. (a)  $\epsilon = 2.5 \times 10^{-4}$ ,  $c_r = 2 \times 10^{-5}$ ; (b)  $\epsilon = 5 \times 10^{-4}$ ,  $c_r = 2 \times 10^{-5}$ ; (c)  $\epsilon = 10^{-3}$ ,  $c_r = 2 \times 10^{-5}$ ; (d)  $\epsilon = 2.5 \times 10^{-4}$ ,  $c_r = 10^{-4}$ ; (e)  $\epsilon = 5 \times 10^{-4}$ ,  $c_r = 10^{-4}$ ; (f)  $\epsilon = 10^{-3}$ ,  $c_r = 10^{-4}$ ; (g)  $\epsilon = 2.5 \times 10^{-4}$ ,  $c_r = 5 \times 10^{-4}$ ; (h)  $\epsilon = 5 \times 10^{-4}$ ,  $c_r = 5 \times 10^{-4}$ ; (i)  $\epsilon = 10^{-3}$ ,  $c_r = 5 \times 10^{-4}$ . ....65

Figure 26: Distribution of the absolute value of the non-dimensional space charge density,  $\rho_E$ , obtained for 1D ionic transport between the two open electrodes. The results are obtained for the values of  $\epsilon = 2.5 \times 10^{-4}$ ,  $t = 1.7 \times 10^{-6}$ , and three different values of  $c_r$ . ....71

Figure 27: Schematic of the gap dimensions. ....72

Figure 28: HP Mini QoM device. ....73

Figure 29: Schematic of mini QoM dimensions. ....73

Figure 30: Absolute current density through any height value  $\tilde{y}_0$  for 10 different times. ....86

Figure 31: Current density received due to applied voltage of 1500V for different initial micelles concentration. ....87

Figure 32: Current density received due to applied voltage of 500V for different initial micelles concentration. ....87

Figure 33: Fitted curves for initial current density (time $10^{-4}$ s) obtained by both simulated and experimental results as a function of the micelles bulk concentration.....	89
Figure 34: Values of the correction coefficient $\alpha$ as a function of the micelles bulk concentration. ....	89
Figure 35: Corrected current density prediction according to the utilized $\alpha$ model due to applied voltage of 1500V for different initial micelles concentration.....	90
Figure 36: Corrected current density prediction according to the utilized $\alpha$ model due to applied voltage of 500V for different initial micelles concentration.....	90
Figure 37: Geometry dimensions and mesh details of QoM simulations: (a) 2D; (b) 3D.....	92
Figure 38: Concentration fields of cation and anion species in the vicinity of the bottom and top QoM electrodes, respectively, a short time after the ECI onset. The convective cells containing VP are related to 2D rheoTool simulations.....	92
Figure 39: Concentration fields of cation and anion species on the bottom and top QoM electrodes, respectively, a short time after the ECI onset. The spatial concentration patterns are related to 3D rheoTool simulations.....	93
Figure 40: The effect of moving boundary on ECI.....	95
Figure 41: Current density as a function of time for stationary and moving top boundary configurations.....	96
Figure 42: Magnification of figure 41. Instability patterns superimposed with the corresponding time evolution of electric current density. ....	96
Figure 43: Isometric view and front, side, and top view of the concentration fields a short time after the ECI onset, $t=0.01$ s. Left: anion concentration. Right: ink concentration. ....	97
Figure 44: Isometric view and front, side, and top views of the concentration fields a short time after the ECI onset, $t=0.012$ s. Left: anion concentration. Right: ink concentration.....	98
Figure I: A Gaussian surface around a complete cylinder.....	XIII



## List of Tables

Table 1: Non-dimensional time and current density values of the minimum and maximum points of the first abrupt peak for different grids, compared to those obtained in Ref. [51].	51
Table 2: Non-dimensional parameters utilized in the numerical simulations.	54
Table 3: Non-dimensional initial concentration values utilized for different $c_r$ values characterizing the strongly non-symmetric electrolyte.	62
Table 4: Values of relative time difference $\tau$ (in percent) between the times characterizing the ECI onset at the cathode and anode.	66
Table 5: Non-dimensional wave numbers $k_1$ and $k_2$ in the vicinity of the cathode and anode, respectively.	68
Table 6: DR-ME gap and QoM geometric dimensions.	74
Table 7: Mixture and species properties.	75
Table 8: Wave numbers of vortex pairs addressing 2D and 3D rheoTool simulations of 2 or 3 species electrolytes. Results are related to a short time after the ECI onset while $\tilde{k}_x$ and $\tilde{k}_z$ are wave numbers in the $x$ and $z$ directions, respectively.	94

# Nomenclature

Description	Symbol	Units	Value
Cross-section/surface area	$A$	$m^2$	
Aspect ratio	$AR$	-	
Parameters	$A, B, G, a \div e, n$	Depends on the parameter	
Magnetic field intensity	$B$	T	
Gap width between electrodes	$a$	m	
Integration constants	$a_1, a_2, c_1, c_2$	Depends on the equation	
Functions of the variation of parameters approach	$C_1, C_2$	Depends on the function	
Species concentration	$c$	$mol/m^3$	
Initial bulk concentration of symmetric binary ions	$c_0$	$mol_i/m^3$	
Initial bulk concentration of charge director species (cations and anions together)	$c_{0\_cd}$	$mol_{cd}/m^3$	
Initial bulk concentration of effective micelles (cations and anions together)	$c_{0\_cd\_eff}$	$mol_{cd}/m^3$	
Initial bulk concentration of solid ink particles	$c_{0\_s}$	$mol_s/m^3$	
Concentration of: (1) cations; (2) anions; (3) third negatively charged species	$c_1, c_2, c_3$	$mol/m^3$	
Initial bulk concentration of cation species	$c_0^+$	$mol_+/m^3$	
Initial bulk concentration of anion species	$c_0^-$	$mol_-/m^3$	
Concentration of species i	$c_i$	$mol_i/m^3$	
Reference bulk ionic concentration of species i	$c_{i,0}$	$mol_i/m^3$	
Maximum constant concentration of solid particles	$c_{max}$	$mol_s/m^3$	
Concentration ratio	$c_r$	-	
Concentration of solid particles species	$c_s$	$mol_s/m^3$	
Ink species concentration	$c^{ink}$	$mol_{ink}/m^3$	
Initial bulk concentration of ink species	$c_0^{ink}$	$mol_{ink}/m^3$	
Cation species concentration	$c^+$	$mol_+/m^3$	
Anion species concentration	$c^-$	$mol_-/m^3$	
Percentage of effective micelles	$cd_{eff}$	%	
Molecular diffusion coefficient of: (1) cations; (2) anions; (3) third negatively charged species	$D_1, D_2, D_3$	$m^2/s$	
Molecular diffusion coefficient of charge director species	$D_{cd}$	$m^2/s$	
Hydraulic diameter	$D_H$	m	
Molecular diffusion coefficient of species i	$D_i$	$m^2/s$	
Molecular diffusivity ratio of species i	$D_{r_i}$	-	
Molecular diffusion coefficient of solid particles	$D_s$	$m^2/s$	
Molecular diffusion coefficient of cation species	$D^+$	$m^2/s$	
Average diameter of micelles	$d_{cd}$	m	

Description	Symbol	Units	Value
Particle diameter	$d_p$	m	
Average diameter of solid ink particles	$d_s$	m	
Electric field vector	$\vec{E}$	N/C = V/m	
Electric field components	$E_x, E_y, E_z, E_r, E_\theta$	N/C = V/m	
Relative density error	$Err_\rho$	-	
Electron's elementary charge	$e$	C	1.6e-19
Faraday's constant	$F$	C/mol	96,485
Body force components	$F_x, F_y, F_z, F_r, F_\theta$	N/m <sup>3</sup>	
Inhomogeneous term of a differential equation	$f$	Depends on the equation variable	
External body force per unit volume vector acting on the mixture	$\vec{f}$	N/m <sup>3</sup>	
Electric body force per unit volume vector acting on the mixture	$\vec{f}_E$	N/m <sup>3</sup>	
External body force per unit mass vector acting on phase i	$\vec{f}_i$	N/kg	
External body force per unit mass vector acting on a particle	$\vec{f}_p$	N/kg	
Hartmann number	$Ha$	-	
Grid step	$h, \Delta x$	m	
Enthalpy of phase i at non-equilibrium	$h_i^n$	J/kg	
Identity tensor	$[I]$	-	
Characteristic current density	$I_0$	C/m <sup>2</sup>	
Limiting current density	$I_{lim}$	C/m <sup>2</sup>	
Particle moment of inertia tensor	$[I_p]$	kg · m <sup>2</sup>	
Total surface-averaged current density	$I_y$	C/m <sup>2</sup>	
Ionic flux of species i	$\vec{J}_i$	mol <sub>i</sub> /m <sup>2</sup> · s	
Characteristic ionic flux	$J_0$	mol <sub>+</sub> /m <sup>2</sup> · s	
y component of ionic flux	$J_y$	mol/m <sup>2</sup> · s	
Ionic flux of ink species	$J_y^{ink}$	mol <sub>ink</sub> /m <sup>2</sup> · s	
Ionic flux of cation species	$J_y^+$	mol <sub>+</sub> /m <sup>2</sup> · s	
Ionic flux of anion species	$J_y^-$	mol <sub>-</sub> /m <sup>2</sup> · s	
Mixture thermal conductivity	$k$	W/m · K	
Boltzmann constant	$k_B$	J/K	1.381e-23
Wave number in the x and z directions	$k_x, k_z$	vortex pairs / mm	
Geometric characteristic length	$L, l_0, H$	m	
Euclidean norm	$L_2$	-	
Main electrode arc length	$l$	m	
Valence index of the i=3 species	$M$	-	
Molar mass of the charge director species	$M_{cd}$	kg/mol <sub>cd</sub>	
Molar mass of species i	$M_i$	kg/mol <sub>i</sub>	

Description	Symbol	Units	Value
External moment vector acting on a particle	$\vec{M}_p$	N · m	
Molar mass of the ink species	$M_s$	kg/mol <sub>s</sub>	
Mass	$m$	kg	
Mass of a single charge director particle	$m_{cd}$	kg	
Mass rate per unit volume of production of phase i	$\dot{m}'_i$	kg/m <sup>3</sup> · s	
Mass of species i	$m_i$	kg	
Mass of a single solid ink particle	$m_s$	kg	
Total mass	$m_T$	kg	
Maximum to minimum ratio of initial species concentration	$N$	-	
Avogadro number	$N_A$	particles / mol	6.02e23
Unit vector perpendicular to a surface	$\hat{n}$	-	
Mixture pressure	$P$	Pa	
Péclet number	$Pe$	-	
Characteristic pressure	$P_0$	Pa	
Pressure of phase i	$P_i$	Pa	
Volumetric force vector of interaction between phases acting on phase i	$\vec{p}_i$	N/m <sup>3</sup>	
Wetted perimeter	$p$	m	
Volumetric flow rate in the gap between the back electrode and the developer roller	$Q_{BE-DR}$	m <sup>3</sup> /s	
Net charge enclosed within a Gaussian surface	$Q_{in}$	C	
Volumetric flow rate in the gap between the main electrode and the developer roller	$Q_{ME-DR}$	m <sup>3</sup> /s	
Volumetric flow rate in the gap between the BID electrodes	$Q_{neck}$	m <sup>3</sup> /s	
Internal heat sources within the mixture	$\dot{q}$	W/m <sup>3</sup>	
Net heat flux out of phase i	$\vec{q}_i$	W/m <sup>2</sup>	
Reynolds number	$Re$	-	
Current density ratios	$R_I, R_{II}, R_{III}, R_{IV}$	-	
Radial coordinate	$r$	m	
Developer roller radius	$r_1$	m	
Main electrode radius	$r_2$	m	
Average radius of spherical particle species	$r_i$	m	
Radial unit vector	$\hat{r}$	-	
Schmidt number	$Sc$	-	
Stokes number	$Stk$	-	
Rate of concentration source of species i	$S_i$	mol <sub>i</sub> /m <sup>3</sup> · s	
Mixture temperature	$T$	K	
Stress tensor of phase i	$[T_i]$	N/m <sup>2</sup>	
Time	$t$	s	
Characteristic time	$t_0$	s	
Time step	$\Delta t$	s	
Mixture specific energy	$U$	J/kg	

Description	Symbol	Units	Value
Specific internal energy of phase i	$U_i$	J/kg	
Mixture velocity vector	$\vec{u}$	m/s	
Characteristic velocity magnitude	$u_0$	m/s	
Fluid velocity vector	$\vec{u}_f$	m/s	
Velocity vector of phase i	$\vec{u}_i$	m/s	
Internal energy per unit volume rate of production of phase i	$u_i'$	W/m <sup>3</sup>	
Electromigration velocity vector of species i	$\vec{u}_{M,i}$	m/s	
Particle velocity vector	$\vec{u}_p$	m/s	
Mixture average inlet velocity	$u_{av}$	m/s	
Boundary wall velocity	$u_{wall}, u_{\theta\_wall}$	m/s	
Velocity components	$u_x, u_y, u_z, u_r, u_\theta$	m/s	
Tangential component of the average mixture velocity entering the ME-DR gap	$\bar{u}_\theta$	m/s	
System volume	$V$	m <sup>3</sup>	
Voltage	$V$	V	
Volume of a single spherical charge director particle	$V_{cd}$	m <sup>3</sup>	
Volume of phase or species i	$V_i$	m <sup>3</sup>	
Volume of a single spherical ink particle	$V_s$	m <sup>3</sup>	
Total volume	$V_T$	m <sup>3</sup>	
Thermal voltage	$V_T$	V	
Electric potential difference	$\Delta V$	V	
Developer roller length	$w$	m	
x coordinate	$\bar{x}, x$	m	
Unit vector in the x direction	$\hat{x}$	-	
Mass fraction of charge director	$Y_{cd}$	-	
Mass fraction of species i	$Y_i$	-	
Mass fraction of liquid oil	$Y_l$	-	
Mass fraction of solid ink particles	$Y_s$	-	
y coordinate	$\bar{y}, y$	m	
Height from bottom reference surface	$y_0$	m	
Homogeneous solution of a differential equation with variable y	$y_h$	Depends on the equation variable	
Max value of y variable	$y_{max}$	Depends on y variable	
Private solution of a differential equation with variable y	$y_p$	Depends on the equation variable	
Wall velocity variable	$y_{wall}$	m/s	
z coordinate	$z$	m	
Valence of: (1) cations; (2) anions; (3) third negatively charged species	$z_1, z_2, z_3$	-	
Valence of charge director species	$z_{cd}$	-	
Valence of species i	$z_i$	-	

Description	Symbol	Units	Value
Valence ratio of species i	$z_{r_i}$	-	
Valence of solid particles species	$z_s$	-	
Valence of cation species	$z^+$	-	
Valence of anion species	$z^-$	-	
Correction coefficient	$\alpha$	-	
Volume fraction of phase or species i	$\alpha_i$	-	
Volume fraction of solid particles species	$\alpha_s$	-	
Mixture equivalent property	$\beta$	Depends on the property	
Property of species i	$\beta_i$	Depends on the property	
Electrostatic screening length	$\epsilon$	-	
Mixture absolute permittivity	$\epsilon$	$C^2 / N \cdot m^2$	
Vacuum permittivity	$\epsilon_0$	$C^2 / N \cdot m^2$	8.854e-12
Mixture relative permittivity	$\epsilon_r$	-	
Mixture dynamic viscosity	$\eta$	Pa · s	
Fluid dynamic viscosity	$\eta_l$	Pa · s	
Dynamic viscosity of ink species	$\eta_s$	Pa · s	
Tangential coordinate	$\theta$	rad	
Tangential unit vector	$\hat{\theta}$	-	
Electrohydrodynamic coupling constant	$\kappa$	-	
Charge density	$\lambda$	C/m	
Debye length	$\lambda_D$	m	
Electrical mobility of charge director species	$\mu_{cd}$	$m^2 / V \cdot s$	
Electrical mobility of species i	$\mu_i$	$m^2 / V \cdot s$	
Electrical mobility of solid ink species	$\mu_s$	$m^2 / V \cdot s$	
Mixture kinematic viscosity	$\nu$	$m^2 / s$	
Kinematic viscosity of liquid oil	$\nu_l$	$m^2 / s$	
Order of magnitude	$O$	-	
Mixture density	$\rho$	$kg / m^3$	
Density of charge director particles	$\rho_{cd}$	$kg / m^3$	
Space charge density	$\rho_E$	$C / m^3$	
Density of phase or species i	$\rho_i$	$kg / m^3$	
Oil density	$\rho_l$	$kg / m^3$	
Particle density	$\rho_p$	$kg / m^3$	
Density of solid ink particles (not porus)	$\rho_s$	$kg / m^3$	
Electrical conductivity per unit length	$\sigma$	S/m	
Electrostatic Maxwell stress tensor	$[\sigma]$	$N / m^2$	
Deviatoric shear stress tensor	$[\tau]$	$N / m^2$	
Stokes relaxation time	$\tau_p$	s	

Description	Symbol	Units	Value
Mixture viscous dissipation	$\Phi$	$\text{W}/\text{m}^3$	
Electric flux	$\Phi$	$\text{N} \cdot \text{m}^2/\text{C}$	
Externally imposed electric potential	$\phi_{Ext}$	V	
Solution form of differential equation	$\varphi$	Depends on the equation variable	
Electric potential	$\Psi$	V	
Electric potential supplied to the developer roller	$\Psi_{DR}$	V	
Electric potential supplied to the BID electrodes	$\Psi_{electrodes}$	V	
Intrinsic electric potential	$\psi$	V	
Reference intrinsic electric potential	$\psi_0$	V	
Dependent variable	$\Omega$	Depends on the variable	
Angular velocity of the developer roller	$\omega$	rad/s	
Particle angular velocity vector	$\vec{\omega}_p$	rad/s	

Subscripts:

Sign	Description	Sign	Description
0	Bulk / reference / vacuum	i	A specific phase or species
1, 2, 3	Indices	l	Liquid
I, II, III, IV	Indices	lim	Limiting
A	Avogadro	M	Migration
av	Average	ME	Main electrode
B	Boltzmann	max	Maximum
BE	Back electrode	n	Total number of phases or species
cd	Charge director	neck	Neck
D	Debye	p	Particle / Private
DR	Developer roller	r	Radial component / Ratio / Relative
E	Electric	s	Solid particles
Ext	External	T	Thermal / Total
eff	Effective	wall	Wall
electrodes	Electrodes	x	x component
f	Fluid	y	y component
G1, G2, G3	Different grids	z	z component
H	Hydraulic	$\theta$	Tangential component
h	Homogeneous	$\rho$	Density

Superscripts:

Sign	Description	Sign	Description
ink	Negatively charged ink species	+	Positively charge cation species
n	Non-equilibrium	-	Negatively charged anion species
T	Transpose	$\wedge$	Unit vector
y	y component	~	Dimensional quantities that have a non-dimensional representation
'	Rate of production		

Operators:

Sign	Description	Sign	Description
det	Determinant	[ ]	Tensor
W	Wronskian	$\vec{\nabla}$	Dell operator
$\otimes$	Tensor product	$\nabla^2, \Delta$	Laplacian



Abbreviations:

<b>Sign</b>	<b>Description</b>	<b>Sign</b>	<b>Description</b>
BC	Boundary Condition(s)	IC	Initial Condition(s)
BE	Back Electrode	ICEO	Induced Charge Electro-Osmosis
BGU	Ben-Gurion University	ITM	Intermediate Transfer Media
BID	Binary Ink Developer	LEP	Liquid Electrophotographic Printing
CFD	Computational Fluid Dynamics	LHS	Left Hand Side
CP	Concentration Polarization	ME	Main Electrode
DH	Debye-Hückel	MHD	MagnetoHydroDynamics
DL	Diffusion Layer	MPI	Message Passing Interface
DR	Developer Roller	NS	Navier-Stokes
EC	ElectroConvection	OLC	OverLimiting Current
ECI	ElectroConvective Instability	PB	Poisson-Boltzmann
EDF	Electrically-Driven Flow	PDE	Partial Differential Equation
EDL	Electric Double Layer	PIP	Photo Imaging Plate
EHD	ElectroHydroDynamics	PNP	Poisson-Nernst-Planck
EK	ElectroKinetic	PTE	Pre-Transfer Erase
EO	Electro-Osmosis	QoM	Q over M
EOI	Electro-Osmotic Instability	R.E.	Richardson Extrapolation
ESC	Extended Space Charge	RHS	Right Hand Side
FV	Finite Volume	UDF	User-Defined Function
GNF	Generalized Newtonian Fluids	VP	Vortex Pairs
GUI	Graphical User Interface		

# 1. Introduction

This report presents a theoretical study of multiphase flow, consisting of charged solid particles moving within an electrolyte fluid under the action of an electric field. The study is motivated by a number of problems faced while operating the HP Indigo printers, whose digital printing technology is based on liquid ink driven by electrical forces. This research was initially conducted by Michael Hagayev, in the framework of a final B.Sc. project under the supervision of Prof. Avi Levy from the Mechanical Engineering Department of BGU and HP Indigo's presenter Mr. Tal Eluk, a former student of Prof. Levy. Within the framework of the above-mentioned project, a physical model that includes governing equations was developed. The equations were solved by an analytical approach for the fully developed region under a number of basic assumptions. In addition, numerical simulations were performed by utilizing the Ansys Fluent program for single-phase flow in the absence of an electric field.

The objective of the current study is to develop a comprehensive numerical methodology that is capable of simulation of multiphase flow subjected to an electric field by means of standard techniques of computational fluid dynamics (CFD). The methodology is focused on the development of a physical model incorporating the electrohydrodynamics (EHD) phenomenon, including governing equations, definitions, and constitutive laws. The developed physical model provides the capability of comparing the analytically and numerically obtained results by means of the distributions of the charged particle concentrations and the mixture velocity fields. First, a simplified well-known physical model will be tested in order to verify the numerical results. Second, a two-way coupled physical model will be implemented in order to characterize the electro-osmotic flow of a strongly non-symmetric electrolyte. Lastly, the developed methodology will be utilized for the numerical simulation of multiphase flows with the purpose of addressing the fundamental multi-physics phenomena typical of those observed in HP Indigo's configurations.

It is expected that this study will comprise a basis for a fundamental understanding of the impact of different operating parameters on the printing quality of HP Indigo laser printers.

Modeling of Van Der Waals and capillary forces, Brownian motion, and particle charging mechanisms remained out of the scope of the current research, for the sake of simplicity.

## 2. Background

Multiphase flows are multiscale phenomena, ubiquitous in a variety of physical and industrial processes. These flows consist of two or more thermodynamic phases, which can be part of the same chemical component (e.g. water and vapor water) or several different chemical components (e.g. water flow combined with silicon particles). Multiphase flows may contain gas, liquid, or solid particle phases, or any combination in between. Several examples of natural multiphase flows are the transport of pure air (wind), sandstorms, volcanic eruptions, and blood flow within our veins. Several examples of industrial multiphase flows are sewage pipe flows, hydraulic or pneumatic transport of solid particles, cavitating pumps, and fluidized beds. The higher the number of phases of the flow, the more complicated is its physical modeling and numerical simulation. Moreover, many other physical phenomena, such as heat transfer, chemical reactions between phases, evaporation, melting, electromagnetic forces acting on a charged phase etcetera, may simultaneously take place within the flow.

EHD is the study of the hydrodynamics of electrically charged fluids [2-3]. The EHD discipline focuses on the interactions between external and induced electric fields and fluid motion in the presence of ionized particles [4]. EHD gathers several mechanisms of particle motion in a fluid: electrophoresis, electro-osmosis (EO), etc. Electrokinetic (EK) phenomena address the formation of equilibrium or quasi-equilibrium electric double layers (EDL) in the micro and nano scales [4-6]. EDL is a structure that is generated due to the interaction between charged substrate and fluid flow. The first layer of negative or positive charge ions is attached to the object surface due to chemical interactions or metal kept at a certain potential, while the second layer is made up of the oppositely signed ions attracted to the first layer via Coulomb forces. This second layer, named the Stern layer, electrically screens the first one, as can be seen in figure 1:

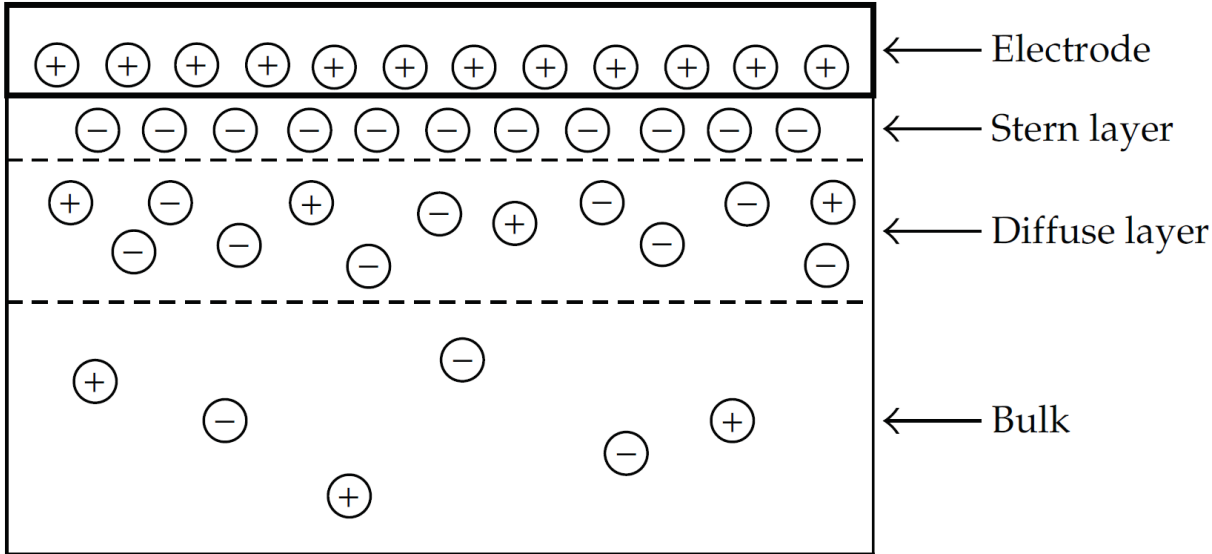


Figure 1: Screening effect caused by the generation of EDL [7].

Both EHD and EK phenomena are collectively called electrically-driven flows (EDFs) throughout this work. Several examples of EDF applications are fuel cells, separation techniques, electro dialysis, fluid pumping, and mixing in microfluidic systems [8].

This study deals with multiphase flow typical of liquid electrophotographic printing (LEP) printers designed and produced by the HP Indigo company. This flow contains charge carrying polymeric ink particles embedded within an electrolyte that consists of charge director micelles surrounded by an oil medium. This mixture is known as ISOPAR L and is characterized by the composition scheme shown in figure 2.

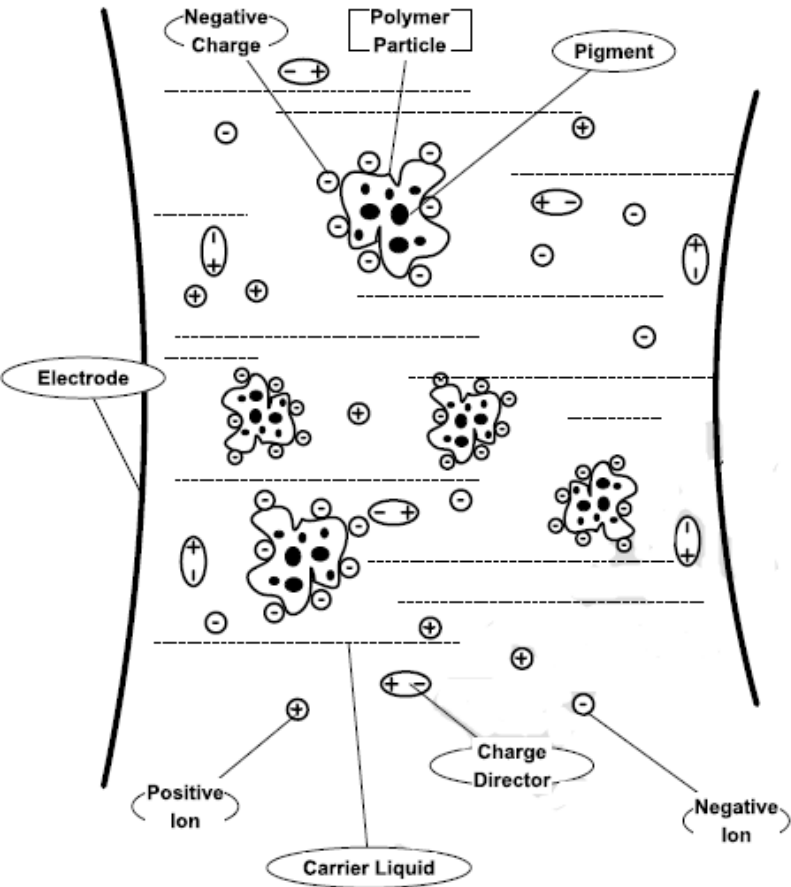


Figure 2: ISOPAR L mixture composition [9].

### 2.1 Main Units of LEP Printers

This section introduces Indigo’s LEP technology printer and describes its main units relevant to the current study. Figure 3 presents a typical model of the printer.



**Figure 3: Indigo industrial LEP technology printer – main units [10].**

The printer consists of diluting and charging units, a computer station, a digital cyclic printing unit, an oil leftover treatment unit, voltage and thermal controllers, and more. This work will focus on the central unit in which the digital periodic printing process takes place, as shown in figure 4.

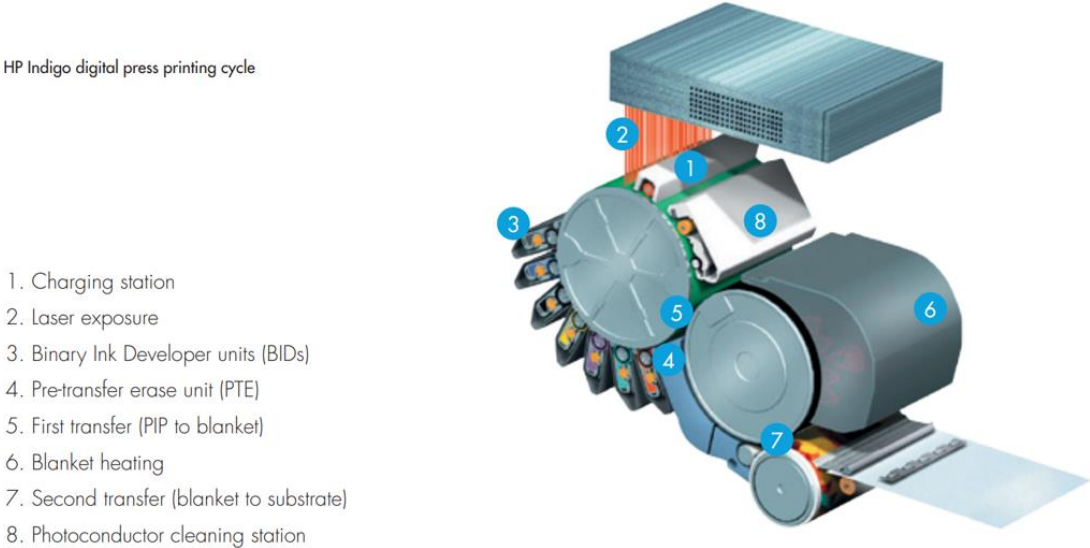


**Figure 4: HP Indigo digital press printing cycle [11-12].**

Description of the different components introduced in figure 4:

1. The charging station positively charges the photo imaging plate (PIP) roller surface (marked in green in figure 4).
2. Exposure to the laser beam electrically discharges specific sections on the PIP surface, forming a desirable photo image, as controlled by the computer unit connected to the printer.
3. Charged ink particles mixed with electrolyte oil are transferred from the binary ink developer (BID) units to the charged regions on the PIP surface.
4. The pre-transfer erase (PTE) unit removes the redundant ink and oil from the PIP surface cleaning it prior to further transportation of the digital photo image to the intermediate transfer media (ITM) roller (marked in black in figure 4).
5. The first transfer of the digital photo (also called "blanket") through the ITM roller takes place.
6. The "blanket" is heated up to melt the ink particles and to evaporate the oil.
7. The second transfer of the "blanket" with the melted ink particles on its surface takes place by pressing it on the printing paper to get the final image.
8. The remaining ink is cleaned and the PIP surface is further cooled.

The above process occurs every entire circle of the PIP drum, each time with a different BID color. Applying this technology to form a number of different color layers, the final photo is printed on the paper.

Figure 5 shows a section view of the BID unit.

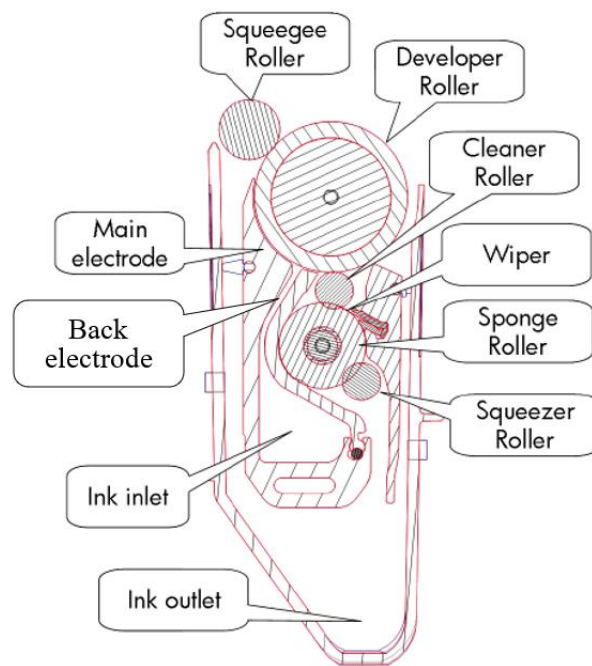


**Figure 5: BID unit section [13].**

Description of the BID components:

Ink inlet – diluted ink mixture enters the BID domain.

Main electrode (ME) – stationary main electrode.

Back electrode (BE) – back stationary electrode at the same electric potential as the ME.

Developer roller (DR) – an important drum at the BID which is kept at an electric potential different from that of the electrodes. The DR rotates clockwise while the ink mixture flows in the gap between its surface and the ME.

Squeegee roller – another drum that rotates counterclockwise. Its purpose is to flatten the coming ink layer, increase its uniformity and attach it to the DR. After passing the squeegee roller, the mixture is transferred from the DR to the PIP shown in figure 4.

Cleaner roller – a counterclockwise roller that cleans remaining ink and oil from the DR and prepares it for the next round.

Wiper – removes remaining ink and oil from the cleaner roller.

Sponge roller – removes viscous ink leftovers from the cleaner roller and the wiper.

Squeezer roller – squeezes the sponge roller.

Ink outlet – remaining ink mixture leaves the BID for further processing and reuse.

The present research focuses on an analysis of the ink flow within the gap between the ME and the main roller of the BID (i.e. the DR). An enlarged sketch of this area is shown in figure 6, while a dimensional drawing and fluid properties of the ink mixture are given in chapter 8.

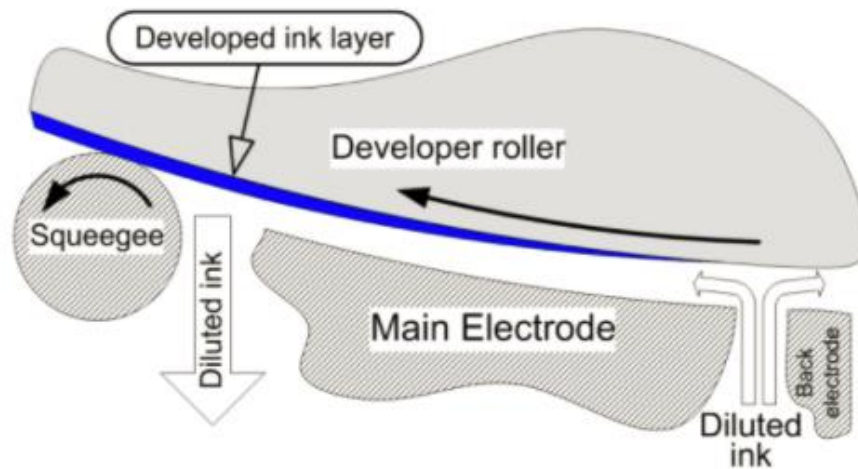


**Figure 6: Schematic of the gap between the ME and DR in which the ink flows [13].**

As can be seen from figure 6, diluted ink enters the neck between both electrodes, and splits to the right (between the BE and the DR) and the left (between the ME and the DR). It should be noted that most of the ink (about 67%) goes to the left. There is an electric potential difference between the electrodes and the DR so that an electric field is generated, which results in electric forces acting on the charged ink particles. The direction of the electric field vector is radially outwards from the DR. Because of the negative charge bonded to the ink particles, the electric force pulls the ink particles toward the DR surface. One should notice that due to the narrow gap between the ME and the DR (350  $\mu\text{m}$ ), the electric field vector and the fluid velocity vector are nearly perpendicular to each other – the electric field is radial while the flow velocity is tangential.



### 3. Literature Review

The present study focuses on analysis of multiphase flow. Several numerical methodologies have been developed over the years to model and analyze multiphase flows. Additionally, the present study includes analysis of an electrolytic fluid that contains ions and charged particles, whose dynamics are determined by the applied electric force. For this reason, some adjustments have to be made to the classical two/multi-phase models in terms of adding additional equations to provide two-way coupling between the electric and the hydrodynamic phenomena. In particular, the whole theoretical framework has been embedded by EDF models. This chapter introduces several multiphase methods and EDF models, in addition to an electro-osmotic flow characterization of a strongly non-symmetric electrolyte. An extensive discussion regarding the pros and cons of each method and model is presented, motivating the choice of a specific methodology that is suitable for the objectives of the present project. A detailed mathematical formulation of the chosen physical methodology, coupling the two-phase flow with the EDF model, is given in chapter 5.

#### 3.1 Methods for Solving the Multiphase Flows

The methods for numerical modeling of multiphase flows can be classified into three general families. This section elaborates each family of the methods, their usage, and the governing equations to be solved.

##### 3.1.1 Eulerian-Eulerian Method

This method addresses all  $n$  phases as a continuum. Solid particle phases are characterized by their concentration  $c$ , in terms of mass or number of particles per unit volume. A specific position in space cannot be occupied by several phases at the same time, that is, the volume occupied by each phase  $i$  cannot be occupied by the remaining phases at the same position in space at the same time. For that reason, the volume fraction  $\alpha_i$  of phase  $i$  is defined by the volume of phase  $i$ ,  $V_i$  in a system of volume  $V$  [14]:

$$V_i = \iiint_{V(t)} \alpha_i dV \quad \text{where} \quad \sum_{i=1}^n \alpha_i = 1. \quad (1)$$

In the Eulerian-Eulerian method, conservation equations are solved for each phase separately, as detailed below.

Mass conservation equation [14]:

$$\frac{\partial(\alpha_i \rho_i)}{\partial t} + \vec{\nabla} \cdot (\alpha_i \rho_i \vec{u}_i) = \dot{m}_i, \quad (2)$$

where  $\rho_i$ ,  $\vec{u}_i$  and  $\dot{m}_i$  are the density, velocity vector, and mass rate per unit volume of production of phase  $i$ , respectively,  $t$  is time, and  $\vec{\nabla}$  is the divergence operator.

Momentum conservation equation [14]:

$$\frac{\partial(\rho_i \alpha_i \vec{u}_i)}{\partial t} + \vec{\nabla} \cdot (\rho_i \alpha_i \vec{u}_i \otimes \vec{u}_i) = \vec{\nabla} \cdot [T_i] + \rho_i \alpha_i \vec{f}_i + \vec{p}_i + \dot{m}_i \vec{u}_i, \quad (3)$$

where  $\otimes$  is the tensor product that denotes a dyadic multiplication of (3x1) by (1x3) velocity vectors,  $[T_i]$  represents the stress tensor of phase  $i$ ,  $\vec{f}_i$  is a vector of external body force per unit mass acting on phase  $i$ , and  $\vec{p}_i$  represents the volumetric force originating from interactions between the different phases (e.g. drag force).

Energy conservation equation [14]:

$$\frac{\partial(\alpha_i \rho_i U_i)}{\partial t} + \vec{\nabla} \cdot (\alpha_i \rho_i \vec{u}_i U_i) = -\vec{\nabla} \cdot (\alpha_i \vec{q}_i) - P_i \frac{\partial \alpha_i}{\partial t} - P_i \vec{\nabla} \cdot (\alpha_i \vec{u}_i) + h_i^n \dot{m}_i + \dot{u}_i, \quad (4)$$

where  $U_i$  corresponds to the specific internal energy of phase  $i$ ,  $\vec{q}_i$  is net heat flux out of phase  $i$ ,  $P_i$  represents the pressure of phase  $i$ ,  $h_i^n$  is the non-equilibrium enthalpy of phase  $i$ , and  $\dot{u}_i$  indicates the rate of production of internal energy per unit volume of phase  $i$ .

### 3.1.2 Eulerian-Lagrangian Method

This method treats fluidic phases as continuous phases so that the conservation equations (2-4) are solved. However, solid particles are considered as a disperse phase. Particle trajectory calculations are based on the equation of motion of every single particle. The vector equation of motion for each particle, neglecting the Brownian motion, is given by [15]:

$$\frac{d\vec{u}_p}{dt} = -\frac{\vec{u}_p - \vec{u}_f}{\tau_p} + \vec{f}_p, \quad (5)$$

where  $\vec{u}_p$  and  $\vec{u}_f$  are particle and fluid velocity vectors, respectively,  $\vec{f}_p$  relates to the vector of external body force per unit mass acting on the particle (e.g. gravitation), and  $\tau_p$  refers to the Stokes relaxation time, which for spherical particles is calculated by [16]:

$$\tau_p = \frac{\rho_p d_p^2}{18\eta_l}, \quad (6)$$

where  $\rho_p$  and  $d_p$  are particle density and diameter, respectively, and  $\eta_l$  is the fluid dynamic viscosity. The Stokes relaxation time accounts for the particle inertia and is the time constant for the exponential decaying in particle velocity due to drag. In other words, Stokes relaxation time is proportional to the time that the particle takes to reach its velocity, which for small particles is approximately the fluid velocity.

In addition, the rotational dynamics of each particle is governed by the vector equation of motion due to the action of external moments:

$$[I_p] \frac{d\vec{\omega}_p}{dt} = \sum \vec{M}_p, \quad (7)$$

where  $[I_p]$  is the particle moment of inertia tensor,  $\vec{\omega}_p$  is the particle angular velocity vector, and the  $\vec{M}_p$  vector refers to the action of external moments on the particle.

With this formalism, six scalar equations corresponding to six degrees of freedom govern the spatial trajectory of each particle.

### 3.1.3 Mixture Method

Similar to the Eulerian-Eulerian method, all phases are assumed to be continuous. This method relates to all the  $n$  phases as one mixture consisting of  $n$  species, having equivalent properties (e.g. temperature, density, viscosity). These equivalent properties are calculated based on the volume fraction of each species  $\alpha_i$ , which generally can be time and space dependent:

$$\beta = \sum_i \alpha_i \beta_i, \quad (8)$$

where  $\beta$  is the mixture equivalent property (scalar or vector) and  $\beta_i$  is the property of the  $i^{th}$  species.

The four conservation equations to be solved for the mixture are as follows.

The mass conservation equation:

$$\frac{\partial \rho}{\partial t} + \vec{\nabla} \cdot (\rho \vec{u}) = 0, \quad (9)$$

where  $\rho$  and  $\vec{u}$  are the density and velocity vector of the mixture, respectively.

The momentum conservation equation:

$$\frac{\partial(\rho\vec{u})}{\partial t} + \vec{\nabla} \cdot (\rho\vec{u} \otimes \vec{u}) = -\vec{\nabla}P + \vec{\nabla} \cdot [\tau] + \vec{f}, \quad (10)$$

where  $P$  represents the pressure of the mixture,  $\vec{f}$  is the vector of the external body force per unit volume acting on the mixture, and  $[\tau]$  is the deviatoric shear stress tensor defined as:

$$[\tau] = \eta(\vec{\nabla}\vec{u} + \vec{\nabla}\vec{u}^T), \quad (11)$$

where  $\eta$  is the dynamic viscosity of the mixture.

The thermal energy conservation equation:

$$\frac{\partial}{\partial t}(\rho U) + \vec{\nabla} \cdot (\vec{u}(\rho U + P)) = \vec{\nabla} \cdot (k\vec{\nabla}T) + \Phi + \dot{q}, \quad (12)$$

where  $U$ ,  $k$ , and  $T$  are the specific energy, thermal conductivity, and temperature of the mixture, respectively,  $\Phi$  accounts for the viscous dissipation and  $\dot{q}$  represents internal heat sources within the mixture.

The concentration of each species is calculated by Fick's law of diffusion, which refers to the conservation of species  $i$  as:

$$\frac{\partial c_i}{\partial t} + \vec{\nabla} \cdot (c_i\vec{u}) = \vec{\nabla} \cdot (D_i\vec{\nabla}c_i) + S_i, \quad (13)$$

where  $c_i$  and  $D_i$  are the concentration and the molecular diffusivity of species  $i$ , respectively, and  $S_i$  refers to the rate of the concentration source of species  $i$ . The concentration variable may be based on the number or mass of particles per unit volume. Throughout this work, the units used for concentration are  $[\text{mol}_i/\text{m}^3]$ . The equations relating concentration, mass fraction and volume fraction of species  $i$  are:

$$\begin{aligned} c_i &= \frac{\alpha_i \rho_i}{M_i} = \frac{(V_i/V_T) \cdot (m_i/V_i)}{(m_i/\text{mol}_i)} = \frac{\text{mol}_i}{V_T} \\ c_i &= \frac{Y_i \rho}{M_i} = \frac{(m_i/m_T) \cdot (m_T/V_T)}{(m_i/\text{mol}_i)} = \frac{\text{mol}_i}{V_T}, \end{aligned} \quad (14)$$

where  $M_i$  is the molar mass of species  $i$ ,  $Y_i$  is the mass fraction of species  $i$ ,  $m$  and  $V$  denote mass and volume, respectively, and the subscript  $T$  means "Total". Similar to the volume fraction, the mass fraction fulfills:

$$\sum_{i=1}^n Y_i = 1. \quad (15)$$

Since the sum of volume or mass fractions has to be equal to unity (see equations (1) and (15)) equation (13) should be solved for only  $n - 1$  species [17]. The volume or mass fraction of the  $n^{\text{th}}$  species is determined as unity minus the sum of  $n - 1$  solved volume or mass fractions and the concentration of the  $n^{\text{th}}$  species is calculated according to equation (14). To further minimize numerical errors, the  $n^{\text{th}}$  species should be selected as the species with the largest overall volume or mass fraction.

### **3.1.4 Multiphase Flows Solving Methods: Pros and Cons**

Multiphase flow phenomena have been extensively investigated over the last six decades. During this period, a large number of different numerical methods have been developed to simulate various multiphase flows relevant to basic science and engineering applications. Each method is typically tailored to address the specific kind of flows. The Eulerian-Lagrangian method is used to calculate the trajectories of bubbles [18-19], particles [20-21] or droplets [22]. The Eulerian-Eulerian method facilitates accounting for the forces acting between different continuous phases when simulating bubble flows [23] and fluidized beds [24]. Several works compare between the above methods [15,25]. Another method widely used in various engineering applications is the mixture method, which is a simplification of the Eulerian-Eulerian method. Simulation of fluid-solid suspensions [26] and jet spray flames [27] for example, are the representative studies in which the mixture method has been implemented.

When carefully implemented, the Eulerian-Lagrangian method is the most accurate approach, requiring the minimal amount of basic assumptions. However, this method is the most computationally expensive because of the large number of equations – six per particle/bubble. Because of this, the Eulerian-Lagrangian method is limited to several tens of thousands of particles at the most. Besides, each simulation may take weeks, or even months, to run.

The Eulerian-Eulerian method treats particle phases as continuous, relying on constitutive laws and correlations used to approximate the properties of each phase and the interaction between the phases. The accuracy and reliability of the results obtained by the above approach may suffer if the correlations used do not exactly fit the flow under the consideration. At the same time, this method gives satisfactory results for a lot of practical applications, with much less computational effort than the Eulerian-Lagrangian approach.

The mixture method is the simplest way to approximate multiphase flows, because of the relatively small number of equations involved in the model. Conservation equations are solved for the whole mixture, while the mixture equivalent properties are obtained by an average-weighting. Due to these reasons, the mixture method is based on the largest number of physical assumptions and is not necessarily suitable for simulations of general multiphase flows. Still, this method is useful for simulating flows related to various engineering applications, providing results of acceptable quality, while making a reasonable computational effort.

Precise calculation of particle trajectories is out of the scope of the present study. As a result, any numerical method based on the Eulerian-Lagrangian approach should not be considered. In contrast, Eulerian-Eulerian and mixture methods are both suitable for this research. This report will focus on the mixture method because of its simplicity and reasonable computational effort. Furthermore, in this work the particles are considered to be small and light, so the drag force between them and the surrounding fluid is relatively small and can be safely neglected.

## 3.2 Electrically-Driven Flow (EDF) Models

Considering that the focus in this work is on a weak electrolyte subjected to an electric field, the external force term  $\vec{f}_i$ ,  $\vec{f}_p$ , or  $\vec{f}$  for either the Eulerian-Eulerian, the Eulerian-Lagrangian, or the mixture method, respectively, should be introduced to account for the electric force. In this case, additional relations must be provided in order to achieve a closed form of the overall system of equations. These relations depend on a specific EDF model. This section elaborates three different EDF models that can be embedded into the mixture method, including the governing equations and the limitations of each EDF model.

### 3.2.1 Poisson-Nernst-Planck (PNP) Model

In the absence of magnetic effects, the electric potential  $\Psi$  can be computed by the Gauss law [28]:

$$\vec{\nabla} \cdot (\varepsilon \vec{\nabla} \Psi) = -\rho_E, \quad (16)$$

where  $\varepsilon$  is the absolute permittivity of the electrolyte medium and  $\rho_E$  relates to the space charge density of the medium. Absolute permittivity is calculated by the following relation:

$$\varepsilon = \varepsilon_r \varepsilon_0, \quad (17)$$

where  $\varepsilon_r$  is the non-dimensional relative permittivity of the medium and  $\varepsilon_0$  is the constant vacuum permittivity.

The space charge density is defined as [28]:

$$\rho_E \triangleq F \sum_{i=1}^n z_i c_i, \quad (18)$$

where  $z_i$  is the valence of the  $i^{\text{th}}$  species,  $n$  is the number of charged species in the electrolyte and  $F$  denotes the Faraday's constant that is defined as:

$$F = eN_A, \quad (19)$$

where  $e$  is the electron's elementary charge and  $N_A$  is the Avogadro number.

The valence of a chemical element is related to the number of electrons in its outer shell. The valence of a chemical element is the combined power of the element with the surrounding electrons with which it will bond or form chemical compounds or molecules.

The Nernst-Planck equation (20) extends Fick's law of diffusion determined in equation (13). It is the standard law governing the transport of charged species in a weak electrolyte under the action of an electric field. The Nernst-Planck equation reads:

$$\frac{\partial c_i}{\partial t} = -\vec{\nabla} \cdot \vec{J}_i, \quad (20)$$

where  $\vec{J}_i$  is the ionic flux of the  $i^{\text{th}}$  species due to advection, diffusion and electric phenomena (in the absence of magnetic potential):

$$\vec{J}_i = c_i \vec{u} - D_i \vec{\nabla} c_i - \left( D_i \frac{z_i e}{k_B T} \vec{\nabla} \Psi \right) c_i, \quad (21)$$

where  $k_B$  is the Boltzmann constant.

### 3.2.2 Poisson-Boltzmann (PB) Model

In certain numerical simulations, there may be some difficulties when defining the boundary conditions for solving Gauss's law, determined in equation (16). A common approach to avoid this EDF simulation problem is the decomposition of the electric potential into two variables [28]:

$$\Psi = \phi_{Ext} + \psi, \quad (22)$$

where  $\phi_{Ext}$  refers to externally imposed electric potential and  $\psi$  is the intrinsic electric potential. Following this approach, Gauss's law determined in equation (16) is also decomposed into two equations [28]:

$$\begin{aligned} \vec{\nabla} \cdot (\varepsilon \vec{\nabla} \phi_{Ext}) &= 0 \\ \vec{\nabla} \cdot (\varepsilon \vec{\nabla} \psi) &= -\rho_E. \end{aligned} \quad (23)$$

An additional simplification is to consider the external electric force  $\vec{f}$  acting on the mixture formulated in equation (10) as only influenced by the externally imposed electric potential.

In such conditions, the PNP model can be simplified to the PB model. Assuming that the ions follow a Boltzmann equilibrium, Gauss's law for the intrinsic electric potential determined in equation (23) reads [28]:

$$\vec{\nabla} \cdot (\varepsilon \vec{\nabla} \psi) = -F \sum_{i=1}^n z_i c_{i,0} \exp\left(-\frac{e z_i}{k_B T} (\psi - \psi_0)\right), \quad (24)$$



where  $c_{i,0}$  is a reference bulk ionic concentration of species  $i$  and  $\psi_0$  is a reference intrinsic electric potential, typically valued as 0. Like in the PNP model, The Nernst-Planck equation (20) is solved.

### 3.2.3 Debye-Hückel (DH) Model

The DH model is a further simplification of the PB model for low intrinsic electric potentials

$\frac{ez_i}{k_B T} \psi \ll 1$ . By Taylor series expansion up to the second exponential term, equation (24)

becomes:

$$\vec{\nabla} \cdot (\epsilon \vec{\nabla} \psi) = -F \sum_{i=1}^n z_i c_{i,0} \left( 1 - \frac{ez_i}{k_B T} \psi \right). \quad (25)$$

As in the PB model, Gauss's law for the externally imposed electric potential (23), as well as the Nernst-Planck (20) equations, are solved.

### 3.2.4 EDF Models: Pros and Cons

Considering the mixture method, PNP is the most comprehensive EDF model in which the electric and hydrodynamic variables are two-way coupled. The efficiency and convergence rate of the model were extensively surveyed in [29]. An example of the PNP model usage is the modeling of EK transport and biogeochemical reactions in porous media [30]. PB and DH models are based on the electric potential splitting into external and intrinsic electric potentials. Considering the Gauss law, the intrinsic electric potential depends on the space charge density, which is influenced by the concentration of the charged mixture species. Considering Boltzmann equilibrium, the space charge density does not depend on species concentration variables (it only depends on the initial bulk concentrations). Hence, the electric variables depend neither on the species concentrations nor on the hydrodynamics (one-way coupling). Several studies applying the PB model have been performed, such as the dynamic ion adsorption process in porous electrodes of capacitive deionization [31] and the analysis and application of an ion size-modified PB equation [32]. The DH model suggests a simplified space charge density expression, rather than the PB's exponential relation. The expression is obtained by performing the Taylor series expansion and assuming a low value of the intrinsic electric potential. The new space charge density expression is numerically simpler to implement. The DH model has been successfully applied for the analysis of deformation and stability of a viscous electrolyte [33].

Among the above three EDF models, the PNP model provides the best description of the realistic physical state. However, its numerical implementation is complicated. PB and DH models are simpler but are not suitable for a wide range of electrical problems.

The EDF model chosen in this work is the PNP model. It has already been implemented and performs good simulation results in several open-source programs (see chapters 6-7). Besides, PB and DH models are not accurate enough when a high electric potential gradient is applied [28,34].

### 3.3 Physical Phenomena Relating to Bounding Electrolyte Subjected to Electric Potential Difference

Figure 7, taken from Ref. [35], demonstrates the electric charge density (electric charge per unit volume) field of a symmetric binary electrolyte consisting of positively charged cations and negatively charged anions of the same diffusivity and absolute valence values, subjected to various values of external voltage. The electrolyte presented is bounded by a stationary reservoir from the top and by an ion-selective surface that is permeable for cations only from the bottom. In this case, an electric field directed downwards is generated due to the externally supplied voltage. For low voltage values (figure 7(a)), an EDL is generated in the vicinity of the ionic selective surface, as mentioned in chapter 2. The thickness of this EDL is of  $O(\epsilon)$  [35], where  $\epsilon$  is the electrostatic screening length introduced in section 5.1.3. An electrically neutral diffusion layer (DL) is located out from the EDL towards the top reservoir [35]. The existence of a tangential electric field, perpendicular to the externally supplied voltage, may result in an electroconvection (EC) mechanism of the space charge density within the EDL, which is associated with the classical EO flow of the first kind related to the quasi-equilibrium EDL [36-41]. The presence of only EDL and DL for low voltages is associated with the Ohmic regime of the I-V curve presented as the underlimiting current in figure 8, taken from Ref. [42]. For supplied voltages close to the value of the thermal voltage defined in section 5.1.1, concentration gradients directed from the DL towards the ion-selective surface are developed. This phenomenon is known as concentration polarization (CP) [39-40,42,44-49]. At steady state, molecular diffusion ionic flux driven by this concentration gradient is equal (for an ideal ion-selective surface) to the oppositely directed electromigration flux of co-ions (see chapter 5) [35,48-51]. For higher voltage values (figure 7(b)), the CP limits the species transport and corresponds to diffusion limitation. This constraint results in a depletion region [35,42,52-55] associated with the extended space charge (ESC) region presented in figure 7 and the saturated current  $I_{lim}$  of the limiting regime presented in figure 8 [35,42,48-49,56-57]. The existence of a tangential electric field component within the ESC, along with the electric field component perpendicular to the ion-selective surface, may result in EO of the second kind (non-linear) related to non-equilibrium EDL [36,39-

41,44,49,53,58-60]. As can be seen from figure 8, high voltages are associated with the entrance to the overlimiting regime of the electric current. Rubinstein and Zaltzman were the first to associate the EC as a hydrodynamic mechanism that governs this overlimiting current (OLC) [39,41,44,59]. They examined extensively the generation of convective cells consisting of vortex pairs (VP) in the vicinity of the ion-selective surface, where the ionic concentration gradient is very significant. At voltages associated with the onset of the OLC regime, an electric field fluctuation in the tangential direction drives the EO of the second kind mechanism, which, in turn, generates a test vortex. This test vortex results in an additional concentration gradient, a local change in the electric resistance, and a local potential difference which enhances the tangential electric field. The enhanced electric field implies tangential electric force on the fluid and contributes to the intensity of the test vortex in the manner of a positive feedback mechanism [35,42,55]. For low voltages of the OLC regime, steady VP are generated (see figure 7(c)) [35,44-45,61]. This vortex phenomenon is called electroconvective instability (ECI) [48-50,62-63], or electro-osmotic instability (EOI) [35,54,62]. The ECI is possible due to EO of the second kind for a perfectly permselective surface or due to either equilibrium EO (first kind), bulk EC or both for non-ideal permselectivity of the surface [39-41,44,48-49,51,60,64-66]. For a highly ion-selective surface, the shape of the ESC layer has a great impact on the ECI characteristic [49-50]. Higher voltages (figure 7(d)) result in chaotic ECI, which is characterized by multi-layer vortex structures that mix the electrolyte, enhance ionic transport by convection, eject patches of positive and negative space charge density into the DL and increase the current value [35,42,44,50,56,60-62]. The OLC related to high voltage values is mostly associated with excess noise [8,35,39,44-45,60,62,67-71].

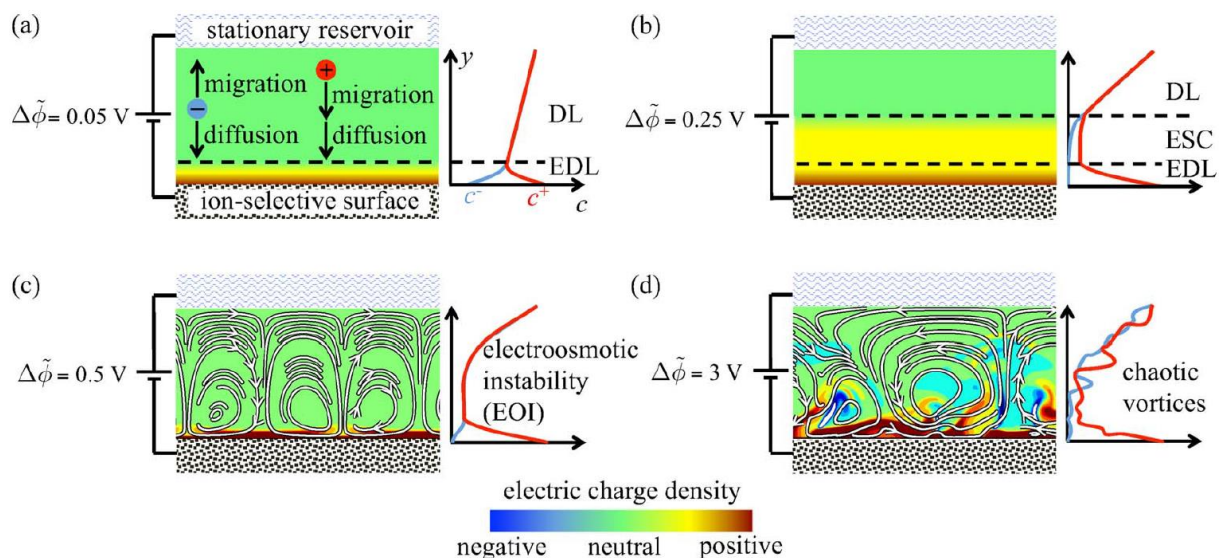


**Figure 7: Schematic of space charge density of symmetric binary electrolyte subjected to different electrical voltages. [35]**

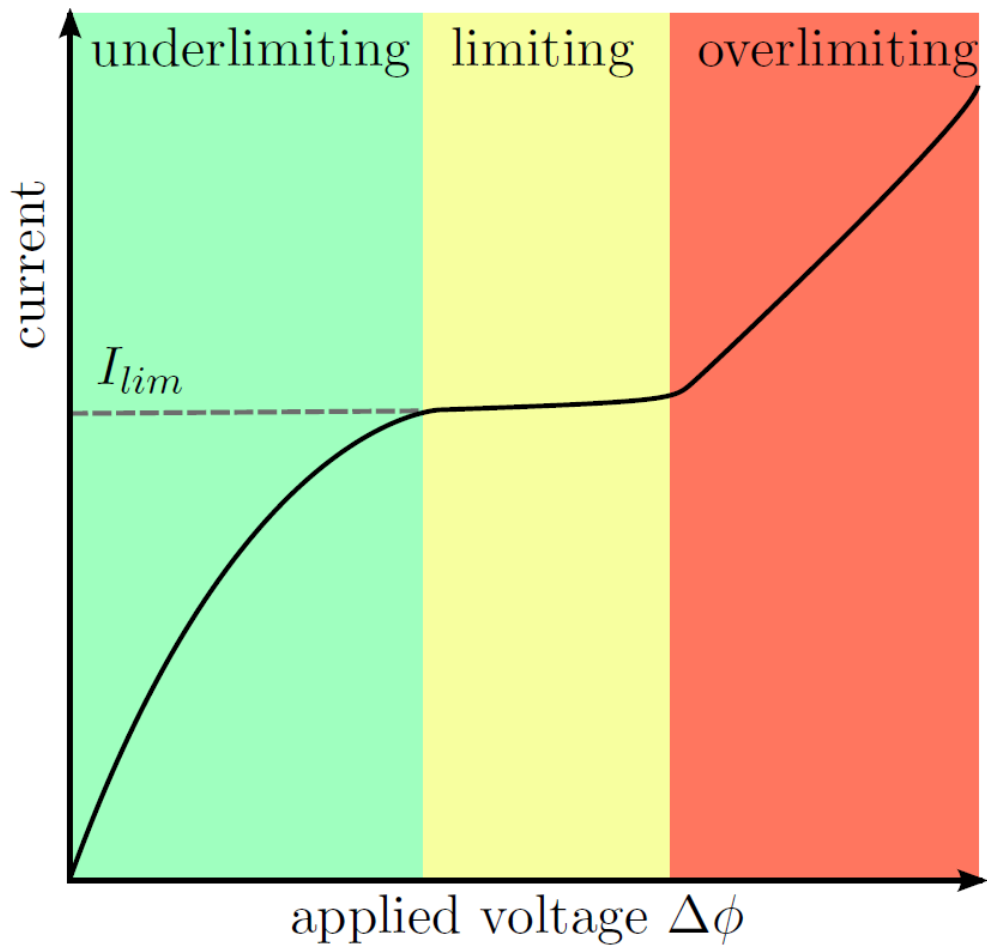


Figure 8: Schematic of different current regimes as a function of membrane-reservoir applied voltage. [42]

## **4. Research Objectives**

The objective of this research is to develop a comprehensive numerical methodology that is capable of addressing the above-described multi-physics phenomena, theoretically employing standard techniques of computational fluid dynamics. Implementation of this methodology should shed light on the physical processes simultaneously taking place in the EDF and help to investigate the triggers leading to the onset of EHD instability of the EDF under consideration.

The results of the present research should provide HP Indigo engineers with a verified and fully accessible CFD model, which will serve them as a tool for an in-depth understanding of the fundamental mechanisms of EDF taking place in different parts of the printer. It is believed that understanding the fundamental EDF mechanisms will shed light on ways to further improve the quality of printing.

An additional secondary objective is to investigate and characterize the electro-osmotic flow of a strongly non-symmetric electrolyte consisting of positively charged cation species, negatively charged anion species, and a third negatively charged species of high valence value, subjected to high voltage of the overlimiting regime.

## 5. The Physical Model

This chapter summarizes the governing equations, solved for an incompressible isothermal mixture flow, utilizing the PNP model. The governing equations are first formulated in dimensional form and then normalized by utilizing characteristic scales of the problem under consideration (see section 5.1). The tilde superscript  $\sim$  above a symbol denotes any dimensional physical quantity that has a non-dimensional representation. First, equivalent mixture density, dynamic viscosity, absolute permittivity, and temperature are calculated by utilizing equation (8). For incompressible flow characterized by a constant value of mixture density the continuity equation (9) is reduced to:

$$\vec{\nabla} \cdot \tilde{\mathbf{u}} = 0. \quad (26)$$

Additionally, when the mixture experiences an electric force, the momentum equation (10) is modified into:

$$\rho \left( \frac{\partial \tilde{\mathbf{u}}}{\partial \tilde{t}} + \tilde{\mathbf{u}} \cdot \vec{\nabla} \tilde{\mathbf{u}} \right) = -\vec{\nabla} \tilde{P} + \eta \nabla^2 \tilde{\mathbf{u}} + \tilde{\mathbf{f}}_E, \quad (27)$$

where  $\tilde{\mathbf{f}}_E$  vector is the electric body force acting on the mixture.

To find this force value, one should be familiar with the electrostatic Maxwell stress tensor [8]:

$$[\tilde{\sigma}] = \varepsilon \left[ \tilde{\mathbf{E}} \otimes \tilde{\mathbf{E}} - \frac{1}{2} (\tilde{\mathbf{E}} \cdot \tilde{\mathbf{E}}) [I] \right], \quad (28)$$

where  $[\tilde{\sigma}]$  is the electrostatic Maxwell stress tensor,  $\tilde{\mathbf{E}}$  indicates the electric field vector, and  $[I]$  denotes the appropriate identity tensor. The electric body force vector acting on the mixture is obtained by the divergence of the Maxwell stress tensor:

$$\tilde{\mathbf{f}}_E = \vec{\nabla} \cdot [\tilde{\sigma}] = \vec{\nabla} \cdot \left[ \varepsilon \left( \tilde{\mathbf{E}} \otimes \tilde{\mathbf{E}} - \frac{1}{2} (\tilde{\mathbf{E}} \cdot \tilde{\mathbf{E}}) [I] \right) \right]. \quad (29)$$

Considering the electrostatic relation between the electric field and the electric potential as:

$$\tilde{\mathbf{E}} = -\vec{\nabla} \tilde{\Psi}, \quad (30)$$

equation (29) becomes:

$$\tilde{\mathbf{f}}_E = \vec{\nabla} \cdot \left[ \varepsilon \left( (-\vec{\nabla} \tilde{\Psi}) \otimes \tilde{\mathbf{E}} - \frac{1}{2} (\tilde{\mathbf{E}} \cdot \tilde{\mathbf{E}}) [I] \right) \right]. \quad (31)$$

Due to the Gauss law determined in equation (16) equation (31) can be rewritten as:

$$\tilde{f}_E = \tilde{\rho}_E \tilde{E} - \frac{(\tilde{E} \cdot \tilde{E})}{2} \vec{\nabla} \varepsilon, \quad (32)$$

and, for the constant mixture permittivity:

$$\tilde{f}_E = \tilde{\rho}_E \tilde{E} = -F \left( \sum_{i=1}^n z_i \tilde{c}_i \right) \vec{\nabla} \tilde{\Psi}. \quad (33)$$

Substituting the mixture electric body force expression (33) into the momentum equation (27), we get:

$$\rho \left( \frac{\partial \tilde{u}}{\partial t} + \tilde{u} \cdot \vec{\nabla} \tilde{u} \right) = -\vec{\nabla} \tilde{P} + \eta \nabla^2 \tilde{u} - F \left( \sum_{i=1}^n z_i \tilde{c}_i \right) \vec{\nabla} \tilde{\Psi}. \quad (34)$$

The electric potential in this physical model is derived from the Gauss law (16), being one of the four Maxwell equations. Using the space charge density definition determined in equation (18), and assuming a constant value of absolute permittivity, the Gauss law satisfies the Poisson's equation:

$$\nabla^2 \tilde{\Psi} = -\frac{F}{\varepsilon} \left( \sum_{i=1}^n z_i \tilde{c}_i \right). \quad (35)$$

To get a closed form of the overall set of equations, the Nernst-Planck equation (20-21) for incompressible flow is written as:

$$\frac{\partial \tilde{c}_i}{\partial t} + \tilde{u} \cdot \vec{\nabla} \tilde{c}_i = \vec{\nabla} \cdot \left[ D_i \vec{\nabla} \tilde{c}_i + \left( D_i \frac{z_i e}{k_B T} \vec{\nabla} \tilde{\Psi} \right) \tilde{c}_i \right]. \quad (36)$$

The last term in this equation is named the "electromigration term" [28]. This term represents the transport of charged species due to an electric field and can be further rewritten as a standard convective term:

$$\tilde{S}_i = \vec{\nabla} \cdot \left[ \left( D_i \frac{z_i e}{k_B T} \vec{\nabla} \tilde{\Psi} \right) \tilde{c}_i \right] = \vec{\nabla} \cdot \left[ (\mu_i \vec{\nabla} \tilde{\Psi}) \tilde{c}_i \right] = \vec{\nabla} \cdot (\tilde{u}_{M,i} \tilde{c}_i), \quad (37)$$

where  $\mu_i$  is the electrical mobility of species  $i$  and  $\tilde{u}_{M,i}$  is the vector of electromigration velocity determining the relative velocity between the fluidic carrier and the corresponding ionic species  $i$ . However, this term may also be considered as the Laplacian operator applied to the electric potential field  $\tilde{\Psi}$ .

In order to derive an expression for the electromigration term determined in equation (37), it is necessary to know the electrical mobility equation for the diffusion of charged particles:

$$D_i = \frac{\mu_i k_B T}{|z_i| e}. \quad (38)$$

Alternatively, the  $i^{\text{th}}$  species diffusion coefficient can be derived by the Stokes-Einstein equation for the diffusion of spherical particles within a liquid with a low relative velocity-based Reynolds number:

$$D_i = \frac{k_B T}{6\pi\eta r_i}, \quad (39)$$

where  $r_i$  is the average radius of the  $i^{\text{th}}$  spherical particle species. Both equations (38) and (39) are known as "Einstein relations" [72].

To solve the set of the coupled time and space dependent partial differential equations (PDEs), initial conditions (ICs) and boundary conditions (BCs) should be obtained. The IC for species concentration in the case of an electrolyte bounded by two parallel electrodes satisfies the electroneutrality condition [73]:

$$\sum_{i=1}^n z_i \tilde{c}_i = 0. \quad (40)$$

Four types of BCs are implemented in this work:

1. Dirichlet BC – specifies a constant value of the dependent variable on the boundary.
2. Neumann BC – specifies the value for which the derivative of the dependent variable is set on the boundary domain, in its normal direction. For example,  $\vec{\nabla} \tilde{P} \cdot \hat{n} = 0$  specifies a zero gradient BC for the pressure variable  $\tilde{P}$ , where  $\hat{n}$  is a unit vector perpendicular to the boundary.
3. Robin BC – specifies a relationship between the dependent variable and its derivative normal to the boundary domain. For example,  $\vec{J}_i \cdot \hat{n} = 0$  specifies a zero ionic flux BC, where both  $c_i$  and  $\vec{\nabla} c_i$  are connected.
4. Periodic BC – specifies the value of the dependent variable on the certain boundary as the value of the same dependent variable on the opposite boundary.

An important parameter which can be calculated when running the numerical simulation is the total surface-averaged electric current density (positively signed electric current per unit area) passing through a plane parallel to the applied voltage boundaries and placed at height  $\tilde{y}_0$  from the bottom boundary [73-74]:



$$\tilde{I}_y = \left| \frac{1}{2L} \int_{-L}^L \left[ F \left( \sum_{i=1}^n z_i (\tilde{J}_i)_y \right) - \varepsilon \frac{\partial^2 \tilde{\Psi}}{\partial \tilde{y} \partial \tilde{t}} \right] \right|_{\tilde{x}, \tilde{y}=\tilde{y}_0, \tilde{t}} d\tilde{x}, \quad (41)$$

where  $2L$  is the length of the above-mentioned plane in the horizontal  $x$  direction and  $(\tilde{J}_i)_y$  is the  $y$  component of the ionic flux vector of the  $i^{\text{th}}$  species defined by equation (21). The first term in the above expression corresponds to the charged species passing through the given plane, while the second term corresponds to the displacement current density and accounts for the time-varying electric field. To better understand the meaning of the above calculation, let us consider an elementary charge moving from point A to point B within the computational domain. If our amperemeter is located outside the zone between A and B, there will be no flux contribution to the calculation. However, as follows from equation (35), the charge transport will change the electric field within the domain, which will be reflected by measurement of an electric current made by the amperemeter.

Generally, the mixture equivalent properties and the volume or mass fractions determined in equations (8), (1), and (15), respectively, are space and time dependent functions. Moreover, the governing equations, including the conservation of mass (26), momentum (34), species (36), and the Gauss law (35), are two-way coupled when employing the PNP model. As can be seen, the physical model, even not accounting for the particle charging kinetics, Van der Waals forces, and Brownian motion is still very complicated. Hence, dimensional analysis is next performed to reduce the number of parameters that determine the physics of the problem under consideration.

## 5.1 Dimensional Analysis

Dimensional analysis is a mathematical process that aims to determine non-dimensional groups governing the problem under consideration. The process starts with identifying scales of the problem and is followed by algebraic transformations of the governing equations. Finally, the non-dimensional governing equations, together with all the non-dimensional groups, are obtained. This chapter suggests ways of normalizing the problem parameters for two different configurations:

1. A configuration with two stationary horizontal boundaries.
2. A configuration with one horizontal boundary moving with constant velocity in the  $x$  direction, while another horizontal boundary is stationary.

Both configurations operate with an electrolyte consisting of  $n$  charged species.

The scales defined will be substituted into equations (20-21,26,34-35,41) providing the set of non-dimensional groups.

### 5.1.1 First Configuration

For the configuration characterized by stationary boundaries, the characteristic scales are of the form [35,51]:

$$t_0 = \frac{l_0^2}{D^+}, \quad V_T = \frac{k_B T}{z^+ e}, \quad u_0 = \frac{\varepsilon}{\eta l_0} V_T^2, \quad P_0 = \frac{\eta u_0}{l_0}, \quad J_0 = \frac{D^+ c_0^+}{l_0}, \quad I_0 = \frac{F z^+ D^+ c_0^+}{l_0}, \quad (42)$$

where  $t_0$  is the diffusion time,  $l_0$  is the geometric characteristic length,  $V_T$  is the thermal voltage,  $c_0^+$  is the initial bulk concentration of cation species,  $u_0$ ,  $P_0$ ,  $J_0$ , and  $I_0$  are characteristic velocity, pressure, ionic flux, and current density, respectively, and superscript sign  $^+$  refers to positive cation species. Utilizing the above scaling, one can obtain the non-dimensional variables:

$$t = \frac{\tilde{t}}{t_0}, \quad \vec{x} = \frac{\tilde{x}}{l_0}, \quad \vec{u} = \frac{\tilde{u}}{u_0}, \quad c_i = \frac{\tilde{c}_i}{c_0^+}, \quad P = \frac{\tilde{P}}{P_0}, \quad \Psi = \frac{\tilde{\Psi}}{V_T}, \quad \vec{J}_i = \frac{\tilde{J}_i}{J_0}, \quad I_y = \frac{\tilde{I}_y}{I_0}, \quad (43)$$

where  $\vec{x}$  corresponds to the spatial coordinate. We next substitute the expressions that appear in equations (42-43) into the governing equations of the physical model (as detailed in appendix A), yielding non-dimensional governing equations as explained below.

The mass conservation equation for incompressible flow is of the form:

$$\vec{\nabla} \cdot \vec{u} = 0. \quad (44)$$

The momentum conservation equation is of the form:

$$\frac{1}{Sc} \left( \frac{\partial \vec{u}}{\partial t} + Pe \vec{u} \cdot \vec{\nabla} \vec{u} \right) = -\vec{\nabla} P + \nabla^2 \vec{u} - \frac{1}{2 \epsilon^2} \left( \sum_{i=1}^n z_{r_i} c_i \right) \vec{\nabla} \Psi, \quad (45)$$

where the non-dimensional numbers  $Sc$ ,  $Pe$ ,  $\epsilon$ , and  $z_{r_i}$  are determined in section 5.1.3.

Poisson's equation for the electric potential is of the form:

$$-2 \epsilon^2 \nabla^2 \Psi = \sum_{i=1}^n z_{r_i} c_i. \quad (46)$$

The species conservation Nernst-Planck equation is of the form:

$$\frac{\partial c_i}{\partial t} = -\vec{\nabla} \cdot \vec{J}_i, \quad (47)$$

where  $\vec{J}_i$  is the non-dimensional ionic flux of the  $i^{\text{th}}$  species for isothermal flow:

$$\vec{J}_i = Pec_i \vec{u} - D_{r_i} \vec{\nabla} c_i - D_{r_i} z_{r_i} c_i \vec{\nabla} \Psi, \quad (48)$$

where the non-dimensional number  $D_{r_i}$  is determined in section 5.1.3.

The equation for the non-dimensional surface-averaged electric current density in the  $y$  direction is of the form:

$$I_y = \left| \frac{1}{AR} \int_{AR} \left[ \left( \sum_{i=1}^n z_{r_i} (J_i)_y \right) - 2 \epsilon^2 \frac{\partial^2 \Psi}{\partial y \partial t} \right]_{x, y=y_0, t} dx \right|, \quad (49)$$

where the aspect ratio  $AR$  is determined in section 5.1.3. In summary, the first form of a non-dimensional set of governing equations is:

$$\begin{aligned} \vec{\nabla} \cdot \vec{u} &= 0 \\ \frac{1}{Sc} \left( \frac{\partial \vec{u}}{\partial t} + Pec \vec{u} \cdot \vec{\nabla} \vec{u} \right) &= -\vec{\nabla} P + \nabla^2 \vec{u} - \frac{1}{2 \epsilon^2} \left( \sum_{i=1}^n z_{r_i} c_i \right) \vec{\nabla} \Psi \\ -2 \epsilon^2 \nabla^2 \Psi &= \sum_{i=1}^n z_{r_i} c_i \\ \frac{\partial c_i}{\partial t} &= -\vec{\nabla} \cdot \vec{J}_i \\ \vec{J}_i &= Pec_i \vec{u} - D_{r_i} \vec{\nabla} c_i - D_{r_i} z_{r_i} c_i \vec{\nabla} \Psi. \end{aligned} \quad (50)$$

### 5.1.2 Second Configuration

For a 2D configuration characterized by a moving boundary, its velocity  $u_{wall}$  is utilized to scale the time, velocity vector, and pressure fields, as well as the species ionic flux and current density. In such a case, the characteristic length  $H$  refers to the distance between the two parallel electrodes. For a 3D configuration characterized by a moving boundary, the characteristic velocity  $u_{av}$  and length  $D_H$  are defined as the average inlet velocity due to the flow rate of the mixture and the hydraulic diameter of the rectangular duct, respectively:

$$D_H = \frac{4A}{p}, \quad (51)$$

where  $A$  and  $p$  are the cross-section area and wetted perimeter of the duct, respectively.

The characteristic scales of the moving boundary configuration which differ from the stationary boundary configuration, are of the form:

$$t_0 = \frac{l_0}{u_0}, \quad P_0 = \rho u_0^2, \quad J_0 = c_0^+ u_0, \quad I_0 = F z^+ c_0^+ u_0, \quad (52)$$

where

$$l_0 = (H)_{2D} \text{ or } (D_H)_{3D}, \quad u_0 = (u_{wall})_{2D} \text{ or } (u_{av})_{3D} \quad (53)$$

are the characteristic length and velocity for 2D or 3D configurations, respectively, and  $t_0$  is the characteristic time.

We next substitute the expressions that appear in equations (52-53) and (43) into the governing equations of the physical model (as detailed in appendix A), yielding non-dimensional governing equations as explained below.

The non-dimensional mass conservation for incompressible flow, Poisson equation for the electric potential, Nernst-Planck equation for the species concentration and the calculation for current density in the  $y$  direction, all remain the same as written in (44,46,47) and (49), respectively.

The momentum conservation equation is of the form:

$$\frac{\partial \vec{u}}{\partial t} + \vec{u} \cdot \vec{\nabla} \vec{u} = -\vec{\nabla} P + \frac{1}{Re} \nabla^2 \vec{u} - \frac{\kappa}{2 \epsilon^2 Re^2 Sc} \left( \sum_{i=1}^n z_{r_i} c_i \right) \vec{\nabla} \Psi, \quad (54)$$

where the non-dimensional numbers  $Re$  and  $\kappa$  are determined in section 5.1.3.

The non-dimensional ionic flux of the  $i^{th}$  species for isothermal flow is defined as:

$$\vec{J}_i = c_i \vec{u} - \frac{D_{r_i}}{Re Sc} \left( \vec{\nabla} c_i + z_{r_i} c_i \vec{\nabla} \Psi \right). \quad (55)$$

In summary, the second form of a non-dimensional set of governing equations is:

$$\begin{aligned}
\vec{\nabla} \cdot \vec{u} &= 0 \\
\frac{\partial \vec{u}}{\partial t} + \vec{u} \cdot \vec{\nabla} \vec{u} &= -\vec{\nabla} P + \frac{1}{Re} \nabla^2 \vec{u} - \frac{\kappa}{2 \epsilon^2 Re^2 Sc} \left( \sum_{i=1}^n z_{r_i} c_i \right) \vec{\nabla} \Psi \\
-2 \epsilon^2 \nabla^2 \Psi &= \sum_{i=1}^n z_{r_i} c_i \\
\frac{\partial c_i}{\partial t} &= -\vec{\nabla} \cdot \vec{J}_i \\
\vec{J}_i &= c_i \vec{u} - \frac{D_{r_i}}{Re Sc} \left( \vec{\nabla} c_i + z_{r_i} c_i \vec{\nabla} \Psi \right).
\end{aligned} \tag{56}$$

Note that the sets of equations (50,56) formulated for the general non-symmetric electrolyte consisting of  $n$  charged species are straight-forwardly reduced to the system governing the EC of a symmetric binary electrolyte by setting  $n = 2$ ,  $z_{r1} = -z_{r2} = 1$ , and  $D_{r1} = D_{r2} = 1$ , where the indices 1 and 2 refer to the cation and anion species, respectively.

### 5.1.3 Non-Dimensional Numbers

This section describes the non-dimensional groups derived in the previous sections.

The Reynolds number ( $Re$ ) is the ratio between the inertial and viscous forces of the flow. At low Reynolds numbers, the flow tends to be laminar because of the relatively high viscous force. At high Reynolds numbers, the flow tends to be turbulent because of the relatively high inertial force. The transition between "low" and "high" Reynolds number flows is not unique and it depends on the geometry. The Reynolds number is defined as:

$$Re = \frac{\rho u_0 l_0}{\eta}. \tag{57}$$

The Schmidt number ( $Sc$ ) is the ratio between the viscous diffusion rate and molecular mass diffusion rate. Viscous diffusion is responsible for the diffusion of momentum in the fluid, while molecular mass diffusion tends to prevent the local accumulation of species to minimize the state of internal energy. The Schmidt number is defined as:

$$Sc = \frac{\nu}{D^+} = \frac{\eta}{\rho D^+}, \tag{58}$$

where  $\nu$  is the kinematic viscosity of the mixture.

The Péclet number ( $Pe$ ) is the ratio between the advective and diffusive rates of species transport within the flow. At low Péclet numbers, species transport is dominated by the molecular

diffusion mechanism. At high Péclet numbers, species transport is dominated by the flow advection mechanism. The Péclet number is defined as:

$$Pe = \frac{u_0 l_0}{D^+}. \quad (59)$$

The electrohydrodynamic coupling constant ( $\kappa$ ) is the ratio between the electric and hydrodynamic forces. At a low value of  $\kappa$ , the EDF is dominated by viscous and molecular diffusion forces. At high  $\kappa$  numbers, the EDF is dominated by electric forces acting on the ions within the solution. The electrohydrodynamic coupling constant is defined as [57]:

$$\kappa = \frac{\varepsilon}{\eta D^+} \cdot V_T^2 = \frac{\varepsilon}{\eta D^+} \left( \frac{k_B T}{z^+ e} \right)^2. \quad (60)$$

One should note that the Péclet number and the electrohydrodynamic coupling constant are identical if the characteristic velocity determined in equation (42) for the configuration with stationary boundaries is used in equation (59) instead of  $u_0$ .

The non-dimensional electrostatic screening length ( $\epsilon$ ) is the ratio between the Debye length  $\lambda_D$  and the characteristic length  $l_0$ . The Debye length is the characteristic thickness of an EDL and it used to measure its spatial extent [8,75-76]. The Debye length is defined as [8,76]:

$$\lambda_D = \sqrt{\frac{\varepsilon k_B T}{2(z^+ e)^2 c_0^+ N_A}}. \quad (61)$$

Figure 9 illustrates the Gouy-Chapman model of an EDL that helps to understand the meaning of Debye length (or electrostatic screening length) [77]:

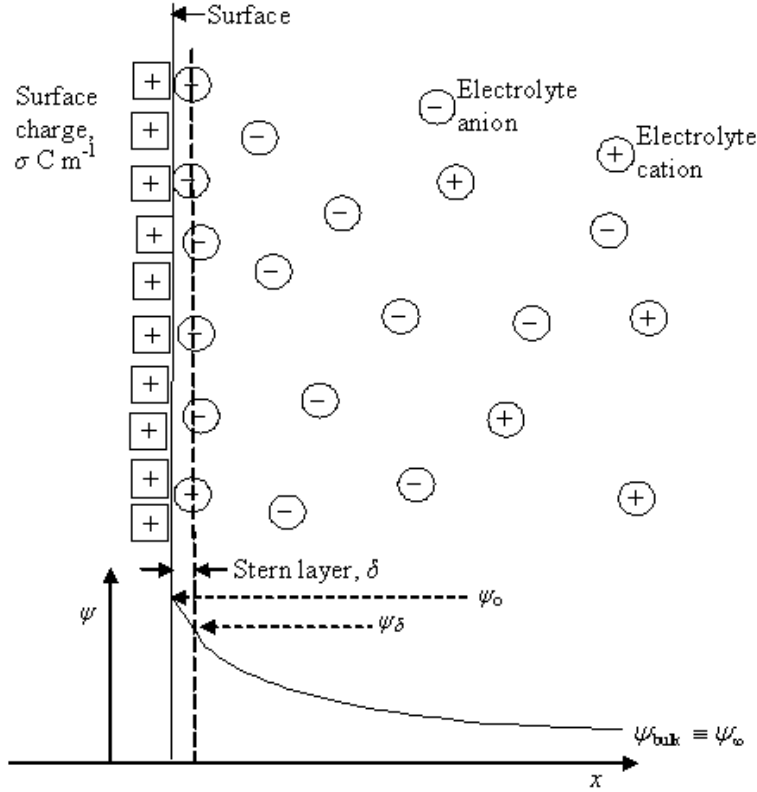


Figure 9: Gouy-Chapman model for EDL. Electric potential decays exponentially when moving away from the charged surface.

The Debye length (or electrostatic screening length) is responsible for the curve-shaped decay of the electric potential. The smaller the Debye length, the steeper is the exponential curve of the electric potential, which corresponds to the existence of a large potential gradient in the direction perpendicular to the surface. In other words, a small value of the Debye length indicates the dominant role of the electric field screening effect. The non-dimensional electrostatic screening length is defined as:

$$\epsilon = \frac{\lambda_D}{l_0} = \frac{l}{l_0} \sqrt{\frac{\epsilon k_B T}{2(z^+ e)^2 c_0^+ N_A}}. \quad (62)$$

The non-dimensional voltage ( $V$ ) corresponds to the Dirichlet BC of the electric potential and is defined as the overall electric potential difference  $\Delta V$  between two opposite boundaries, normalized by the thermal voltage  $V_T$ :

$$V = \frac{\Delta V}{V_T}. \quad (63)$$

In the case of stationary boundaries containing a symmetric binary electrolyte, the non-dimensional electrostatic screening length and voltage,  $\epsilon$  and  $V$ , fully characterize charging and discharging dynamics of the electrolytic cell [75].

The valence ratio ( $z_{r_i}$ ) is defined as the valence of the  $i^{th}$  species normalized by the valence of the cation species. Considering a symmetric binary electrolyte consisting of positive and negative ions, the valence ratio of anions equals -1. For a multispecies electrolyte, a high absolute value of the valence ratio corresponds to a highly charged  $i^{th}$  species. The valence ratio is defined as:

$$z_{r_i} = \frac{z_i}{z^+}. \quad (64)$$

The molecular diffusivity ratio ( $D_{r_i}$ ) is defined as the molecular diffusion coefficient of the  $i^{th}$  species normalized by the molecular diffusion coefficient of the cation species. Considering a symmetric binary electrolyte consisting of positive and negative ions, the diffusivity ratio of anions equals 1. For a non-symmetric electrolyte, a high value of the diffusivity ratio refers to highly transported  $i^{th}$  species due to molecular diffusion phenomenon. The diffusivity ratio is defined as:

$$D_{r_i} = \frac{D_i}{D^+}. \quad (65)$$

As defined above, the non-dimensional electrostatic screening length ( $\epsilon$ ) controls the initial bulk value of cation concentration. Considering an electrolyte that contains more than two species, the ratio between the initial bulk concentrations of the remaining species should be additionally introduced. In this work, we consider a non-symmetric electrolyte consisting of a single positively charged species of valence  $z^+$  and two negatively charged species of valences  $z^-$  and  $Mz^-$ , respectively, where  $M$  is any positive integer number. The species are denoted by subscripts  $i = 1, 2, 3$  corresponding to the cation species of valence  $z^+$ , the anion species of valence  $z^-$ , and the third negatively charged species of valence  $Mz^-$ , respectively. The non-dimensional bulk concentration ratio  $c_r$  is defined as:

$$c_r = \frac{c_3}{c_2} \quad \text{at } t = 0. \quad (66)$$

Regarding to the above-mentioned electrolyte composition, the non-dimensional form of the electroneutrality condition determined in equation (40) is given by:

$$c_1 + z_{r2}c_2 + Mz_{r2}c_r c_2 = 0. \quad (67)$$



The values of the electrostatic screening length ( $\epsilon$ ), valence ratio ( $z_i$ ), and the bulk concentration ratio ( $c_i$ ), in addition to the electroneutrality condition (67), determine the ICs for the concentration fields of the species.

The aspect ratio ( $AR$ ) of a rectangular computational domain is defined as the ratio of its longer to its shorter edge lengths. A high aspect ratio of the computational grid cell may cause numerical artifacts.

## **6. Solution of a Simplified Physical Model**

The equations governing the physical model relevant to the present study can be solved either analytically or numerically. An analytical solution typically relies on several basic assumptions (e.g. an assumption of laminar flow and the existence of a fully developed flow region), which significantly simplifies the governing equations. In contrast, numerical simulation can address more general flow configurations. This chapter contains results obtained by both analytical solutions and numerical simulations. Several canonical flow configurations are addressed with the purpose of getting acquainted with the fundamental physical phenomena typical of EDFs and benchmarking the utilized numerical solver.

### **6.1 Analytical Approach**

The simplified physical model considered in this section does not take into account the impact of the concentration of charged species on the electric field. Under this assumption, there is no need to solve Poisson's equation for the electric potential (35), as well as the term for the mixture electric body force defined in equation (33). As a result, the concentration of charged species is not coupled with the electric field. Therefore, the electric field is only a function of the electric potential difference applied to the boundaries, while its impact on the momentum of the fluid/mixture is neglected (i.e. one-way coupling is assumed). This section contains analytical solutions for three flow configurations characterized by increasing complexity:

1. One phase Couette-Poiseuille flow between two parallel plates without the action of an electric field.
2. Mixture flow through a curved duct without the action of an electric field. The mixture is composed of a fluid and a solid particle species.
3. Mixture flow through a curved duct under the action of a constant electric field approximated by a given expression. The mixture is composed of a fluid and a solid particle species.

#### **6.1.1 One Phase Couette-Poiseuille Flow**

Considering the Couette-Poiseuille flow, it is possible to obtain an analytical solution for the velocity profile in the fully developed region. Comparison of the analytical solution with the results obtained by numerical simulations serves as a verification of the numerical solver. Couette-Poiseuille flow between static and moving parallel plates is presented in figure 10.

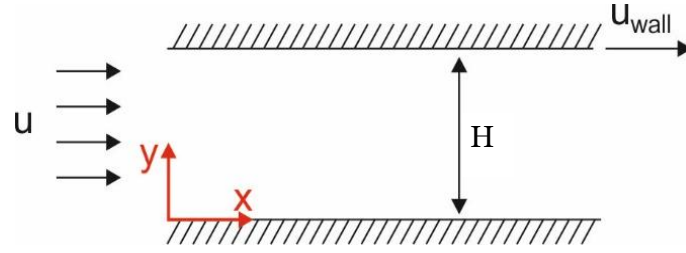


**Figure 10: Schematic description of Couette-Poiseuille flow between two parallel plates.**

The velocity field is obtained by the solution of the dimensional mass and the momentum conservation equations. In the absence of charged species and an electric field, no body force exists. In the following analytical approach, the velocity vector  $\tilde{u}$  and the flow properties appearing in equations (26-27) and in equation (27), respectively, refer to the fluid rather than to the mixture. Mass and momentum conservation equations for Couette-Poiseuille flow are solved under the following assumptions:

- Single-phase flow.
- Isothermal flow: constant fluid temperature. The energy conservation equation is not solved.
- Incompressible flow: fluid density is constant in space and time.
- Fully developed laminar flow: there is no velocity gradient in the  $x$  direction. There is no velocity component in the  $y$  direction.
- 2D case: no dependence on  $z$  coordinate.
- Steady state flow: no dependence on time.
- Newtonian fluid: shear stresses are proportional to the flow strain.
- Constant fluid dynamic viscosity.
- There are no body forces (gravitational force is negligible).

The mass (26) and momentum (27) conservation equations formulated in Cartesian and cylindrical coordinates, along with the analytical solution of the equations for the case of Couette-Poiseuille flow are detailed in appendices B-C, respectively.

The velocity profile analytically obtained under the assumption of a fully developed region is:

$$\tilde{u}_x(\tilde{y}) = A\tilde{y}^2 + c_1\tilde{y} + c_2, \quad (68)$$

where  $A \equiv \frac{1}{2\eta} \frac{\partial \tilde{P}}{\partial \tilde{x}}$  and constants  $c_1, c_2$  depend on the BCs.

The BCs for the configuration shown in figure 10 are:

$$\begin{aligned}\tilde{u}_x(\tilde{y} = 0) &= 0 \\ \tilde{u}_x(\tilde{y} = H) &= u_{wall},\end{aligned}\tag{69}$$

where  $H$  is the distance between the two parallel plates and  $u_{wall}$  is the velocity magnitude of the top moving wall. Substituting the BCs (69) into the solution of (68), the analytical velocity profile reads:

$$\tilde{u}_x(\tilde{y}) = A\tilde{y}^2 + \left(\frac{u_{wall}}{H} - HA\right)\tilde{y}.\tag{70}$$

Figure 11 illustrates the analytical solution obtained for different pressure gradient values.

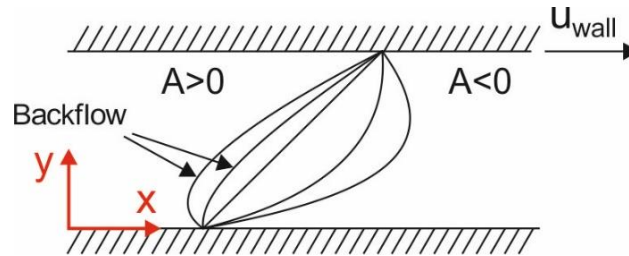


**Figure 11: Analytical velocity profile of a fully developed Couette-Poiseuille flow between two parallel plates, for different pressure gradient values.**

As can be seen from figure 11, positive pressure gradient values may result in the existence of a backflow zone.

### 6.1.2 Mixture Flow Through a Curved Duct Without the Action of an Electric Field

Considering a mixture flow composed of two species in the absence of an electric field, it is possible to obtain an analytical solution for the velocity and concentration profiles in the fully developed region. To do this, one should solve the incompressible mass (26) and the momentum (27) conservation equations for the velocity field, along with the species conservation equation (13) for the secondary particle species. These equations are solved under the following assumptions:

- Isothermal flow: constant mixture temperature. The energy conservation equation is not solved.
- Incompressible flow: mixture density is constant in space and time.
- Fully developed laminar flow: there are no velocity and concentration gradients in the tangential direction. There is no velocity component in the radial direction.

- 2D case: no dependence on  $z$  coordinate.
- Steady state flow: no dependence on time.
- Newtonian fluid: shear stresses are proportional to the flow strain.
- Constant mixture dynamic viscosity.
- There are no body forces (gravitational force is negligible).
- Implementation of the mixture model: the momentum conservation equation (27) is solved for the mixture elements composing the two above-mentioned species. Therefore, the drag force between species is not considered.
- The molecular diffusion coefficient of the secondary particle species is constant.
- There is no concentration rate source  $S_i$  for the particles species.

Note that the conservation equations of mass, momentum, and species are coupled by the volume fraction of solid particles  $\alpha_s$  and by the mixture velocity  $\tilde{u}$ . The volume fraction of the particle species is necessary for the calculation of mixture properties introduced in equation (8), and influences the concentration value determined by equation (14), while the mixture velocity appears in all of the three conservation equations. However, fully developed laminar flow and constant property (density, dynamic viscosity, and mass diffusivity) assumptions decouple the above relations.

Analytical solutions of the mass (26), momentum (27), and species (13) conservation equations are detailed in appendix C.

The mixture velocity profile analytically obtained under the assumption of a fully developed flow region is:

$$\tilde{u}_\theta(\tilde{r}) = \frac{B\tilde{r}}{2} \left( \ln \tilde{r} - \frac{1}{2} \right) + c_1\tilde{r} + \frac{c_2}{\tilde{r}}, \quad (71)$$

where  $\tilde{r}$  is the radial coordinate,  $B \equiv \frac{1}{\eta} \frac{\partial \tilde{P}}{\partial \tilde{\theta}}$  and constants  $c_1, c_2$  depend on the BCs. The BCs for the configuration of the ME-DR gap shown in figure 6 are:

$$\begin{aligned} \tilde{u}_\theta(\tilde{r} = r_1) &= u_{\theta\_wall} \\ \tilde{u}_\theta(\tilde{r} = r_2) &= 0, \end{aligned} \quad (72)$$

where  $r_1$  and  $r_2$  are the radii of internal DR and external ME concentric boundaries, respectively, and  $u_{\theta\_wall}$  is the tangential velocity of the moving boundary.

Substituting the BCs determined in equation (72) into the solution of (71), the analytical mixture velocity profile reads:

$$\tilde{u}_\theta(\tilde{r}) = \frac{B\tilde{r}^2 \left[ r_2^2 \ln\left(\frac{\tilde{r}}{r_2}\right) - r_1^2 \ln\left(\frac{\tilde{r}}{r_1}\right) \right] + Br_1^2 r_2^2 \ln\left(\frac{r_2}{r_1}\right) + 2u_{\theta\_wall} r_1 (r_2^2 - \tilde{r}^2)}{2\tilde{r}(r_2^2 - r_1^2)}. \quad (73)$$

The particle concentration profile analytically obtained under the assumption of a fully developed flow region is:

$$\tilde{c}_s(\tilde{r}) = a_1 \ln \tilde{r} + a_2, \quad (74)$$

where the constants  $a_1, a_2$  depend on the BCs. Possible BCs for the concentration of the particle species are the Neumann BCs:

$$\begin{aligned} \frac{\partial \tilde{c}_s}{\partial \tilde{r}}(\tilde{r} = r_1) &= 0 \\ \frac{\partial \tilde{c}_s}{\partial \tilde{r}}(\tilde{r} = r_2) &= 0. \end{aligned} \quad (75)$$

Substituting the BCs determined in equation (75) into the solution of (74), the analytical particle concentration profile reads a constant value which does not depend on the radial coordinate:

$$\tilde{c}_s(\tilde{r}) = a_2. \quad (76)$$

### 6.1.3 Mixture Flow Through a Curved Duct Under the Action of Constant Electric Field Approximated by a Given Expression

As has been stated at the beginning of section 6.1, the mixture electric body force term determined in equation (33) is not considered in the current section of the simplified physical model. Also, decoupling assumptions regarding the governing conservation equations are given in section 6.1.2. For these reasons, the embedded electric field does not impact the mixture velocity profile, which remains as presented in equation (73). However, the concentration profile of the particle species is obtained by the Nernst-Planck equation (36), which includes the additional electromigration source term given by equation (37) for the species conservation equation (13). To perform the analytic solution, which accounts for an electric field, several additional assumptions are introduced:

- The electric field does not impact the mixture velocity field.
- Forces between the charged particles are neglected.

- Particle's charge does not impact the external electric field generated by the electric potential difference supplied to the electrode boundaries.
- The magnetic potential is negligible.
- The curved duct configuration displayed in figure 6 is approximated as a complete cylinder, in a way that allows addressing a symmetric Gaussian surface around it.
- The electric field is applied in the radial direction only.
- Constant valence of the charged particles.

As can be seen from equations (30,36), species concentration depends on the electric field  $\tilde{E}$ . The simplest expression for the electric field vector is obtained by plotting a symmetric Gaussian surface around the approximated cylindrical geometry and performing the integral form of Gauss's law [78]:

$$\tilde{\Phi} = \oint_{\tilde{A}} \tilde{E} \cdot \hat{n} d\tilde{A} = \frac{\tilde{Q}_m}{\epsilon_0}, \quad (77)$$

where  $\tilde{\Phi}$  is the electric flux through the Gaussian surface,  $\hat{n}$  is a unit vector perpendicular to the Gaussian surface (directed out),  $\tilde{A}$  is the Gaussian surface area, and  $\tilde{Q}_m$  is the net charge enclosed within the Gaussian surface.

Analytical solutions of Gauss's law determined in equation (77) and the Nernst-Planck equation (36) are detailed in appendix C. Utilizing Gauss's law, the expression obtained for the electric field vector is:

$$\tilde{E}(\tilde{r}) = \frac{\Delta\tilde{V}}{\tilde{r} \ln\left(\frac{r_2}{r_1}\right)} \hat{r}, \quad (78)$$

where  $\hat{r}$  is a radial unit vector directed from the internal  $r_1$  to the external  $r_2$  boundaries.

The particle concentration profile analytically obtained under the assumption of a fully developed flow region is:

$$\tilde{c}_s(\tilde{r}) = a_1 \tilde{r}^G + a_2, \quad (79)$$

where  $G \equiv \frac{z_s e \Delta\tilde{V}}{k_B T \ln\left(\frac{r_2}{r_1}\right)}$  and constants  $a_1, a_2$  depend on the BCs. The BCs for the configuration shown in figure 6 are:

$$\begin{aligned}\tilde{c}_s(\tilde{r} = r_1) &= c_{\max} \\ \tilde{c}_s(\tilde{r} = r_2) &= 0,\end{aligned}\tag{80}$$

where  $c_{\max}$  is a constant.

Substituting the BCs determined in equation (80) into the solution of (79), the analytical particle concentration profile reads:

$$\tilde{c}_s(\tilde{r}) = \frac{c_{\max}(\tilde{r}^G - r_2^G)}{(r_1^G - r_2^G)}.\tag{81}$$

Given different  $G$  values, figure 12 illustrates the result of the normalized concentration of particles. Note that the particles are negatively charged. Therefore, their valence value  $z_s$  is negative, and so is  $G$ .

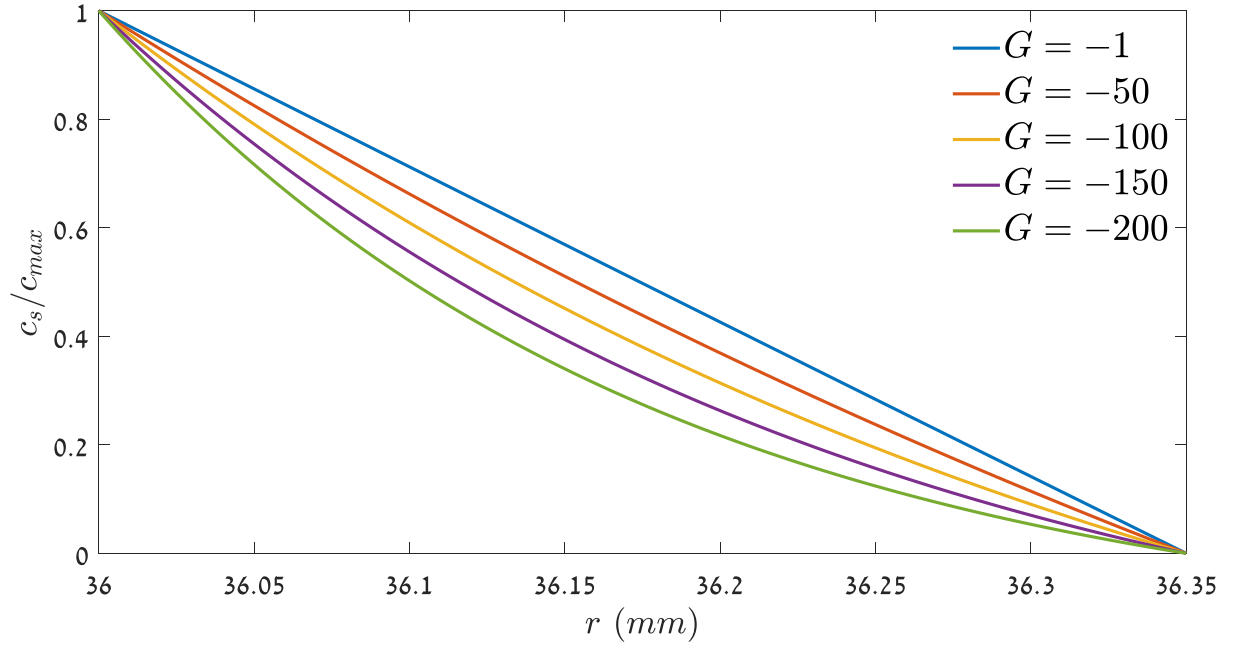


**Figure 12:** Normalized particle concentration as a function of the duct radius for different  $G$  values.

- Note that for absolute  $G$  values larger than 200, the computer memory limitation does not allow to display the corresponding curve, although the solution is physical.

## 6.2 Numerical Approach

Unfortunately, there is an essential difficulty in performing an analytic solution of the equations governing the motion of general incompressible Newtonian flows. An analytical solution may



be achieved for a few configurations only, relating to the fully developed flow region under a number of basic assumptions. The main reason for this difficulty is the non-linear physics of the Navier-Stokes (NS) equation, responsible for the momentum conservation of the flow. Moreover, the challenge is even greater when dealing with multiphase flows. Therefore, performing numerical simulations of the flow field is necessary. The numerical solution can be performed by utilizing several commercial packages, as well as open-source software. These programs enable simulation of flows with given BCs and ICs. Over the years the packages have been upgraded significantly, and nowadays it is possible to simulate multi-physics phenomena, including the motion of particles, and to account for the impact of different fields (e.g. electric, magnetic and gravitational fields), chemical reactions, heat transfer, combustion, etc. The field encompassing all these numerical capabilities is called computational fluid dynamics (CFD).

Examples of CFD programs:

- Ansys programs: Workbench, Fluent, CFX
- OpenFOAM
- RheoTool
- Comsol.

Examples of additional computing resources:

- Mathematic computational programs: Matlab, Mathematica
- Programming languages: C, C++, Java, Fortran, Python.

Each of the above programs has various utilities and requires training and experience. For the simplified physical model solution, Ansys Workbench and Fluent programs (version 18.2) were employed. The main reasons that led to this choice are:

- Intuitive graphical user interface (GUI).
- The mixture method is utilized and verified in the program (species transport model).
- Advanced geometry and mesh features.
- An available student addition in the academic institute.

The main disadvantages of Ansys Fluent are the difficulties with verifying the simulation results (Fluent is not an open-source program) and the need for using the magnetohydrodynamics (MHD) module to include electric equations.

Another program used in this work for calculations, verification, and presentation of results is Matlab. BGU purchased licenses for these programs, and they are installed on the laboratory's computers and clusters.

### **6.2.1 Ansys Fluent Program**

Ansys Fluent operates with the finite volume (FV) method, in which the domain is divided into many small control volume cells. According to the chosen physical model, conservation equations are solved in their integral form for each control volume cell. Following the FV formalism, the values of the unknown variables are calculated at the cell centroids during each numerical iteration or time step. Over the simulation process, errors related to rounding the irrational numbers, as well as errors originating from the discretization of geometry and truncation of the numerical schemes, can appear and further accumulate. If the simulation converges, some of these errors become smaller as the iterations progress.

The Workbench interface enables us to create geometry and grid, and to enter the Fluent program, look and process simulation results, and export data into text files, which can be read by Matlab.

Fluent is the solver which enables definition of the desirable physical model and its equations, and makes it possible to determine BCs and ICs, and to perform the iterations or time steps required by the numerical procedure.

### **6.2.2 Comparison Between Analytical and Numerical Results**

This section includes a comparison between the analytical solutions obtained in section 6.1 and numerical simulations results obtained by the Ansys Fluent program. All the numerical simulations utilize 2D geometries that were divided equally into 100,000 rectangular grid cells. The conservation equations of all the cases were solved in their steady state form and required approximately 2,200 iterations until convergence was achieved (the maximal residual value was  $10^{-6}$ ). The numerical simulations were executed on the lab's cluster, which is computationally powerful and yields results in reasonable time.

Figure 13 presents a comparison between the numerically and the analytically obtained results for the velocity profile of a single-phase Couette-Poiseuille flow in the fully developed region.

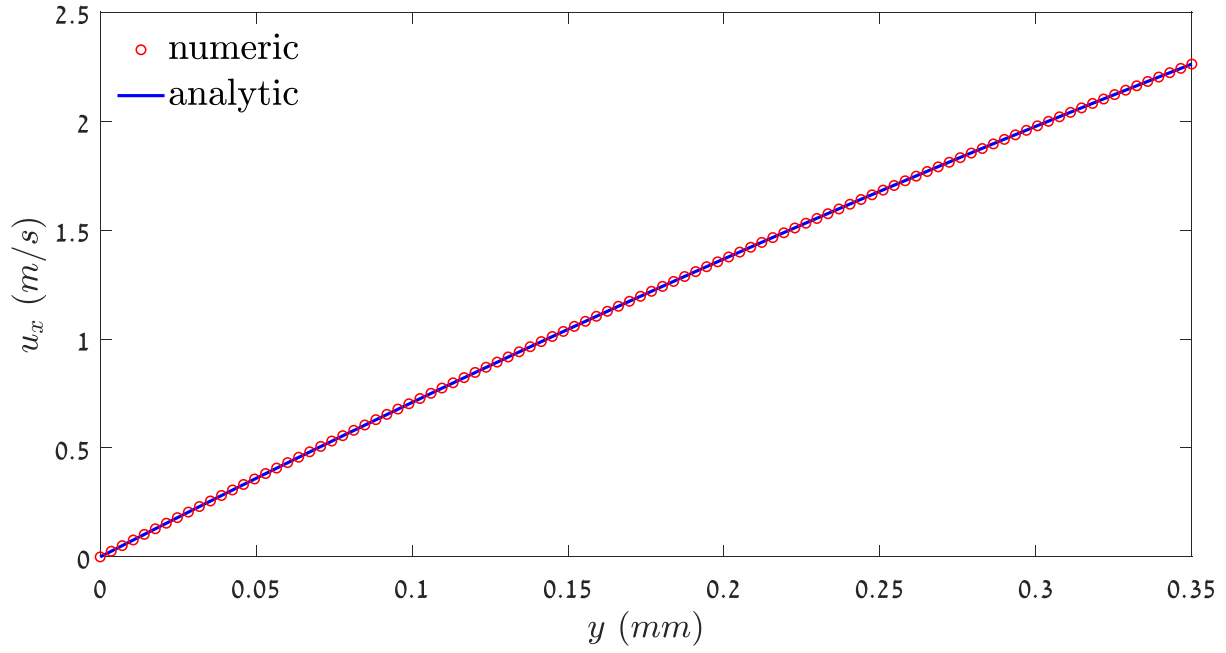


**Figure 13:  $x$  velocity component of the fully developed Couette-Poiseuille flow between two parallel plates. Analytical and numerical results.**

The analytical solution curve is marked by the blue color in figure 13, while 100 sample points located on a line perpendicular to the plates in the fully developed region represent the results obtained by the numerical simulation. The constants substituted into the analytic solution given by equation (70) were:

$$\begin{aligned}
 A &= \frac{1}{2\eta} \frac{\partial \tilde{P}}{\partial \tilde{x}} = \frac{1}{2 \cdot 0.0015} \cdot (-7516.2) = -2505400 \frac{1}{\text{m} \cdot \text{s}} \\
 u_{\text{wall}} &\approx \omega r_1 = 20\pi \cdot 36 \cdot 10^{-3} = 2.262 \text{ m/s} \\
 H &= r_2 - r_1 = 36.35 - 36 = 0.35 \text{ mm},
 \end{aligned} \tag{82}$$

while the pressure gradient in the  $x$  direction was estimated by a linear fit of the numerically obtained result in the fully developed flow region. The values of dynamic viscosity,  $\eta$ , wall velocity,  $u_{\text{wall}}$ , and the distance between plates,  $H$ , were taken from the configuration corresponding to HP Indigo's setup detailed in chapter 8. Figure 13 shows that the results obtained by Fluent for the given model and constant properties chosen are in good agreement with the analytical solution for the simple case of fully developed Couette-Poiseuille flow.

Figure 14 presents a comparison between the numerically and the analytically obtained results for the mixture velocity profile in the fully developed region, considering the curved duct shown in figure 6.

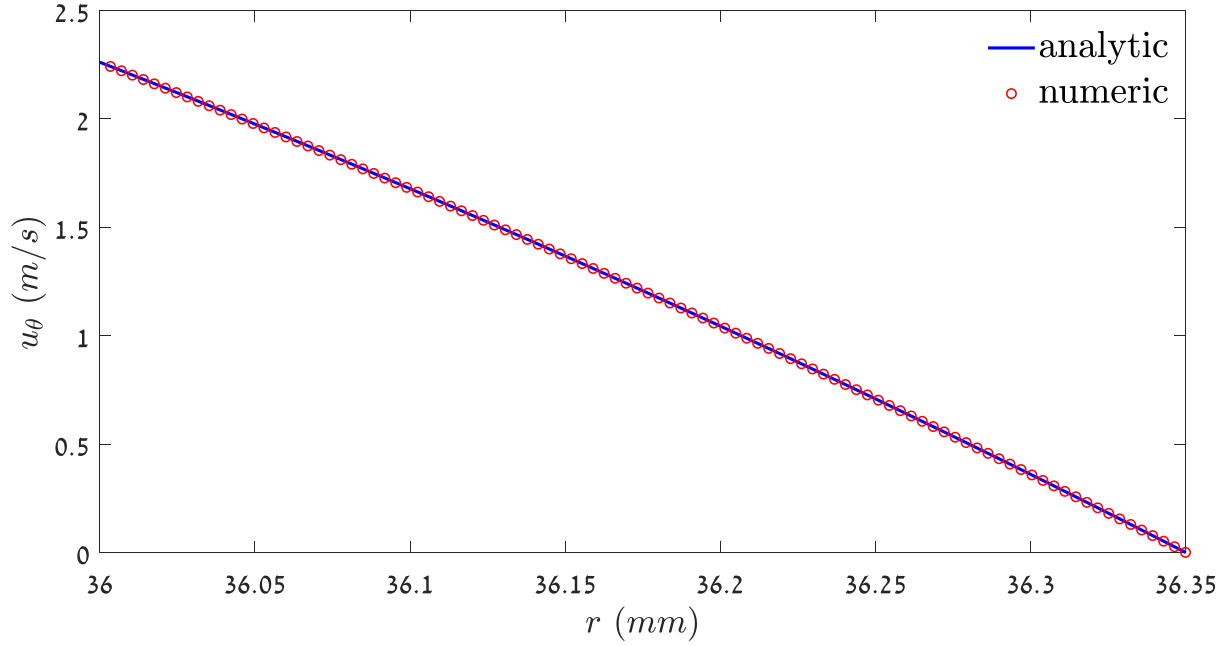


**Figure 14: Tangential velocity component of a fully developed mixture-flow through a curved duct. Analytical and numerical results.**

The analytical solution curve is marked by the blue color in figure 14, while 100 sample points located on a line perpendicular to the duct boundaries in the fully developed region represent the result obtained by numerical simulation. The constants substituted into the analytic solution given by equation (73) were:

$$B = \frac{1}{\eta} \frac{\partial \tilde{P}}{\partial \tilde{\theta}} = \frac{1}{0.0015} \cdot (-281.43) = -187620 \frac{1}{\text{s}} \quad (83)$$

$$u_{\theta\_wall} = \omega r_1 = 20\pi \cdot 36 \cdot 10^{-3} = 2.262 \text{ m/s} ,$$

while the tangential pressure gradient was estimated by a linear fit of the numerically obtained result in the fully developed flow region. The values of the dynamic viscosity of the mixture,  $\eta$ , and the wall velocity,  $u_{\theta\_wall}$ , were determined as in the previous case for a single-phase flow. Figure 14 demonstrates good agreement between the analytical and numerically obtained results, both based on the species transport model.

For an isothermal mixture in the absence of chemical reactions, equation (13) for the conservation of the  $i^{th}$  species is identical to the species transport model implemented in Fluent [17]. Figure 15 presents the concentration profile of the particle species obtained by numerical simulation in the fully developed region in the absence of an electric field.

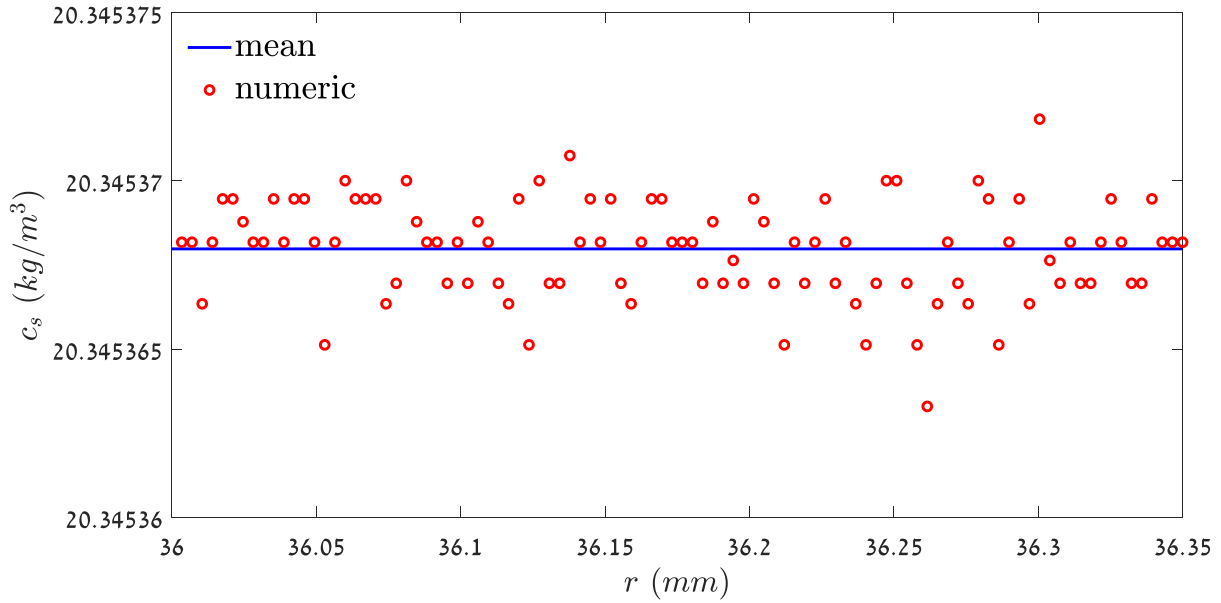


**Figure 15: Concentration profile of particle species obtained by numerical simulation in the fully developed region in the absence of an electric field.**

Figure 15 presents 100 sample points obtained by numerical simulation, located on a line perpendicular to the duct boundaries in the fully developed flow region. The average value of these sample points is marked by a blue line. It can be seen that the concentration of particles in the fully developed region is approximately constant along the radial direction, up to the fourth decimal digit. This result agrees with the analytical solution presented in equation (76).

When an electric field is applied, either by setting a potential difference between the electrode boundaries or by introducing the charged species, the electromigration source term determined in equation (37) should be added to the Fluent species transport model. To do so, one should compose a user-defined function (UDF), which is a block of code that performs a specific task. Another option is to purchase the MHD package mentioned in section 6.2.

## 7. Solution of the Two-Way Coupled Physical Model

In order to simulate the two-way coupled physical model that incorporates the mixture electric body force vector introduced in equation (33), the Poisson equation for the electric potential (35), and the electromigration source term determined in equation (37), it is worthwhile to consider an alternative numerical tool. In this work, the rheoTool open-source program (version 3) based on the popular openFOAM CFD program (version 6), was chosen [8,79]. The main reasons that led to this choice are:

- RheoTool is a free open-source program that is available online (see rheoTool user guide [28]).
- RheoTool has already implemented and cross-verified EDF models. The physical model described in chapter 5 for a Newtonian mixture flow, utilizing the PNP model, is available in this program.
- An available and easily editable tutorial of rheoTool resembles HP Indigo's case.
- RheoTool simulation can be executed in parallel with a message passing interface (MPI).

However, because rheoTool codes are already written, their further utilization at the developer level can be time consuming, especially when fundamental changes in the physical model are required.

### 7.1 CFD Software

OpenFOAM is a popular open-source CFD program that works on a Unix operating system. OpenFOAM has an extensive range of features for solving complex fluid flows involving chemical reactions, turbulence, heat transfer, acoustics, and solid mechanics. The CFD technique utilized within openFOAM is the FV method, which is the same as in Ansys Fluent. RheoTool is an open-source toolbox based on openFOAM which was designed to simulate generalized Newtonian fluids (GNF) and viscoelastic fluids under pressure-driven and/or electrically-driven flows. RheoTool features are available for 1D/2D/3D problems and generic grids. RheoTool has several solvers for different uses: rheoFoam, rheoTestFoam, rheoInterFoam, rheoEfoam, and rheoBDfoam [28]. The physical model equations given in chapter 5 will be solved with the rheoEfoam solver throughout this work, where "E" refers to the electric field. It enables a comprehensive solution of the two-way coupled PNP-NS equations, providing a mixture velocity vector field, a mixture pressure field, an electric potential field, and a concentration field for each of the  $n-1$  secondary species (see section 3.1.3). All the simulations were performed on a standard Unix server equipped with 2 Intel Xeon 12C Processors (Model E5-2697v2, 24 cores in total), and 128 GB RAM.

To contribute to an in-depth understanding of the governing physics and to validate the results obtained by the rheoEFoam solver, two intuitive and simply edited Matlab scripts were developed. Both programs account for a 1D configuration and utilize the PNP equations (35-36) only, while the advective term of the ionic flux  $\vec{J}_i$  containing the velocity of the electrolyte is simply equal to zero. The first Matlab program accounts for a transient state, providing various BC settings, while the second Matlab program addresses Newton-Raphson iterations of the coupled PNP equations yielding a steady state solution related to a membrane-bulk configuration (see in the following section).

Both rheoEFoam and Matlab simulations employ second-order standard spatial discretization of the differential operators [80], while the second-order backward difference is used for the time discretization. Since the system of PNP equations is intrinsically non-linear, internal iterations were introduced when solving equation (36) by the rheoEFoam solver and by the Matlab transient script. When utilizing the transient Matlab script, the convergence criterion for the internal PNP iterations was the value of  $10^{-8}$  of the  $L_2$  norm, calculated for the relative difference between the two consecutive iterations. When employing the rheoEFoam solver a fixed number of eight PNP internal iterations was used for all the calculations.

## 7.2 Verification

RheoEFoam solver has already been implemented and cross-verified for the PNP model in various EDF cases, such as induced charge electro-osmosis (ICEO) around a conducting cylinder and charge transport across an ion-selective membrane [8]. In the current framework, we consider a rectangular 2D computational domain of dimensions  $\pm L \times H$ , which is typical of two configurations presented in figure 16. The first configuration operates with a symmetric binary electrolyte confined by an ideal permselective membrane from the bottom, which allows for the transport of cations and is impermeable for anions, and by the well-stirred Ohmic bulk from the top. Fixed values of electric potential are applied to the membrane and the bulk. Non-slip BCs for all the velocity components are set on the membrane surface, while the slip condition (no penetration and no viscous shear stress) is set on the bulk boundary. Assigning index  $i = 1$  to cation and  $i = 2$  to anion species, the full list of the BCs in a non-dimensional formulation is given by:

$$\begin{aligned}
 y = 0: \quad & c_1 = N, \quad J_{y2} = 0, \quad \Psi = -V - \ln N, \quad \vec{u} = \vec{0}; \\
 y = 1: \quad & c_1 = c_2 = 1, \quad \Psi = 0, \quad \frac{\partial u_x}{\partial y} = 0, \quad u_y = 0,
 \end{aligned} \tag{84}$$

where  $N$  relates to the maximum to minimum ratio of initial species concentration and  $-\ln N$  accounts for the Donnan potential-jump [74], ensuring the zero current density value when no external potential is applied.

The ICs for the concentration and the electric potential fields satisfy the quiescent state, being the steady state solution of the PNP equations (46-47) obtained by assuming no fluid flow ( $\vec{u} = \vec{0}$ ), and by applying the BCs for electric potential as defined in equation (84) with no external voltage ( $V = 0$ ). The initial value of the velocity vector is set to zero.

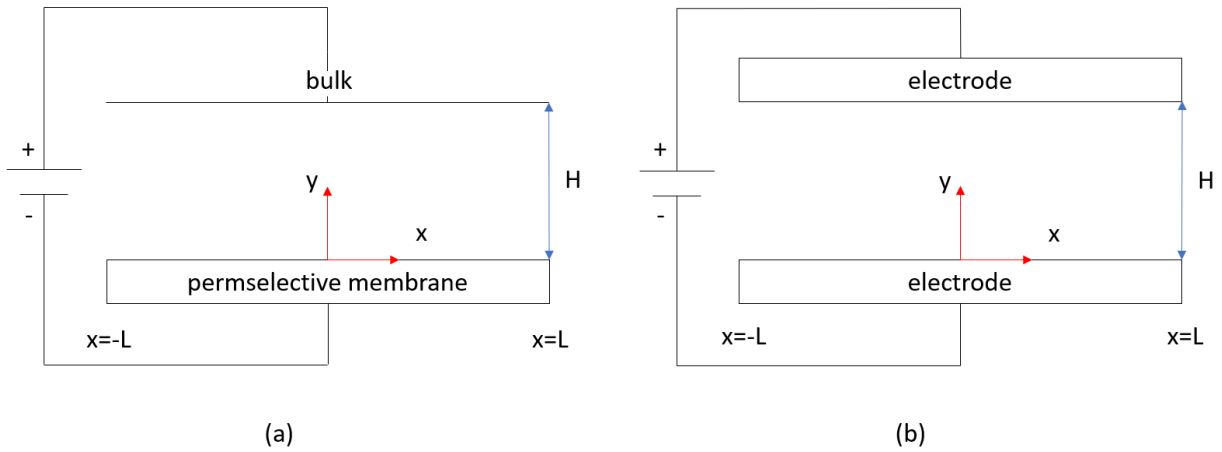


**Figure 16: Schematic of (a) permselective membrane-bulk configuration and (b) two electrodes configuration.**

The second configuration operates with a non-symmetric electrolyte consisting of three charged species of valences  $z^+$ ,  $z^-$ , and  $Mz^-$  assigned with the indices  $i = 1, 2, 3$ , respectively. This configuration is confined by two parallel open electrodes. The BCs for the concentration fields are: the bottom electrode is completely open for cations and impermeable for the two negatively charged species; the top electrode is impermeable for cations and is completely open for the two negatively charged species. The bottom and top electrodes are held at constant electric potential  $-V/2$  and  $V/2$ , respectively. Note that the Donnan effect is not taken into account for the electrode boundaries. Non-slip BCs for all the velocity components are set on the surfaces of both electrodes. The full list of the applied BCs in a non-dimensional formulation is given by:

$$\begin{aligned}
 y = 0: \quad & \frac{\partial c_1}{\partial y} = 0, \quad J_{y2} = J_{y3} = 0, \quad \Psi = -\frac{V}{2}, \quad \vec{u} = \vec{0}; \\
 y = 1: \quad & J_{y1} = 0, \quad \frac{\partial c_2}{\partial y} = \frac{\partial c_3}{\partial y} = 0, \quad \Psi = \frac{V}{2}, \quad \vec{u} = \vec{0}.
 \end{aligned} \tag{85}$$

Note that the above BCs can be straightforwardly adapted for the case of a symmetric binary electrolyte by simply omitting the relationships with index  $i = 3$ .



The ICs for the concentration fields have to provide the electroneutrality condition of the DL given by equation (67). Note that this relationship can be straightforwardly adapted to the symmetric binary electrolyte by simply assigning the values of  $z_{r,2} = -1$  and  $c_r = 0$ . Zero initial values are set for the electric potential and velocity vector fields within the computational domain.

For both configurations, periodic BCs for all the fields are set in the  $x$  direction such that

$$\Omega|_{x=-AR/2} = \Omega|_{x=AR/2} \quad \text{and} \quad \frac{\partial \Omega}{\partial x}\bigg|_{x=-AR/2} = \frac{\partial \Omega}{\partial x}\bigg|_{x=AR/2} \quad \text{where } \Omega \text{ represents any of the dependent variables.}$$

The numerical results obtained in the framework of the current study by using the rheoEFoam solver and specifically written Matlab script have been extensively verified by comparison with the data available in the literature for a number of representative configurations characterizing ionic transport within a symmetric binary electrolyte. Specifically, steady ionic transport phenomena operating in Ohmic, limiting and overlimiting regimes (see figure 8) and unsteady ionic transport phenomena operating in an overlimiting regime, both typical of a permselective membrane-bulk configuration (see figure 16(a)), were simulated and compared with the corresponding results reported in [35,51]. Note also that for the sake of completeness the results obtained for the overlimiting regime were calculated independently from these reported in [8] and obtained by utilizing the same rheoEFoam solver. Additionally, the specifically written Matlab script has been cross verified with the rheoEFoam solver simulating 1D ionic transport between the two electrodes configuration (see figure 16(b)) typical of the limiting regime. The results obtained by the two tools have been compared in terms of the concentration fields of the two species and the distribution of the corresponding potential and electric fields.

### 7.2.1 Permselective Membrane-Bulk Configuration

The 1D (no flow) and 2D ionic transport within the symmetric binary electrolyte are considered for the permselective membrane-bulk configuration shown in figure 16(a). The BCs applied are the same as in [35]:

$$\begin{aligned} y=0: \quad c_1 = N, \quad J_{y,2} = 0, \quad \Psi = 0, \quad \vec{u} = \vec{0}; \\ y=1: \quad c_1 = c_2 = 1, \quad \Psi = V, \quad \vec{u} = \vec{0}, \end{aligned} \tag{86}$$

where periodic BCs are applied in the horizontal direction for the 2D case.

Following the procedure described in [35], the ICs are assigned by locally perturbing by 1% the concentration values obtained by the solution of the 1D PNP equations. The electric current density  $I_y$  obtained by utilizing equation (49) applied to the mid-cross section ( $y = 0.5$ ) of the

electrolytic cell<sup>1</sup> for the binary ( $n = 2$ ) electrolyte is shown in figure 17 as a function of the non-dimensional voltage  $V$ . For the 1D configurations the presented results represent the steady state  $I_y - V$  dependence corresponding to Ohmic and limiting regimes (see figure 8). For the 2D configuration the steady state  $I_y$  value was only obtained for the value of  $V = 20$ . For higher voltages, quasi-steady state flows were observed, while the current density values presented in figure 17 were obtained by the averaging of the instantaneous  $I_y$  values over the time interval  $t = 0.1 \div 0.9$  (the same as in [35]). All the simulations performed for permselective membrane-bulk configuration (see figure 16(a)) were run on  $1 \times 10000$  and  $960 \times 180$  grids utilized for 1D and 2D configurations, respectively. Both grids were stretched towards the boundaries while the minimal cell width was equal to  $3.278 \times 10^{-4}$ . The 2D grid described here is denoted as G1 throughout this work.

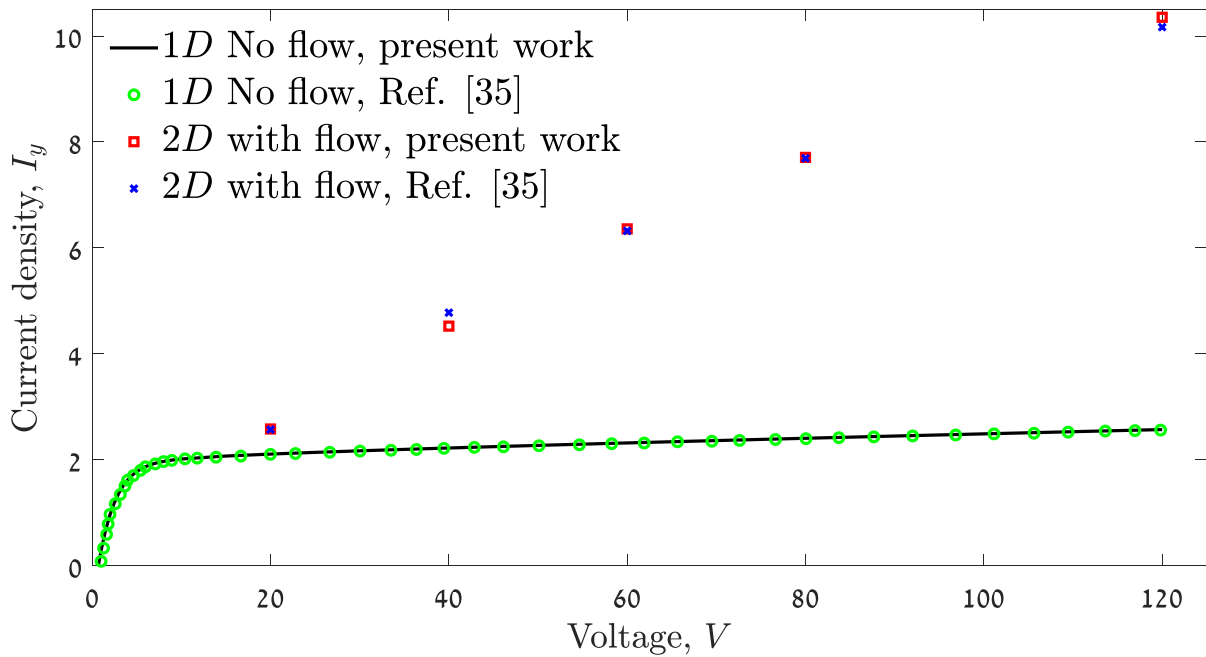


**Figure 17: Non-dimensional steady state  $I_y - V$  dependence. Comparison between the presently obtained and independent [35] results obtained for 1D and 2D configurations. The results are obtained for  $N = 2$ ,  $\epsilon = 10^{-3}$ , and  $V \in [0 \div 120]$ . For the 2D configuration the values of  $AR = 6$ ,  $Sc = 10^3$ , and  $Pe = 0.5$  were used.**

All the results were obtained for the values of  $N = 2$ ,  $\epsilon = 10^{-3}$ , and  $V \in [0 \div 120]$ . Additionally, the 2D simulations were run for the values of  $AR = 6$ ,  $Sc = 10^3$ , and  $Pe = 0.5$ . The deviation between the 1D and 2D results shown in figure 17 starts at about  $V = 20$  and is caused by the onset of an EC phenomenon characterizing the transition between limiting and overlimiting

<sup>1</sup> The mid-cross-section is considered here for the sake of simplicity, as the instantaneous current density value is the same at any cross-section of the electrolytic cell (see section 8.3).

regimes [35]. It can be seen that the currently obtained 1D results are in excellent agreement with the corresponding results obtained in [35] for the entire range of  $V$  values. Also, the currently obtained 2D results agree well with the corresponding data reported in [35], while the maximal relative deviation between the current and the independent values of  $I_y$  does not exceed 5.5%.

We next perform a verification study of transient 2D EC, including characterizing the ECI onset which is the major focus of the current chapter. A grid independence study is also performed. For this purpose, the membrane-bulk configuration operating with the symmetric binary electrolyte is considered. The full set of governing equations (50) with the BCs determined in equation (84) and the ICs corresponding to the quiescent state is solved. The non-dimensional parameters utilized are  $N = 2$ ,  $V = 25$ ,  $\epsilon = 10^{-3}$ ,  $AR = 6$ ,  $Sc = 10^3$ , and  $Pe = 0.5$ . Note that as a result of the high value of the  $Sc$  number the convective term of equation (45) was omitted. Figure 18 shows the time evolution of the current density  $I_y$  calculated by utilizing equation (49). The results were obtained on three different grids G1, G2, and G3 corresponding to 960x180, 1920x360, and 3840x720 grid resolutions, respectively. The grids were stretched towards the membrane and bulk boundaries.

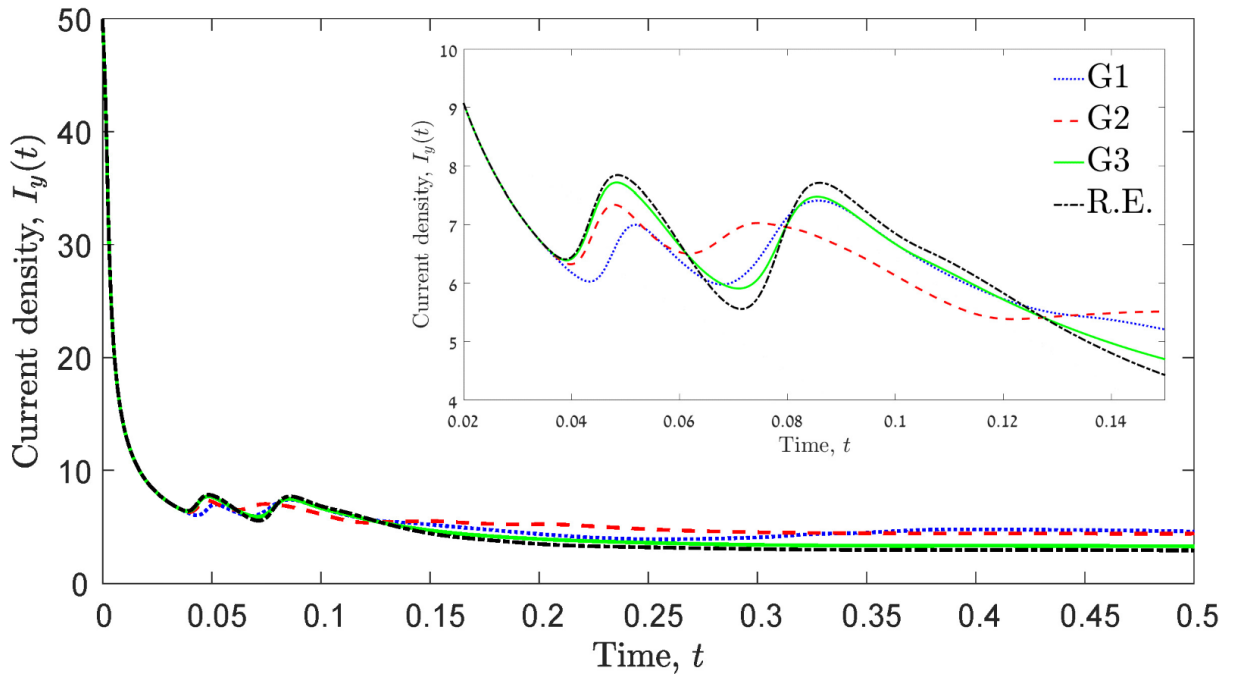


**Figure 18: Grid independence test by means of transient current density obtained by rheoTool 2D simulations of the membrane-bulk configuration. Results are obtained for  $N = 2$ ,  $V = 25$ ,  $\epsilon = 10^{-3}$ ,  $AR = 6$ ,  $Sc = 10^3$ , and  $Pe = 0.5$ . Insets: Close-up on the ECI onset represented by two consecutive abrupt peaks of the current density response including accurate values obtained by employing Richardson extrapolation based on G2 and G3 grids.**

As can be seen from figure 18, the electric current density curves descend rapidly up to two consecutive peaks followed by convergence to the steady state value. These peaks shown in the

close-up of figure 18 are associated with the ECI onset within the electrolytic cell. The convergence of the results obtained with different grid resolutions is established as follows from figure 18. A zero-grid-size approximation for the time evolution of  $I_y$  was next calculated by employing the Richardson extrapolation (R.E.) to the results obtained on G2 and G3 grids. The first minimum and maximum values of the time evolution of  $I_y$  obtained on the three grids, along with the values provided by R.E. (see the close-up of figure 18) are next compared with the independent results reported in [51] for the potentiostatic response of a nonconfined system, as summarized in table 1.

**Table 1: Non-dimensional time and current density values of the minimum and maximum points of the first abrupt peak for different grids, compared to those obtained in Ref. [51].**

	G1	G2	G3	R.E.	Ref. [51]
$t_{min}$	0.0433	0.0398	0.0391	0.0389	0.0238
$I_{min}$	6.0247	6.3203	6.3885	6.4060	8.8141
$t_{max}$	0.0518	0.0479	0.0484	0.0485	0.0450
$I_{max}$	6.9965	7.3391	7.7137	7.8408	10.4240

As can be seen from table 1, the values of the first minimum and maximum peaks of current density reported in [51] are somewhat higher (by up to 28%) and were acquired at earlier times compared to the currently obtained grid convergent results. Unfortunately, details on neither the ICs nor the discretization schemes were provided in [51], which makes it difficult to exactly pinpoint the reasons for the observed discrepancy. Nonetheless, the currently utilized standard second-order FV based on the central discretization schemes, and thus not containing numerical dissipation, and the extensive grid independence study performed corroborate the correctness and the high precision of the currently obtained results. Taking into account the fact that there are no significant differences in time evolution of  $I_y$  obtained on G2 and G3 grids, all the 2D results presented in section 7.3 were calculated on G2 grid.

### 7.2.2 Two Electrodes Configuration

We next focus on verification of the rheoEFoam solver applied to the simulation of ionic transport typical of the electrolytic cell confined by two electrodes. The electrolytic cell is filled with binary initially electrically neutral electrolyte. The specific BCs and ICs are defined in equations (85) and (67), respectively. Periodic BCs are applied in the horizontal direction. The dynamics of ionic transport are characterized by the separation of oppositely charged species within the electrolytic cell in a limiting regime (with voltage equal to  $V = 40$ ) so that the ECI does not onset. In this case, the advective component of ionic transport is negligibly small and

the ionic transport is only governed by the diffusive and the electromigration terms of the ionic flux (see equation (21)). Thus, the results obtained by the rheoEFOam solver for the 2D geometry can be compared with the corresponding 1D data obtained by the previously verified Matlab code. The comparison is presented in terms of the instantaneous spatial distribution of concentration of anions and cations (see figures 19(a) and 19(b), respectively), as well as in terms of the spatial distribution of electric potential  $\Psi$  (see figure 19(c)) and of the spatial distribution of the absolute value of the electric field  $|\vec{E}|$  (see figure 19(d)). All the simulations were performed on the 1x1000 and 960x180 grids utilized for 1D and 2D configurations, respectively. The two grids were stretched towards the electrode boundaries, while the minimal cell width was equal to  $3.278 \times 10^{-4}$ . All the presented snapshots are taken at a representative time instance equal to  $t = 0.01$ .

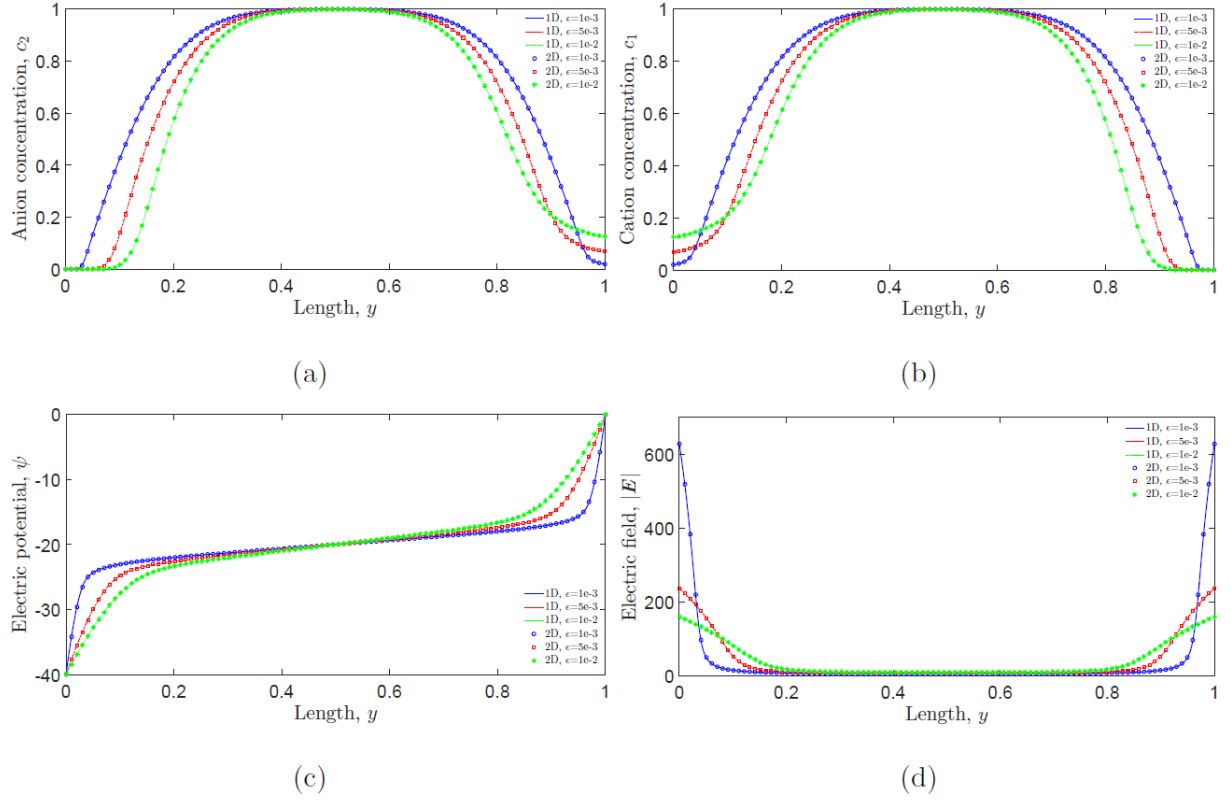


**Figure 19: Comparison between 1D results provided by the specifically written Matlab script and 2D results provided by the rheoEFOam solver for the two electrodes configuration operating in the limiting regime: (a) concentration of the anion species,  $c^-$ ; (b) concentration of the cation species,  $c^+$ ; (c) electric potential field,  $\Psi$ ; (d) magnitude of the electric field,  $|\vec{E}|$ . Results are obtained for the values  $V=40$ ,  $\epsilon \in [10^{-3} \div 10^{-2}]$ , and for the 2D case  $AR=6$ ,  $Sc=10^3$ , and  $Pe=0.45$  at  $t=0.01$ . Solid lines and circles correspond to the results provided by the Matlab script and the rheoEFOam solver, respectively.**

All the results were obtained for the voltage value of  $V = 40$  and three different values of electrostatic screening length,  $\epsilon$  lying in the range of  $\epsilon \in [10^{-3} \div 10^{-2}]$ . The 2D rheoTool

simulation was executed for the values of  $AR=6$ ,  $Sc=10^3$ , and  $Pe=0.45$ . It can be seen that all the results obtained by the two solvers are in excellent agreement for the entire range of  $\epsilon$  values. As expected for the ionic transport within a symmetric binary initially electrically neutral electrolyte, the concentration distributions of positive and negative species are reflective symmetric relative to the center of the electrolytic cell. Note also that the rate of reduction of the bulk region grows with the value of  $\epsilon$ , i.e. is inverse to the initial concentration of the two species. The screening effect of each species in space charge regions adjacent to both electrodes is clearly distinguished by looking at the spatial distributions of electric potential and the electric field magnitude. Close to the two electrodes, both fields are characterized by steep gradients that gradually reduce farther from the electrodes towards the electrically neutral bulk.

### **7.3 Electro-Osmotic Flow Characterization of a Strongly Non-Symmetric Electrolyte**

This section aims to investigate and specify the behavior of a strongly non-symmetric electrolyte composed of 3 charged species and subjected to high voltage. The major question to be addressed in the current section is the impact of an additionally introduced third species characterized by significantly higher (by an order of  $O(10^3)$ ) valence and significantly lower (also by an order of  $O(10^3)$ ) diffusivity values compared to those characterizing the two other species on the electroconvective flow regime. Specifically, the investigation is restricted to the case when the two remaining species have the valence ( $\pm$  unity) and the same diffusivity values. Several flow characteristics are examined in the course of the current study: the character and the rate of the bulk propagation, the width of ESC layer and the propagation velocity of each species, spatio-temporal distribution of the electric field, time response of the electric current density, the onset time of ECI, and the typical value of the wave number of the VP at the instability onset. The above characteristics are investigated based on the results obtained by the whole set of numerical tools verified in the previous section. The results presented below shed light on the fundamental differences between the ionic dynamics typical of an electrolytic cell operating at high voltages with a symmetric binary electrolyte and with a strongly non-symmetric electrolyte composed of 3 species. The differences are discussed by means of comparison with the simulation results obtained for a 1D electrolytic cell (no EC), as well as by means of an extensive parametric study characterizing the instability onset of electroconvective flow typical of the strongly non-symmetric electrolyte. The full set of non-dimensional parameters utilized in the current study is summarized in table 2.

**Table 2: Non-dimensional parameters utilized in the numerical simulations.**

<b>Values of general parameters used in 1D and 2D configurations</b>
Voltage, $V = 4 \times 10^4$
Valence ratio of the anions, $z_{r2} = -1$
Molecular diffusivity ratio of the anions, $D_{r2} = 1$
Electrostatic screening length, $\epsilon \in [2.5 \times 10^{-4} \div 2 \times 10^{-3}]$
<b>Values of parameters used in 2D configurations for both electrolytes</b>
Aspect ratio, $AR = 6$
Schmidt number, $Sc = 10^4$
Péclet number, $Pe = 0.1$
<b>Values of parameters used in 1D and 2D configurations for electrolyte composed of 3 species</b>
Valence index of the third species, $M = 3700$
Molecular diffusivity ratio of the third species, $D_{r3} = 2 \times 10^{-3}$
Concentration ratio, $c_r \in [2 \times 10^{-5} \div 5 \times 10^{-4}]$

### 7.3.1 Analysis of 1D Configuration

We start elucidating the differences between the ionic transport typical of symmetric binary and strongly non-symmetric electrolytes by looking at the corresponding spatial distributions of the absolute value of space charge density,  $\rho_E$ , obtained between two open electrodes. Recall that both electrolytes were initially electrically neutral and composed of an equal amount of positive and negative charges. The distribution of non-dimensional  $\rho_E$  obtained for the values of  $\epsilon = 2.5 \times 10^{-4}$  and  $c_r = 10^{-4}$  is shown in figure 20 for the representative time instance,  $t = 1.7 \times 10^{-6}$ . The  $\epsilon$  value chosen constitutes the most challenging setup for the numerical solution since the Poisson equation (46) is close to being singular over almost the whole computational domain. The specific value of the time instance was chosen as it exposes an interesting phenomenon of separation between the second and the third species, as is discussed in the following.

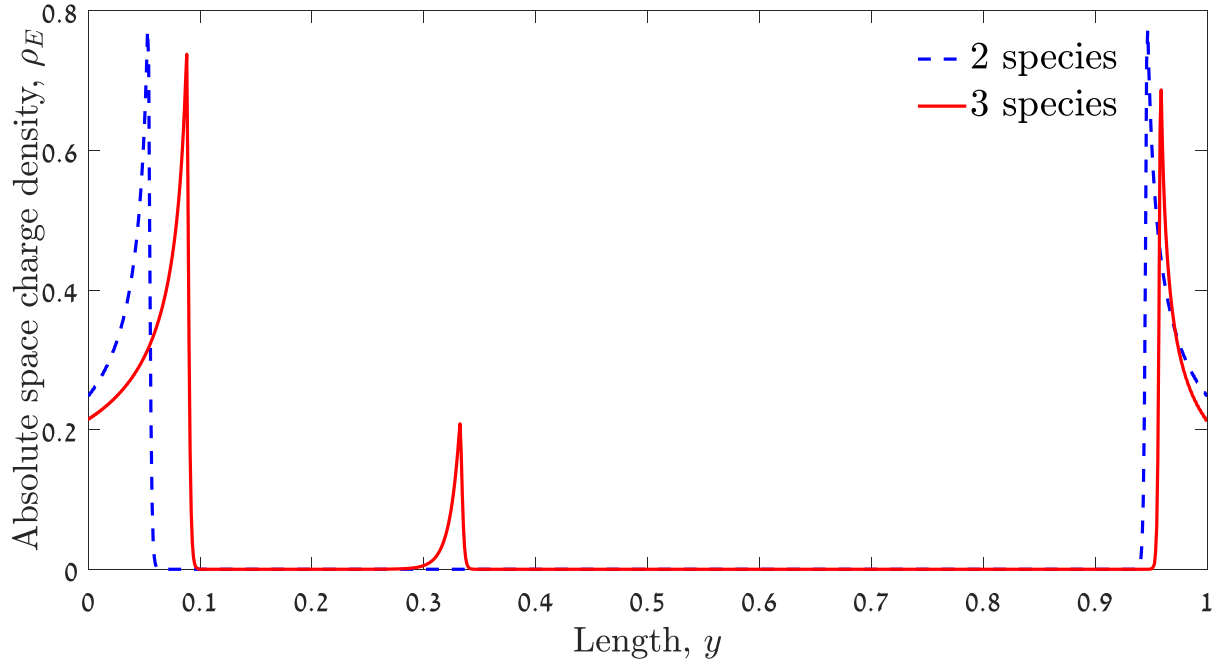


**Figure 20: Distribution of absolute value of the space charge density,  $\rho_E$ , obtained for 1D ionic transport between the two open electrodes. The results are obtained for the values of  $\epsilon=2.5 \times 10^{-4}$ ,  $t=1.7 \times 10^{-6}$ , and for 3 species  $c_r=10^{-4}$ . The results corresponding to the symmetric binary electrolyte and to the strongly non-symmetric electrolyte are denoted by the dashed and the solid lines, respectively.**

Non-zero values of the absolute space charge density indicate the width of the ESC region at a given time instance. In both cases, the ionic transport within the electrolyte between the two open electrodes is characterized by the existence of two ESC regions that start to develop close to each electrode and progress inwards with time. Following the schematic of the considered configuration (see figure 16(b)), the externally imposed electric field is directed from the right towards the left electrode; thus the left and the right spikes separate between the neutral bulk and the positively and the negatively charged ESC regions, respectively. As expected, the ESC width of the symmetric binary electrolyte preserves its symmetry over time relative to the center of the electrolytic cell. For the strongly non-symmetric electrolyte the picture is quite different and is distinguished by three unique features. First, there are actually 3 ESC regions, each determined by its spike corresponding to the specific species. Second, the separation of the two negatively charged species can be clearly distinguished by the existence of two spikes in the distribution of  $\rho_E$  in the left part of the computational domain. Third, each ESC region is characterized by a different propagation rate.

To gain more insight into the spatio-temporal charge distribution within the strongly non-symmetric electrolyte we next decompose the space charge density  $\rho_E$  into the terms



contributed by each species, namely,  $z_1 c_1$ ,  $z_2 c_2$  and  $z_3 c_3 = M z_2 c_3$ <sup>2</sup>. The spatial distribution of the absolute value of each term contributing to  $\rho_E$  taken at  $t = 1.7 \times 10^{-6}$  is presented in figure 21.

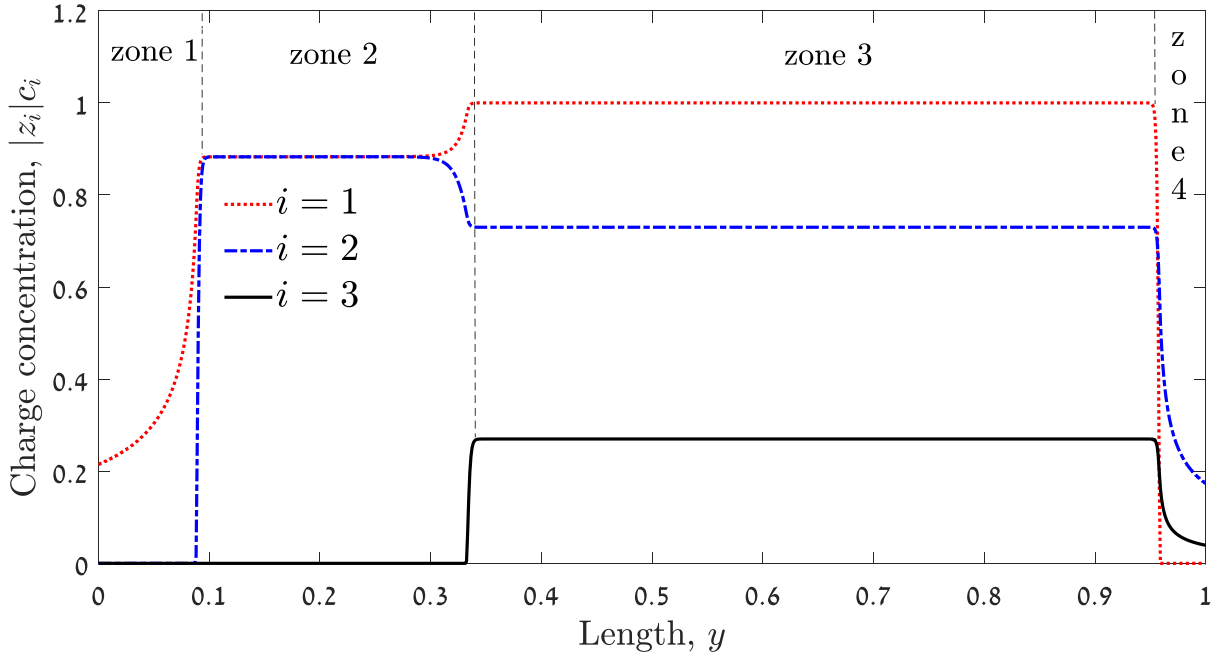


**Figure 21:** Spatial distribution of the terms  $|z_i|c_i$  ( $i = 1, 2, 3$ ) contributing to the space charge density  $\rho_E$ . The results are obtained for the values of  $\epsilon = 2.5 \times 10^{-4}$ ,  $c_r = 10^{-4}$ , and  $t = 1.7 \times 10^{-6}$ .

The spatial distribution shown in figure 21 can be semantically split into four zones. Zones 1 and 4 represent the positively and the negatively charged ESCs, respectively. Zone 3 corresponds to the electrically neutral bulk whose composition is the same as that determined by the IC (see equation (67)). Generally speaking, zone 3 is not unique for a non-symmetric electrolyte, as it can also be seen in ionic transport of a symmetric binary electrolyte. In contrast, zone 2 is an exclusive feature typical of a strongly non-symmetric electrolyte in which one of the species has much higher electrical mobility, and thus the separation phenomenon between two negatively charged species takes place. Specifically, in the current study, the  $D_r z_r$  multiplier entering the ionic flux (see equation (48)) and constituting electrical mobility of the  $i^{\text{th}}$  species is more than seven times higher for the  $i = 3$  species compared to that of the  $i = 2$  species. For this reason, both zones 1 and 2 are entirely depleted of the  $i = 3$  species as its propagation rate is much higher than that of the  $i = 2$  species. Remarkably, the  $i = 1$  and  $i = 2$  species adjust themselves

<sup>2</sup> Note that this decomposition has been already introduced in equation (67) as the IC providing electroneutrality of the non-symmetric electrolyte.

differently in zone 2 compared to zone 3 in order to preserve electroneutrality in the region entirely depleted by the  $i = 3$  species <sup>3</sup>.

Until now, we have explained two distinguishing features typical of the charge distribution of the considered strongly non-symmetric electrolyte. The third feature, i.e. non-equal propagation rate of the  $i = 1$  and  $i = 2$  species when moving away from the right and left electrodes, respectively, towards the center of the electrolytic cell can be explained by focusing on the spatial distribution of the electric field magnitude  $|\vec{E}|$  shown in figure 22. We first focus on the distribution of the electric field magnitude in the ESC region adjacent to the right electrode. Close to the electrode, there is no separation between the two negatively charged species (see figure 21); thus, both species simultaneously affect the ionic transport in this region, while the degree of impact of each species is in accordance with the concentration multiplied by the valence of the given species. As a result, this region is dominated by the negative charges which screen the imposed electric potential, as reflected by a rapid decrease of the electric field, until it reaches a minimum constant value characterizing the bulk region and eventually governing the propagation rate of the cations away from the right electrode. The mechanism driving the negatively charged species away from the left electrode is somewhat different. As has already been mentioned, there is a separation between the species (see figure 21) in this region due to the different electro-osmotic mobilities, and the negatively charged  $i = 3$  species outstrips the  $i = 2$  species on its way towards the center of the electrolytic cell. Zone 2 is thus entirely depleted of the  $i = 3$  species, which leads to a decrease in the concentration of the  $i = 1$  species (see figure 21) in order to preserve the electroneutrality of the electrolyte in this region. As a result, the screening of the imposed electric potential due to the presence of the  $i = 1$  species is lower compared to that in the ESC region adjacent to the right electrode <sup>4</sup>. This fact is reflected by the higher value of the electric field magnitude  $|\vec{E}|$  prevailing in zone 2 compared to that prevailing in zone 3 (see figure 22), and determines the higher propagation rate of the anion species ( $i = 2$ ) towards the center of the electrolytic cell compared to that of the cation species ( $i = 1$ ).

---

<sup>3</sup> The electroneutrality is preserved over the whole width of zone 2, except for the back front of the  $i = 3$  species, consistently with the spike of  $\rho_E$  observed at  $y \approx 0.33$  as appears in figure 20.

<sup>4</sup> Recall that in the ESC region adjacent to the right electrode the screening effect of the imposed electric potential is due to the presence of the two negatively charged species  $i = 2$  and  $i = 3$ .

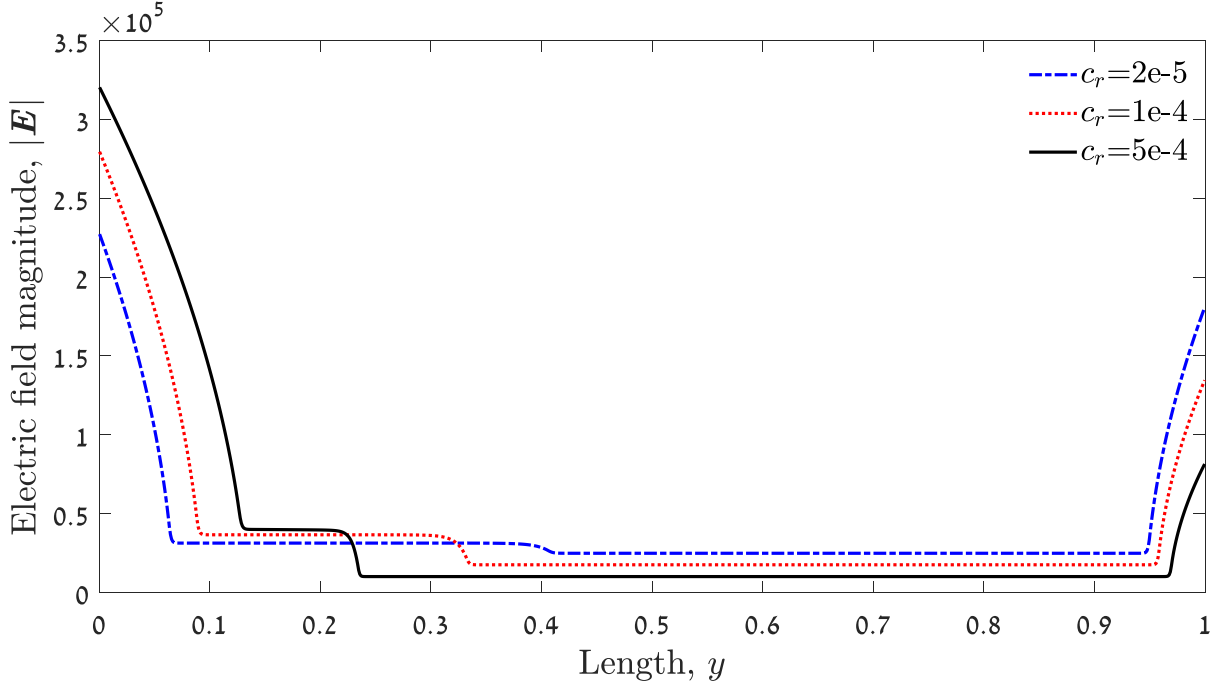


**Figure 22:** Spatial distribution of the electric field magnitude,  $|\vec{E}|$ , for different  $c_r$  values. The results are obtained for the value of  $\epsilon = 2.5 \times 10^{-4}$  and  $t = 1.7 \times 10^{-6}$ .

The last interesting observation regards the impact of the concentration ratio of two negatively charged species,  $c_r = c_3/c_2$  on the propagation rate of all the species, which is closely correlated with the spatio-temporal distribution of  $|\vec{E}|$ . As can be seen from figure 22, increasing the  $c_r$  value has a quite minor impact on the propagation rate of the cations. The higher the  $c_r$  value, the more negative charge is accumulated in the ESC region adjacent to the right electrode (zone 4) and the weaker is  $|\vec{E}|$  due to the screening effect. As a result, the propagation rate of cations decreases slightly with the increasing  $c_r$  value. In contrast, increasing the  $c_r$  value significantly affects the propagation rate of the two negatively charged species away from the left electrode. In particular, the higher the  $c_r$  value, the higher is the propagation rate of the  $i = 2$  species and the lower is the propagation rate of the  $i = 3$  species. As has been explained above, the propagation rate of the  $i = 3$  species is entirely determined by the magnitude of  $|\vec{E}|$  in zone 3. Thus, the higher is the value of  $|\vec{E}|$  in zone 3, or, in other words, the lower the  $c_r$  value, the higher is the propagation rate of the  $i = 3$  species. Following the same idea, the propagation rate of the  $i = 2$  species is entirely determined by the magnitude of  $|\vec{E}|$  in zone 2. Decreasing the  $c_r$  value results in increasing the concentration value of the  $i = 1$  species (cations) in zone 2 to

provide electroneutrality of the electrolyte in this region. Further, the screening of the imposed electric potential by the  $i = 1$  species in zone 1 becomes pronounced, which, in turn, leads to the stronger drop in the  $|\vec{E}|$  value typical of zone 2, and consequently results in the lower propagation rate of the  $i = 2$  species.

### 7.3.2 Analysis of 2D Configuration

The analysis performed in the previous section provided important insights regarding the fundamental differences between the ionic transport within a symmetric binary and a strongly non-symmetric electrolyte consisting of 3 species under high voltage. However, to investigate the differences in mechanism typical of the onset of the ECI within the electrolytic cell, an analysis of 2D electroconvective flow should be performed.

#### 7.3.2.1 Analysis of Current Density

Figure 23 presents the time evolution of the current density  $I_y$  obtained by the numerical simulation of 1D and 2D ionic transport for symmetric binary (2 species) and strongly non-symmetric (3 species) electrolytes confined by two parallel electrodes. The simulations were performed for the value of  $c_r = 2 \times 10^{-5}$  and four different values of  $\epsilon$  in the range of  $\epsilon \in [2.5 \times 10^{-4} \div 2 \times 10^{-3}]$ . The obtained results indicate several general trends. First, the initial value of the current density  $I_y$  obtained for the 3 species electrolyte is higher by about 22% than that of the binary electrolyte for the entire range of  $\epsilon$  values. It is remarkable that the trend caused by the very rapid transport of the  $i = 3$  species compared to the cation and the anion species is invariant to the  $\epsilon$  value and can be accurately predicted by simply using equation (49) applied to the mid-cross-section ( $y = 0.5$ ) of the electrolytic cell. The applied ICs provide a uniform initial concentration and zero velocity values, leading to negligible velocities and concentration gradients in the mid-cross-section of the electrolytic cell at the very beginning of numerical simulations. As a result, the contribution of the advective and diffusive terms of the ionic flux (see equation (48)) is neglected for the two electrolytes. Next, also neglecting, for the sake of simplicity, the displacement current density term in equation (49), and assuming the same value of the electric field characterizing the two configurations at the very beginning of the ionic transport, the ratio  $R_r$ , between the electric current densities characterizing a strongly non-symmetric electrolyte consisting of 3 species and its symmetric binary counterpart, is estimated by:

$$R_I \approx \frac{(c_1 + c_2 + D_{r3} z_{r3}^2 c_3)_{3 \text{ species}}}{(c_1 + c_2)_{2 \text{ species}}}. \quad (87)$$

All the results presented in figure 23 were obtained for the non-dimensional values of  $c_1 = c_2 = 1$  or  $c_1 = 1$ ,  $c_2 = 0.9311$ , and  $c_3 = 1.8622 \times 10^{-5}$  related to the electrolyte composed of 2 or 3 species, respectively, which can be deduced from the IC providing the electroneutrality constraint for the two electrolytes (see equation (67)). The value of  $R_I = 1.26$  can be analytically approximated by equation (87). Overestimation of about 4% of the approximated  $R_I$  value can be attributed to the contribution of the displacement current density term (see equation (49)), which was neglected when estimating the  $R_I$  value in equation (87).

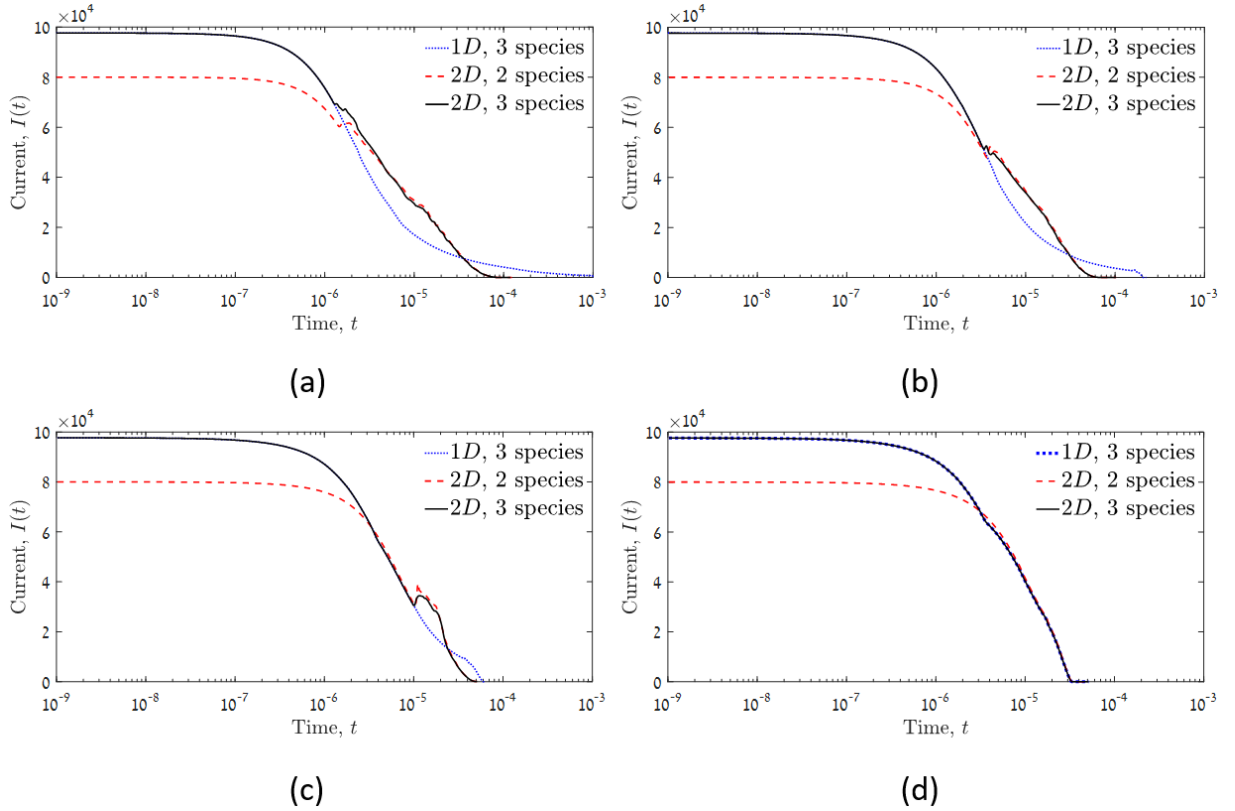


**Figure 23: Time evolution of the current density obtained by the numerical simulations of ionic transport within 2 or 3 species electrolytes for 1D and 2D configurations. The results are obtained for the value of  $c_r = 2 \times 10^{-5}$  and for the values of: (a)  $\epsilon = 2.5 \times 10^{-4}$ ; (b)  $\epsilon = 5 \times 10^{-4}$ ; (c)  $\epsilon = 10^{-3}$ ; (d)  $\epsilon = 2 \times 10^{-3}$ .**

Another trend clearly distinguished by looking at figure 23 is related to the equal transient values of the current density  $I_y$  obtained for both 1D and 2D configurations up to the ECI onset, as recognized by the local abrupt increase of the  $I_y$  values characterizing the 2D configuration. This result is consistent with the data presented in figure 19 and shows that there is no difference

between the ionic transport obtained for 1D and 2D configurations in the limiting flow regime. As mentioned in section 7.2, the abrupt increase of the  $I_y$  values indicates the transition between limiting and overlimiting regimes [57], which typically indicates the ECI onset. The physical mechanism responsible for the abrupt increase of  $I_y$  is attributed to the enhanced ionic transport caused by the convective mixing of the charged species. Remarkably, higher  $\epsilon$  values (or, in other words, lower values of the initial concentration of the charged species) result in a delay of the ECI onset. In particular, for the maximal value of  $\epsilon = 2 \times 10^{-3}$  the electrolytic cell became fully discharged before the ECI onset.

We next investigate the time evolution of the current density for the non-symmetric electrolyte consisting of 3 species, characterized by the fixed value of  $\epsilon = 5 \times 10^{-4}$  and three different values of  $c_r = 2 \times 10^{-5}, 10^{-4}$  and  $5 \times 10^{-4}$ . The results are shown in figure 24. It can be seen that higher values of  $I_y$  correlate with the higher values of  $c_r$  at times up to  $t \leq 10^{-6}$ . This finding is not surprising as at the very beginning of the ionic transport  $I_y$  is primarily governed by the charge carried by the  $i=3$  species, whose electrical mobility is much higher compared to that characterizing the other two species. Consequently, the higher the concentration of the  $i=3$  species<sup>5</sup> (i.e. the higher the  $c_r$  value), the higher is the corresponding initial current density value. In particular, the initial value of the current density  $I_y$  obtained for the value of  $c_r = 5 \times 10^{-4}$  is higher by about 152% and by about 65% than the corresponding values obtained for  $c_r = 2 \times 10^{-5}$  and  $c_r = 10^{-4}$ , respectively. Additionally, the initial value of the current density  $I_y$  obtained for the value of  $c_r = 10^{-4}$  is higher by about 53% than the corresponding value obtained for  $c_r = 2 \times 10^{-5}$ . It was further verified that these ratios are invariant to the  $\epsilon$  value and can be accurately estimated by simply using equation (49) applied to the mid-cross-section ( $y = 0.5$ ) of the electrolytic cell. Following the same assumptions as those applied when deriving equation (87), we next derive the expressions for  $R_{II}$ ,  $R_{III}$ , and  $R_{IV}$  corresponding to the ratios between the electric current densities obtained for the values of  $c_r = 5 \times 10^{-4}$  and  $c_r = 2 \times 10^{-5}$ ,  $c_r = 5 \times 10^{-4}$  and  $c_r = 10^{-4}$ , and  $c_r = 10^{-4}$  and  $c_r = 2 \times 10^{-5}$ , respectively:

---

<sup>5</sup> Increasing the initial concentration of the  $i=3$  species leads to a simultaneous decrease in the initial concentration of the  $i=2$  species in order to preserve the constant value of the negative charge within the electrolyte.

$$\begin{aligned}
R_{II} &\approx \frac{\left(c_1 + c_2 + D_{r3} z_{r3}^2 c_3\right)_{c_r=5 \times 10^{-4}}}{\left(c_1 + c_2 + D_{r3} z_{r3}^2 c_3\right)_{c_r=2 \times 10^{-5}}}; \\
R_{III} &\approx \frac{\left(c_1 + c_2 + D_{r3} z_{r3}^2 c_3\right)_{c_r=5 \times 10^{-4}}}{\left(c_1 + c_2 + D_{r3} z_{r3}^2 c_3\right)_{c_r=10^{-4}}}; \\
R_{IV} &\approx \frac{\left(c_1 + c_2 + D_{r3} z_{r3}^2 c_3\right)_{c_r=10^{-4}}}{\left(c_1 + c_2 + D_{r3} z_{r3}^2 c_3\right)_{c_r=2 \times 10^{-5}}}.
\end{aligned} \tag{88}$$

All the results presented in figure 24 were obtained by applying the initial concentration values detailed in table 3. The values can be straightforwardly deduced from equation (67), which determines the IC meeting the electroneutrality constraint for the two electrolytes. Substituting the concentration values from table 3 into equation (88) yields an analytical approximation for the values of  $R_{II} = 2.52$ ,  $R_{III} = 1.65$ , and  $R_{IV} = 1.53$ . It is remarkable that the numerically obtained ratio values (see figure 24) coincide with the corresponding values estimated by equation (88), which confirms that the contribution of the displacement current density term (see equation (49)) is negligible at the very beginning of the ionic transport process.

**Table 3: Non-dimensional initial concentration values utilized for different  $c_r$  values characterizing the strongly non-symmetric electrolyte.**

$c / c_r$	$2 \times 10^{-5}$	$10^{-4}$	$5 \times 10^{-4}$
$c_1$	1	1	1
$c_2$	0.9311	0.7299	0.3509
$c_3$	$1.8622 \times 10^{-5}$	$7.2993 \times 10^{-5}$	$1.7544 \times 10^{-4}$

Another important observation that can be made by looking at figure 24 regards the effect of the  $c_r$  value on the ECI onset in the strongly non-symmetric electrolyte. The onset can be recognized by an abrupt increase in the current density. As follows from looking at the close-up of the ECI onset region, the instability starts earlier for higher  $c_r$  values. This observation, along with the fact that the higher values of  $c_r$  result in a wider positively charged ESC close to the bottom electrode (see figure 22), gives rise to the expectation of a non-symmetric development of the ECI relative to the two electrodes, which is discussed in the next section of this chapter.

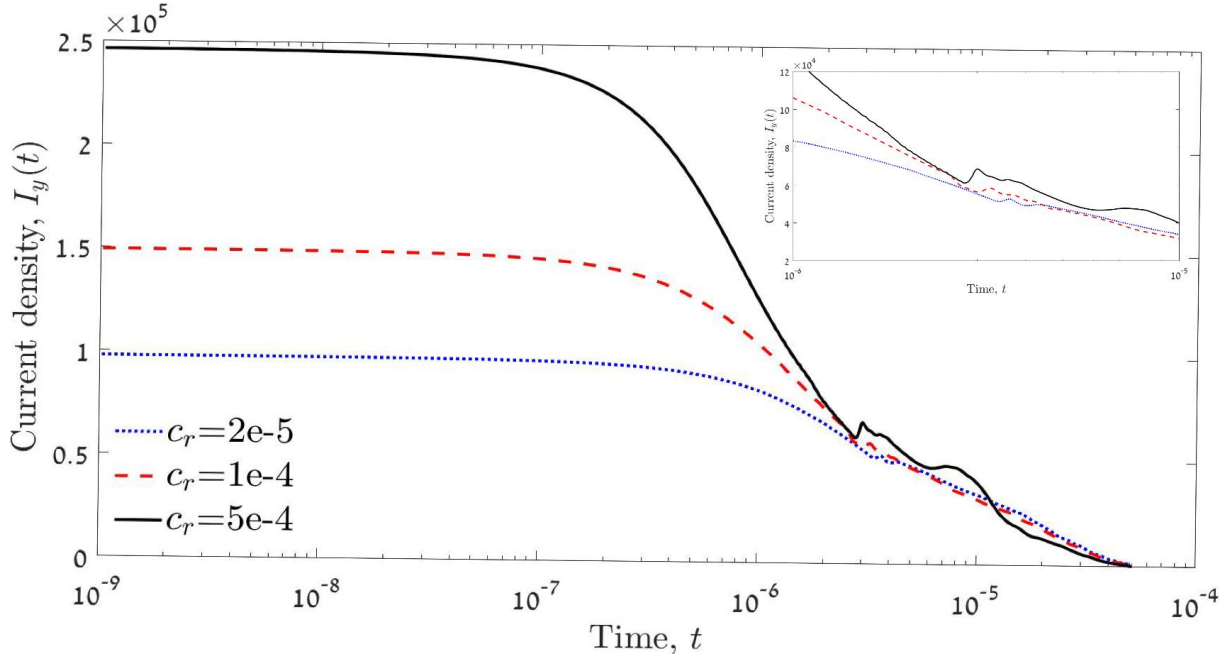


**Figure 24:** Time evolution of the current density obtained by the numerical simulations of ionic transport within a 3 species electrolyte for 2D configuration. The results are obtained for the value of  $\epsilon = 5 \times 10^{-4}$  and three different values of  $c_r$ . Close-up is of the ECI onset.

### 7.3.2.2 Analysis of Concentration Fields

As mentioned in the previous sections, symmetry breaking of ionic transport within the strongly non-symmetric electrolyte is the fundamental feature distinguishing it from that typical of a symmetric binary initially electroneutral electrolyte. The symmetry breaking takes place due to the large differences in valences and electrical mobilities of the negatively charged species  $i = 3$  compared to these characterizing the cation ( $i = 1$ ) and the anion ( $i = 2$ ) species. The latter gives rise to the development of non-symmetric ECI within the electrolytic cell, which is thoroughly investigated in the current section in terms of the spatio-temporal distributions of the cation and the anion concentration fields, taken at the ECI onset attributed to each species. Following the observations made in the previous section, there is a strong resemblance between the ionic transport within 1D and 2D electrolytic cells prior to and at the very beginning of the ECI onset. Thus, the discussion on features characterizing the ECI onset within 2D electrolytic cell is supported by the corresponding 1D results facilitating the fundamental understanding of the observed phenomena. We next introduce two additional metrics quantifying the characteristics of the ECI onset in the 2D electrolytic cell. The first is the non-dimensional wave number  $k$  defined as the instantaneous number of VP located along the length  $2L$  in the  $x$  direction (see figure 16(b)):

$$k = \frac{2\pi N_{VP}}{AR}. \quad (89)$$



Consistently with the works of [51,81-82], the wave number  $k$  was obtained based on 2D contours of the cation and anion concentrations. The  $k_1$  and  $k_2$  wave numbers were next related to the cation and the anion species, respectively. The  $k_1$  and  $k_2$  values were calculated in the vicinity of the bottom and the top electrodes, respectively. The second metric is based on two times,  $t_1$  and  $t_2$ , corresponding to appearance of VP close to the ECI onset in the vicinity of the bottom and the top electrodes, respectively. We next introduce the relative time difference  $\tau$  between  $t_2$  and  $t_1$  as:

$$\tau = \frac{t_2 - t_1}{t_2} \times 100\%. \quad (90)$$

The results of extended parametric study performed for the set of  $\epsilon$  and  $c_r$  values lying in the range of  $\epsilon \in [2.5 \times 10^{-4} \div 10^{-3}]$  and  $c_r \in [2 \times 10^{-5} \div 5 \times 10^{-4}]$  are presented in figure 25. The results are presented in terms of concentration distributions of the cation and the anion species acquired for 2D electrolytic cell together with concentration distributions of all the three species acquired for the corresponding 1D electrolytic cell at the same time instances. The time instances chosen correlate with the ECI onset recognized for each species by the vortical structures just conceived in the ESC layer adjacent to the corresponding electrode. In the following, we focus on the major characteristics of the ECI onset typical of a 2D electrolytic cell operating with a strongly non-symmetric electrolyte distinguishing it from its symmetric binary counterpart.

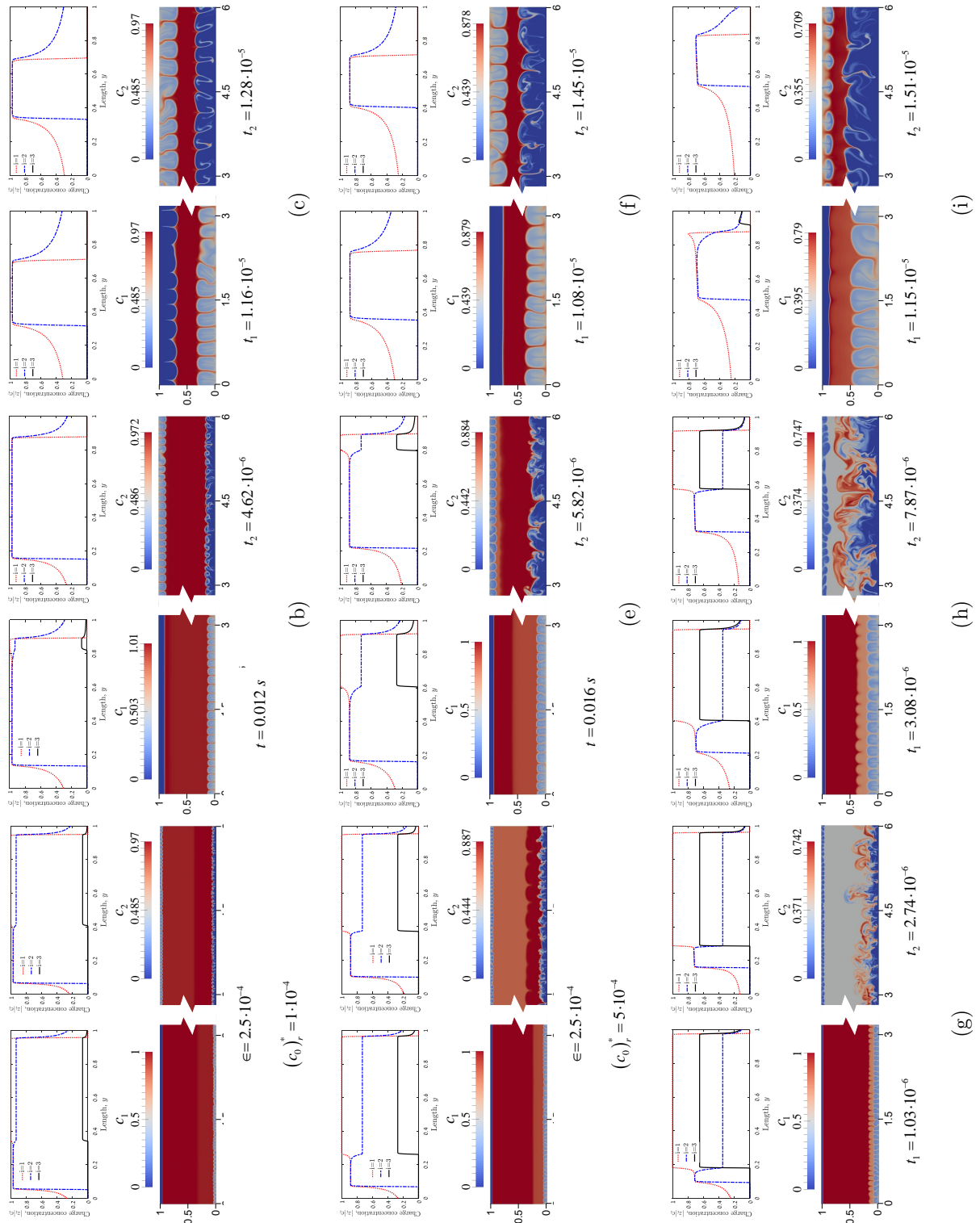


**Figure 25: ECI patterns of cation and anion species a short time after its generation, including 1D charge concentration curve of each species. (a)  $\epsilon = 2.5 \times 10^{-4}$ ,  $c_r = 2 \times 10^{-5}$ ; (b)  $\epsilon = 5 \times 10^{-4}$ ,  $c_r = 2 \times 10^{-5}$ ; (c)  $\epsilon = 10^{-3}$ ,  $c_r = 2 \times 10^{-5}$ ; (d)  $\epsilon = 2.5 \times 10^{-4}$ ,  $c_r = 10^{-4}$ ; (e)  $\epsilon = 5 \times 10^{-4}$ ,  $c_r = 10^{-4}$ ; (f)  $\epsilon = 10^{-3}$ ,  $c_r = 10^{-4}$ ; (g)  $\epsilon = 2.5 \times 10^{-4}$ ,  $c_r = 5 \times 10^{-4}$ ; (h)  $\epsilon = 5 \times 10^{-4}$ ,  $c_r = 5 \times 10^{-4}$ ; (i)  $\epsilon = 10^{-3}$ ,  $c_r = 5 \times 10^{-4}$ .**

- **Non-symmetric vortical initial state**

Following the known mechanism described in [36,58], the electro-osmotic flow of the second kind onsets within the electrolytic cell operating at the overlimiting regime with an external vertically applied electric field and drives the ECI phenomenon. The instability is initiated as a result of disturbances in the electric field introduced in the tangential direction <sup>6</sup>. In real experiments, the disturbance is typically attributed to imperfections intrinsic to the experimental setup, while in numerical simulations the instability is excited by the rounding and the truncation errors as a result of limited machine precision and discretization errors, respectively. The ECI manifests in creating a series of VP occupying the whole ESC <sup>7</sup> and accelerating the contraction of the DL region. Note that when working with finite (no matter how small) values of the Debye length (see equation (61)), the VP do not show up immediately after applying external voltage; rather, they can be clearly recognized only after the ESC reaches its critical width or, alternatively, after a certain critical time value. Although the explicit determination of the critical width and time values is the subject for a separate investigation and is not within the scope of the current study, we note in passing that these values apparently depend on the Debye length and the external voltage.

In contrast to the electrolytic cell operating with a symmetric binary electrolyte, the ECI does not onset simultaneously on DL-ESC interfaces adjacent to the two electrodes. In fact, the time  $t_2$  is higher than the time  $t_1$  for the entire range of parameters (see figure 25). Recalling that the focus is not on direct determination of the critical time values at which the ECI sets on, the delay between the emergence of VP occupying the ESC layers adjacent to the electrodes for the entire range of  $\epsilon$  and  $c_r$  values is next analyzed in terms of relative time difference  $\tau$  (see equation (90)) as summarized in table 4.

**Table 4: Values of relative time difference  $\tau$  (in percent) between the times characterizing the ECI onset at the cathode and anode.**

$c_r/\epsilon$	$2.5 \times 10^{-4}$	$5 \times 10^{-4}$	$10^{-3}$
$2 \times 10^{-5}$	19.88	18.61	9.37
$10^{-4}$	41.46	41.24	25.52
$5 \times 10^{-4}$	62.41	60.86	23.84

The physical explanation for the observed differences in  $t_1$  and  $t_2$  values is given by looking at the corresponding concentration distributions reflecting the ionic transport within the 1D electrolytic cell. It is evident that for all the simulations performed the width of the ESC layer

<sup>6</sup> i.e. in the direction perpendicular to the externally applied electric field

<sup>7</sup> In contrast to the membrane-bulk configuration, in the current electrolytic cell confined by two electrodes the VP are conceived on the DL-ESC interface.

adjacent to the cathode is higher than that adjacent to the anode, which is a consequence of much higher electrical mobility of the  $i = 3$  species and preserving electro-neutrality of the DL. As a result, the ESC layer adjacent to the cathode reaches the critical width before this happens for its counterpart adjacent to the anode, which promotes earlier conception of the ECI VP close to the cathode ESC.

A next important observation is related to the dependence of  $\tau$  on  $c_r$  and  $\epsilon$  values, as can be deduced from the data summarized in table 4. It can be seen that  $\tau$  is almost constant when the non-dimensional Debye length  $\epsilon$  increases from  $\epsilon = 2.5 \times 10^{-4}$  to  $\epsilon = 5 \times 10^{-4}$ , and rapidly increases for  $\epsilon$ , growing from  $\epsilon = 5 \times 10^{-4}$  to  $\epsilon = 10^{-3}$  - the trend which is preserved for all the  $c_r$  values. From the physical point of view this means that when the initial concentration of the charged species is low it takes a longer time for ECI to onset; thus, when the instability eventually onsets, the  $i = 3$  species possessing the higher electrical mobility has already left the electrolytic cell. As a result, the ECI evolves by a scenario resembling that of the symmetric binary electrolyte and the delay between the two times characterizing emergence of VP in the vicinity of the two electrodes decreases significantly. The same physical reason is also responsible for increasing  $\tau$  with  $c_r$  values while keeping the same values of  $\epsilon$  - the tendency which is preserved for all the data summarized in table 4 except for the two last values in column 3 of the table. In fact, the higher  $c_r$ , the faster is the contraction of DL from the cathode side compared to that from the anode side and, consequently, the difference in times at which the ECI onsets in regions adjacent to each electrode grows. The exception from this trend is observed for the last two configurations corresponding to the maximal  $\epsilon$  values (see figures 25(f) and 25(i)), and can be apparently attributed to the initially low absolute concentration value of the  $i = 3$  species and, as a consequence, its limited impact on the mechanism of the ECI onset.

- **Non-symmetric value of wave number of the VP**

As has been already mentioned, when operating in the overlimiting regime the electro-osmotic flow of the second kind is characterized by the generation of a series of VP in the vicinity of each electrode as a result of tangential disturbance of the electric field within the electrolyte. In contrast to the membrane-bulk configuration (see figure 16(a)), where the VP occupy the whole computational domain, the VP in the system of two parallel open electrodes (see figure 16(b)) occupy only the ESC regions, confined by the corresponding electrode and the ESC-DL interface. As such, the ESC width corresponding to the VP onset (in the vicinity of either the cathode or the anode), designated also as the critical width, has a major impact on the wave number value. The higher values of the ESC critical width result in larger VP hosted along the same  $2L$  length in the horizontal  $x$  direction, which, in turn, leads to their lower amount  $N_{VP}$

and to the lower value of the VP wave number. The differences between the wave numbers  $k_1$  and  $k_2$  observed for the cation concentration in the vicinity of the cathode at time  $t_1$  and for the anion concentration in the vicinity of the anode at time  $t_2$ , respectively, can be recognized by looking at the 2D subplots of figure 25, and constitute a key feature indicating the symmetry breaking of ionic transport within the non-symmetric electrolyte. The differences, as summarized in table 5, are next analyzed for the entire range of  $\epsilon$  and  $c_r$  values.

**Table 5: Non-dimensional wave numbers  $k_1$  and  $k_2$  in the vicinity of the cathode and anode, respectively.**

$c_r/\epsilon$		$2.5 \times 10^{-4}$		$5 \times 10^{-4}$		$10^{-3}$	
$2 \times 10^{-5}$	$k_1$	102	Figure 25(a)	46	Figure 25(b)	22	Figure 25(c)
	$k_2$	98		47		19	
$10^{-4}$	$k_1$	88	Figure 25(d)	39	Figure 25(e)	19	Figure 25(f)
	$k_2$	95		40		20	
$5 \times 10^{-4}$	$k_1$	71	Figure 25(g)	30	Figure 25(h)	15	Figure 25(i)
	$k_2$	83		39		16	

First, it is evident that the higher the  $\epsilon$  value, the lower are both  $k_1$  and  $k_2$  values for the entire range of  $c_r$ . Additionally, it can be seen from figure 25 that higher  $\epsilon$  values delay both the  $t_1$  and  $t_2$  times of the ECI onset. Both observations indicate that the critical ESC width associated with higher  $\epsilon$  values gets higher values as well. As a consequence, the higher critical width of the ESC results in a lower wave number. Another observation related to figure 25 is the dependency of the wave numbers,  $k_1$  and  $k_2$ , on the concentration ratio value  $c_r$ . As can be seen from table 5, for  $c_r \geq 10^{-4}$ ,  $k_2$  is higher than  $k_1$  for the entire range of  $\epsilon$ . Additionally, the higher  $c_r$  value results in a larger relative difference between the  $k_1$  and  $k_2$  values. This observation can be explained by looking at the critical width of the ESC adjacent to each electrode. As can be seen from figure 22, as well as from the 1D charts shown in figure 25, a higher  $c_r$  value results in a wider positively charged ESC close to the bottom cathode, and a thinner negatively charged ESC close to the top anode. Thus, the wave number  $k_2$  obtained for the top anode is higher than its corresponding counterpart  $k_1$  obtained for the bottom cathode. The difference between the ESC critical widths in the vicinity of the bottom and top electrodes increases with the  $c_r$  value and affects the difference between  $k_1$  and  $k_2$  values. Note that for the value of  $c_r = 2 \times 10^{-5}$ , corresponding to the lowest concentration of the  $i = 3$  species, the difference between the ESC

critical widths adjacent to each electrode is less pronounced compared to two other values of  $c_r$ . As a result, the differences between  $k_1$  and  $k_2$  values corresponding to the lowest value of  $c_r$  are relatively small and can be within the range of the computational uncertainty of equation (89).

- **Double VP series adjacent to the cathode region**

We recall that for the case of a strongly non-symmetric electrolyte, there are 3 ESC regions, each determined by its spike of absolute space charge density corresponding to the specific species, as has been demonstrated in figure 20. As can be seen from figure 21, the larger electrical mobility of the  $i = 3$  species compared to that of the other two species results in semantically splitting the electrolytic cell close to the bottom electrode into 2 different zones, denoted as zone 1 and zone 2 throughout this work. Zone 1 represents the positively charged ESC filled by only the  $i = 1$  species, while zone 2 is an exclusive feature typical of a strongly non-symmetric electrolyte and located between zones 1 and the DL (zone 3). Zone 1 together with zone 2 virtually compose the ESC corresponding to the  $i = 3$  species. We next focus on a feature associated with a 2D secondary VP series observed in zone 2 by means of  $c_1$  and  $c_2$  patterns, as shown in figure 25.

As can be seen from subfigures 25(b),(c),(f),(i), the  $i = 3$  species has already left (or is very close to leaving) the electrolytic cell. As such, the electrolyte can be considered to be a symmetric binary one, for which zone 2 simply does not exist. For this reason, we next focus only on such subplots of figure 25 where the  $i = 3$  species is still present in the electrolytic cell at both ECI onset times  $t_1$  and  $t_2$ . The left and right sides of figure 25(a) represent the concentration of the  $i = 1$  species at the time instance  $t_1$  and the concentration of the  $i = 2$  species at the time instance  $t_2$ , respectively, right after the VP were conceived in the vicinity of the cathode (for  $i = 1$ ) and the anode (for  $i = 2$ ). The different shades of red color in the bottom part of the 2D concentration field patterns represent the interface between zone 2 and the DL (zone 3). The shape of this interface is uniform on both sides of figure 25(a), meaning that the back front of the  $i = 3$  species propagates in the same way as in the 1D configuration, at both  $t_1$  and  $t_2$  time instances. Similarly, this interface is also uniform on the left side of figures 25(d),(e), corresponding to the higher  $c_r$  value than that described in figure 25(a). However, the zone 2-DL interface presented on the right side of figures 25(d),(e) is non-uniform, indicating the development of the ECI. Further increasing of the  $c_r$  value results in the appearance of a secondary VP series located in zone 2, already at the  $t_1$  time instance (left side of figures 25(g),(h)) close to the primary VP series located in zone 1 next to the cathode. The wave number of the secondary VP series resembles the wave number

of the primary VP series located in zone 1, for both figures 25(g),(h). At the more advanced time instance  $t_2$  (right side of figures 25(g),(h)), the chaotic development of the bottom VP series and the generation of multi-layer vortex structures ejected into the DL are observed, resembling the scenario observed for the overlimiting voltage in [35].

We next propose a physical interpretation of the observed phenomena. As has been already mentioned, the ECI is conceived on the ESC-DL interface. The secondary ECI, also caused by an electric field disturbance in the direction tangential to the externally applied electric field, develops in two consecutive stages: the first one leads to the non-uniformity of the zone 2-DL interface, while the second one leads to the development of VP series within zone 2, which at the overlimiting regime can be further expressed by the chaotic vortical transport of charged species. As follows from the 2D subplots of figure 25, in which the secondary ECI can clearly be recognized, it can be seen that the higher the  $c_r$  value, the earlier and faster is the development process of secondary ECI in the zone 2-DL interface. To facilitate an understanding of the physical origin of the above observation we relate to the corresponding 1D subplots of figure 25. It can be seen that a higher  $c_r$  value results in a more significant difference between the concentration values of the  $i=1$  and  $i=2$  species in the DL and in the thin area of zone 2 adjacent to it. To support this statement, we next present the distribution of the non-dimensional absolute space charge density  $\rho_E$  along the electrolytic cell for the values of  $\epsilon=2.5\times 10^{-4}$ ,  $t=1.7\times 10^{-6}$ , and three different values of  $c_r$  (see figure 26). The concentration difference between the  $i=1$  and  $i=2$  species can be easily recognized by the local abrupt increase of the absolute space charge density  $\rho_E$  as appears in the  $0.2 < y < 0.4$  region. It is clear that a higher  $c_r$  value results in a higher peak value of  $\rho_E$  corresponding to the back front of the  $i=3$  species. The higher the maximal value of the abrupt increase in  $\rho_E$  adjacent to the back front of the  $i=3$  species, the faster is the development of an electric field disturbance into the non-uniform zone 2-DL interface and a secondary ECI. Hence, looking back at figure 25(a) corresponding to the lowest value of  $c_r$ , it can be seen that the secondary ECI has not developed yet<sup>8</sup>. Looking next at figures 25(d),(e) corresponding to a higher value of  $c_r$  it can be seen that the secondary ECI starts to develop only after the appearance of a VP series along zone 1, while for the highest  $c_r$  value the secondary ECI develops simultaneously with the VP series in zone 1, yielding the chaotic vortical transport at  $t_2$  (see figures 25(g),(h)).

---

<sup>8</sup> The non-uniformity of the zone 2-DL interface starts to develop at  $t = 3.4\times 10^{-6}$  (not shown in figure 25).

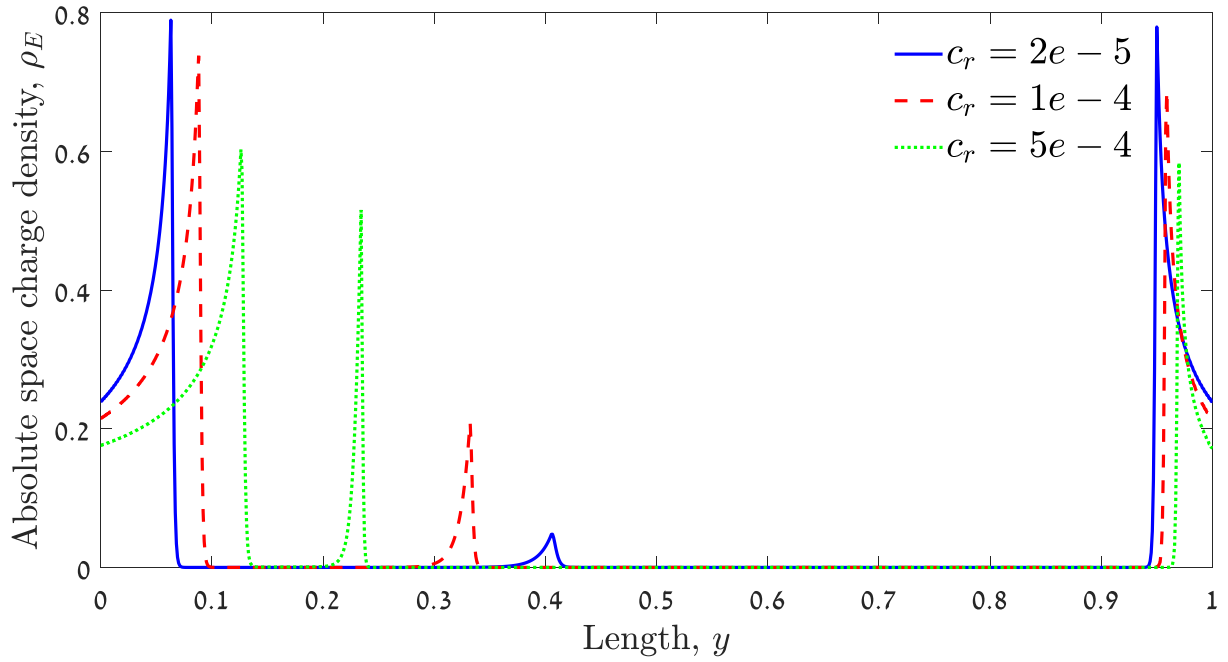


**Figure 26:** Distribution of the absolute value of the non-dimensional space charge density,  $\rho_E$ , obtained for 1D ionic transport between the two open electrodes. The results are obtained for the values of  $\epsilon = 2.5 \times 10^{-4}$ ,  $t = 1.7 \times 10^{-6}$ , and three different values of  $c_r$ .

It is also remarkable that, similarly to the primary ECI, the width of the secondary ESC also has a considerable effect on the wave number of the secondary VP series. In fact, the width of zone 2 on the left side of figure 25(g) is thinner than that on the left side of figure 25(h). As a result, the wave number value of the secondary VP series on the left side of figure 25(g) is higher than that on the left side of figure 25(h).



## 8. HP Indigo Case

HP Indigo's configuration is a private case of electrically-driven multiphase flow. The liquid is an ISOPAR L mixture, which is composed of carrier oil, polymeric ink particles, and a component called charge director (see figure 2). When the mixture flows in the neck between the electrodes of the BID (see figure 5) it splits into the gaps between the DR and the MA or BA (see figure 6), where it is exposed to an electric field. The electric field polarizes the neutral charge director into inverse micelles and breaks up several of them into positive (cation) and negative (anion) charges. At this stage, a large amount of negative charges is bonded to the solid polymeric ink particles, while the rest of them and the positive charges remain in the oil domain. Therefore, the oil domain can be defined as a weak electrolyte which is composed of positively charged cations, negatively charged anions, and negatively charged ink particles of high valence value.

### 8.1 Geometric Dimensions and Mixture Properties

The physical values given in this section are taken from the data provided by HP Indigo engineers. Figure 27 presents a schematic of the gap dimensions between the DR and the electrodes of the BID:

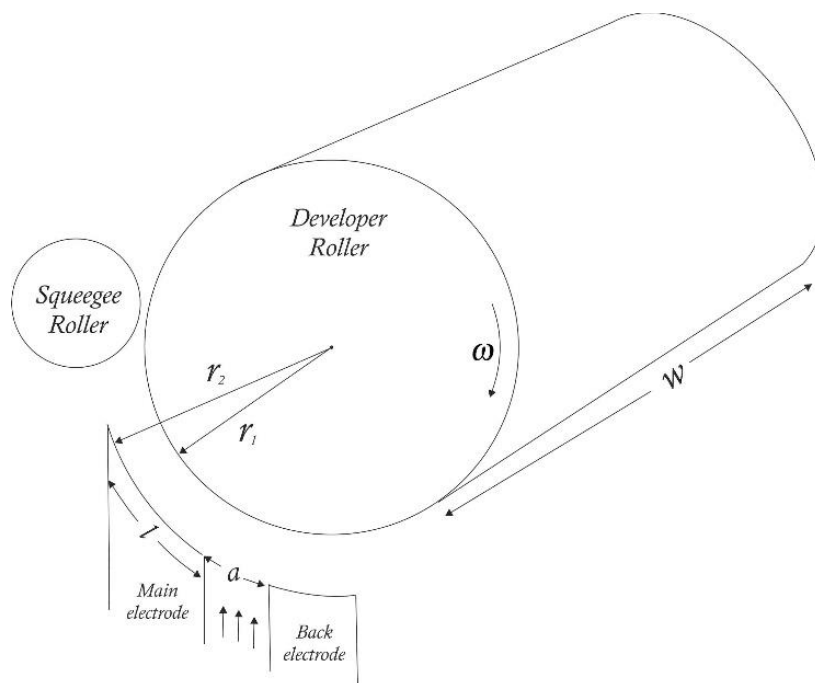


Figure 27: Schematic of the gap dimensions.

Together with HP Indigo engineers, a device called mini Q over M (QoM) was chosen to serve as a prior simulation domain for the BID. QoM is a cylindrical device bounded by two parallel electrodes made of the same material (see figures 28-29). This cylindrical space is filled with an electrolyte oil mixture of known mass. A chosen voltage is applied across the electrodes and a time-dependent value of the current density is obtained. Several reasons led to the decision to use the QoM device:

- Easy to set and determine different initial concentrations of species.
- Feasible to perform experiments on charge director with/without ink particles.
- Top and bottom boundaries are made of the same material. Therefore, for a binary electrolyte, simulation results are expected to be symmetric relative to the center point of the electrolytic cell, which simplifies the validation procedure of the simulation results.
- Feasible to relate to as a 1D solution in space.
- Feasible to assess the species concentration gathered near the boundaries after the electric field is shut down.



Figure 28: HP Mini QoM device.

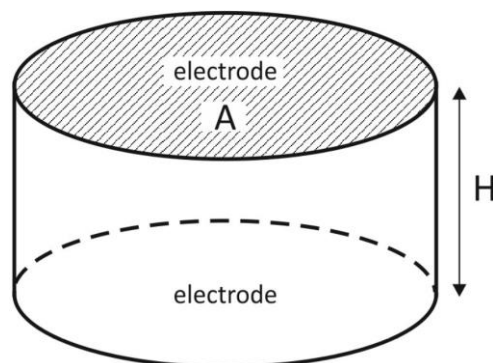


Figure 29: Schematic of mini QoM dimensions.

Table 6 contains the values of the dimensions defined in figures 27,29.

**Table 6: DR-ME gap and QoM geometric dimensions.**

<b>Description</b>	<b>Symbol</b>	<b>Value</b>	<b>Units</b>
Neck width between the BID electrodes	$a$	2	mm
DR radius	$r_1$	36	mm
ME radius from DR center	$r_2$	36.35	mm
DR length	$w$	78.5	cm
ME arc length	$l$	1.8	cm
DR angular velocity	$\omega$	62.83 ( $= 20\pi$ )	rad / s
Length between the QoM electrodes	$H$	0.974	mm
Electrode area of the QoM	$A$	1002	mm <sup>2</sup>

Mixture and species properties are displayed in table 7.

**Table 7: Mixture and species properties.**

Description	Symbol	Value	Units	Comments
Ink mass fraction	$Y_s$	0.03	-	In the neck between the electrodes
Charge director mass fraction	$Y_{cd}$	0.001	-	For anions and cations together
Ink particles density (not porous)	$\rho_s$	1000	kg/m <sup>3</sup>	
Ink particles density (porous)	$\rho_{s\_porous}$	~850	kg/m <sup>3</sup>	Up to a maximal ink mass fraction of ~0.35
Charge director density	$\rho_{cd}$	1100	kg/m <sup>3</sup>	For both anions and cations
Liquid oil density	$\rho_l$	765	kg/m <sup>3</sup>	For 15°C
Liquid oil kinematic viscosity	$\nu_l$	1.64e-6	m <sup>2</sup> /s	For 25°C
Ink particles dynamic viscosity	$\eta_s$	0.003-0.005	Pa·s	For 0.03 mass fraction
Volumetric flow rate in the neck between the electrodes	$Q_{neck}$	30	L/min	
Volumetric flow rate in the gap between the ME and the DR	$Q_{ME-DR}$	~20	L/min	
Volumetric flow rate in the gap between the BE and the DR	$Q_{BE-DR}$	~10	L/min	
Ink particles average diameter	$d_s$	4	µm	
Micelle's average diameter	$d_{cd}$	7	nm	
Percentage of effective micelles	$cd_{eff}$	2	%	
Mixture temperature	$T$	30	°C	
Ink particles electrical mobility	$\mu_s$	1.2e-8	m <sup>2</sup> /V·s	For 0.002 mass fraction. Empirical result
Micelles electrical mobility	$\mu_{cd}$	1.7e-9	m <sup>2</sup> /V·s	For E = 1.5 V/mm . Empirical result
Mixture relative permittivity	$\epsilon_r$	~2	-	For low ink concentration
Electric potential supplied to the DR	$\Psi_{DR}$	-400	V	Considering a reference point
Electric potential supplied to the electrodes	$\Psi_{electrodes}$	-1400	V	Considering a reference point

According to equation (15) and table 7, the mass fraction of the liquid oil is:

$$Y_l = 1 - 0.03 - 0.001 = 0.969. \quad (91)$$

To calculate the mixture properties determined by equation (8), the volume fractions  $\alpha_i$  have to be known. However, the data in table 7 and in equation (91) include only mass fractions. The relation between mass and volume fractions is calculated according to equation (14):

$$\alpha_i = \frac{\rho}{\rho_i} Y_i, \quad (92)$$

which enables reformulating equation (8) as:

$$\beta = \sum_i \frac{\rho}{\rho_i} Y_i \beta_i. \quad (93)$$

Because volume fractions of each species and mixture density are not given, the mixture density will be assumed to be equal to the liquid oil density:

$$\rho \approx \rho_l. \quad (94)$$

The dynamic viscosity of the liquid oil is:

$$\eta_l = \rho_l \cdot \nu_l = 765 \cdot 1.64 \cdot 10^{-6} = 1.255 \cdot 10^{-3} \text{ Pa} \cdot \text{s}. \quad (95)$$

Mixture dynamic viscosity can be calculated due to equations (91) and (93-95), neglecting the dynamic viscosity of the charge director and considering the average value of dynamic viscosity of the ink particles from table 7:

$$\begin{aligned} \eta &= \sum_i \frac{\rho}{\rho_i} Y_i \eta_i \approx \sum_i \frac{\rho_l}{\rho_i} Y_i \eta_i = \frac{\rho_l}{\rho_s} Y_s \eta_s + \frac{\rho_l}{\rho_l} Y_l \eta_l = \\ &= \frac{765}{1000} \cdot 0.03 \cdot 0.004 + \frac{765}{765} \cdot 0.97 \cdot 1.255 \cdot 10^{-3} = 1.309 \cdot 10^{-3} \text{ Pa} \cdot \text{s}. \end{aligned} \quad (96)$$

The tangential component of the average mixture velocity in the ME-DR gap can be calculated from the data given in tables 6-7:

$$\bar{u}_\theta = \frac{Q_{ME-DR}}{w(r_2 - r_1)} = \frac{20 \cdot (1/60000)}{78.5 \cdot 10^{-2} \cdot (36.35 - 36) \cdot 10^{-3}} = 1.213 \frac{\text{m}}{\text{s}}, \quad (97)$$

while the tangential velocity of the DR reads:

$$u_{\theta\_wall} = \omega r_1 = 20\pi \cdot 36 \cdot 10^{-3} = 2.262 \frac{\text{m}}{\text{s}}. \quad (98)$$

The volume of a single spherical ink particle is:

$$V_s = \frac{\pi d_s^3}{6} = \frac{\pi (4 \cdot 10^{-6})^3}{6} = 3.351 \cdot 10^{-17} \text{ m}^3 \quad (99)$$

and the volume of a single spherical charge director (same for anion and cation) is:

$$V_{cd} = \frac{\pi d_{cd}^3}{6} = \frac{\pi (7 \cdot 10^{-9})^3}{6} = 1.796 \cdot 10^{-25} \text{ m}^3. \quad (100)$$

The mass of a single ink or charge director particle can be estimated from equations (99-100), respectively:

$$m_s = \rho_s \cdot V_s = 1000 \cdot 3.351 \cdot 10^{-17} = 3.351 \cdot 10^{-14} \text{ kg}, \quad (101)$$

$$m_{cd} = \rho_{cd} \cdot V_{cd} = 1100 \cdot 1.796 \cdot 10^{-25} = 1.976 \cdot 10^{-22} \text{ kg}. \quad (102)$$

The molar mass of ink and charge director species can be evaluated from equations (101-102), respectively as:

$$M_s = m_s \cdot N_A = 3.351 \cdot 10^{-14} \cdot 6.022 \cdot 10^{23} = 2.018 \cdot 10^{10} \frac{\text{kg}_s}{\text{mol}_s}, \quad (103)$$

$$M_{cd} = m_{cd} \cdot N_A = 1.976 \cdot 10^{-22} \cdot 6.022 \cdot 10^{23} = 118.97 \frac{\text{kg}_{cd}}{\text{mol}_{cd}}. \quad (104)$$

Utilizing equations (14), (103) and (104), the bulk molar concentration of each species can be obtained by:

$$c_{0_s} = \frac{Y_s \rho}{M_s} \approx \frac{Y_s \rho_l}{M_s} = \frac{0.03 \cdot 765}{2.018 \cdot 10^{10}} = 1.137 \cdot 10^{-9} \frac{\text{mol}_s}{\text{m}^3}, \quad (105)$$

$$c_{0_{cd}} = \frac{Y_{cd} \rho}{M_{cd}} \approx \frac{Y_{cd} \rho_l}{M_{cd}} = \frac{0.001 \cdot 765}{118.97} = 6.43 \cdot 10^{-3} \frac{\text{mol}_{cd}}{\text{m}^3}. \quad (106)$$

The bulk concentration of effective micelles, anions and cations together is:

$$c_{0_{cd\_eff}} = c_{0_{cd}} \cdot cd_{eff} = 6.43 \cdot 10^{-3} \cdot 0.02 = 1.286 \cdot 10^{-4} \frac{\text{mol}_{cd}}{\text{m}^3}. \quad (107)$$

In the absence of ink species, the bulk concentration of the anions is assumed to be equal to the bulk concentration of cations. Hence, to ensure initial electroneutrality (see equation (40)):

$$c_0^+ = c_0^- = \frac{c_{0_{cd\_eff}}}{2} = \frac{1.286 \cdot 10^{-4}}{2} = 6.43 \cdot 10^{-5} \frac{\text{mol}_{cd}}{\text{m}^3}. \quad (108)$$

It is difficult to evaluate the valence value for the ink particles and ion species. To do so, it is possible to utilize the electrical mobility equation for the diffusion of charged particles (38). In this case, one should know the molecular diffusion coefficient of each species. Considering a relatively low velocity-based Reynolds number and an averaged radius of ink particles and ions, the molecular diffusivity of each species can be calculated according to the Stokes-Einstein equation (39):

$$D_s = \frac{k_B T}{6\pi\eta \frac{d_s}{2}} = \frac{1.381 \cdot 10^{-23} \cdot 303.15}{6\pi \cdot 1.309 \cdot 10^{-3} \cdot \frac{4 \cdot 10^{-6}}{2}} = 8.483 \cdot 10^{-14} \frac{\text{m}^2}{\text{s}}, \quad (109)$$

$$D_{cd} = \frac{k_B T}{6\pi\eta \frac{d_{cd}}{2}} = \frac{1.381 \cdot 10^{-23} \cdot 303.15}{6\pi \cdot 1.309 \cdot 10^{-3} \cdot \frac{7 \cdot 10^{-9}}{2}} = 4.847 \cdot 10^{-11} \frac{\text{m}^2}{\text{s}}. \quad (110)$$

Substituting these values into equation (38) yields the absolute valence value of each species:

$$|z_s| = \frac{\mu_s k_B T}{D_s e} = \frac{1.2 \cdot 10^{-8} \cdot 1.381 \cdot 10^{-23} \cdot 303.15}{8.483 \cdot 10^{-14} \cdot 1.602 \cdot 10^{-19}} = 3695.41 \approx 3695, \quad (111)$$

$$|z_{cd}| = \frac{\mu_{cd} k_B T}{D_{cd} e} = \frac{1.7 \cdot 10^{-9} \cdot 1.381 \cdot 10^{-23} \cdot 303.15}{4.847 \cdot 10^{-11} \cdot 1.602 \cdot 10^{-19}} = 0.916 \approx 1. \quad (112)$$

Recalculation of the diffusion coefficients based on the rounded integer valence values yields:

$$D_s = \frac{\mu_s k_B T}{|z_s| e} = \frac{1.2 \cdot 10^{-8} \cdot 1.381 \cdot 10^{-23} \cdot 303.15}{3695 \cdot 1.602 \cdot 10^{-19}} = 8.484 \cdot 10^{-14} \frac{\text{m}^2}{\text{s}}, \quad (113)$$

$$D_{cd} = \frac{\mu_{cd} k_B T}{|z_{cd}| e} = \frac{1.7 \cdot 10^{-9} \cdot 1.381 \cdot 10^{-23} \cdot 303.15}{1 \cdot 1.602 \cdot 10^{-19}} = 4.441 \cdot 10^{-11} \frac{\text{m}^2}{\text{s}}. \quad (114)$$

Considering the ink species, the bulk concentration of the effective positive micelles remains as in equation (108), according to equation (112). The negative charges are attributed to both anion and ink species. The bulk concentration of the negative charges attached to the ink particles is calculated due to equations (105) and (111):

$$|z_s| \cdot c_{0_s} = 3695 \cdot 1.137 \cdot 10^{-9} = 4.202 \cdot 10^{-6} \frac{\text{mol}_s}{\text{m}^3} \quad (115)$$

Hence, to ensure the initial electroneutrality condition determined in equation (40), the bulk concentration of the remaining anions yields:

$$c_0^- = \frac{-z^+ c_0^+ - z_s \cdot c_{0_s}}{z^-} = \frac{-6.43 \cdot 10^{-5} - (-4.202 \cdot 10^{-6})}{-1} = 6.01 \cdot 10^{-5} \frac{\text{mol}_-}{\text{m}^3}. \quad (116)$$

The electric potential difference between the DR and the BID electrodes is:

$$\Delta V = \Psi_{DR} - \Psi_{electrodes} = -400 - (-1400) = 1000 \text{ V}, \quad (117)$$

while common values of the voltage applied across the QoM electrodes are 500 V or 1500 V.

Following the dimensional analysis characterized by stationary boundaries, as introduced in section 5.1.1, the non-dimensional numbers can be calculated for HP Indigo's QoM configuration. Consider the characteristic velocity  $u_0$ , as it appears in equation (42), and the characteristic length  $l_0$  as the length between the QoM electrodes  $H$  (see table 6), the non-dimensional numbers obtained are as follows:

Schmidt number (see equation (58)):

$$Sc = \frac{\eta}{\rho D^+} \approx \frac{\eta}{\rho_l D^+} = \frac{1.309 \cdot 10^{-3}}{765 \cdot 4.441 \cdot 10^{-11}} = 3.852 \cdot 10^4. \quad (118)$$

Péclet number (see equation (59)):

$$\begin{aligned} Pe &= \frac{u_0 l_0}{D^+} = \frac{\varepsilon}{\eta l_0} V_T^2 \frac{l_0}{D^+} = \frac{\varepsilon_r \varepsilon_0}{\eta D^+} \left( \frac{k_B T}{z^+ e} \right)^2 = \\ &= \frac{2 \cdot 8.854 \cdot 10^{-12}}{1.309 \cdot 10^{-3} \cdot 4.441 \cdot 10^{-11}} \left( \frac{1.381 \cdot 10^{-23} \cdot (30 + 273.15)}{1 \cdot 1.602 \cdot 10^{-19}} \right)^2 = 0.208. \end{aligned} \quad (119)$$

Electrostatic screening length (see equation (62)):

$$\begin{aligned} \epsilon &= \frac{\lambda_D}{l_0} = \frac{1}{l_0} \sqrt{\frac{\varepsilon k_B T}{2(z^+ e)^2 c_0^+ N_A}} = \frac{1}{H} \sqrt{\frac{\varepsilon_r \varepsilon_0 k_B T}{2(z^+ e)^2 c_0^+ N_A}} = \\ &= \frac{1}{0.974 \cdot 10^{-3}} \sqrt{\frac{2 \cdot 8.854 \cdot 10^{-12} \cdot 1.381 \cdot 10^{-23} \cdot (30 + 273.15)}{2(1 \cdot 1.602 \cdot 10^{-19})^2 \cdot 6.43 \cdot 10^{-5} \cdot 6.022 \cdot 10^{23}}} = 1.982 \cdot 10^{-4}. \end{aligned} \quad (120)$$

Considering common values of the voltage applied across the QoM electrodes,  $\Delta V = 500$  or 1500 V, the non-dimensional voltage applied is:

$$V = \frac{\Delta V}{V_T} = \frac{\Delta V}{\left( \frac{k_B T}{z^+ e} \right)} = \frac{\Delta V}{\left( \frac{1.381 \cdot 10^{-23} \cdot (30 + 273.15)}{1 \cdot 1.602 \cdot 10^{-19}} \right)} = 1.914 \cdot 10^4 \text{ or } 5.742 \cdot 10^4. \quad (121)$$

For the case of a non-symmetric electrolyte consisting of a single positively charged species of valence  $z_1 = z^+$  and two negatively charged species of valences  $z_2 = z^-$  and  $z_3 = z_s = Mz^-$ , the non-dimensional numbers  $z_{r_i}$ ,  $D_{r_i}$ , and  $c_{r_i}$  obtained are:



$$z_{r_i} = \frac{z_i}{z_1}; \quad z_{r_2} = \frac{z_2}{z_1} = \frac{-1}{1} = -1, \quad z_{r_3} = \frac{z_3}{z_1} = \frac{Mz_2}{z_1} = Mz_{r_2} = -3695 \rightarrow M = 3695; \quad (122)$$

$$D_{r_i} = \frac{D_i}{D_1}; \quad D_{r_2} = \frac{D_2}{D_1} = \frac{4.441 \cdot 10^{-11}}{4.441 \cdot 10^{-11}} = 1, \quad D_{r_3} = \frac{D_3}{D_1} = \frac{8.484 \cdot 10^{-14}}{4.441 \cdot 10^{-11}} = 1.91 \cdot 10^{-3}; \quad (123)$$

$$c_r = \frac{c_3}{c_2} \text{ at } (t=0) = \frac{c_{0-s}}{c_0^-} = \frac{1.137 \cdot 10^{-9}}{6.01 \cdot 10^{-5}} = 1.892 \cdot 10^{-5}. \quad (124)$$

Substituting the non-dimensional numbers into the governing equations (50) yields:

$$\begin{aligned} \vec{\nabla} \cdot \vec{u} &= 0 \\ 2.596 \cdot 10^{-5} \left( \frac{\partial \vec{u}}{\partial t} + 0.208 \vec{u} \cdot \vec{\nabla} \vec{u} \right) &= -\vec{\nabla} P + \nabla^2 \vec{u} - 1.272 \cdot 10^7 (c^+ - c^- - 3695 c_s) \vec{\nabla} \Psi \\ -7.86 \cdot 10^{-8} \nabla^2 \Psi &= c^+ - c^- - 3695 c_s \\ \frac{\partial c^\pm}{\partial t} &= \vec{\nabla} \cdot \left( -0.208 c^\pm \vec{u} + \vec{\nabla} c^\pm \pm c^\pm \vec{\nabla} \Psi \right) \\ \frac{\partial c_s}{\partial t} &= \vec{\nabla} \cdot \left( -0.208 c_s \vec{u} + 1.91 \cdot 10^{-3} \vec{\nabla} c_s - 7.059 c_s \vec{\nabla} \Psi \right), \end{aligned} \quad (125)$$

and into the electric current density calculation introduced in equation (49) yields:

$$I_y = \left| \frac{1}{AR} \int_{AR} \left[ 0.208 u_y (c^+ - c^- - 3695 c_s) - \frac{\partial}{\partial y} (c^+ - c^- - 7.059 c_s) - \frac{\partial \Psi}{\partial y} (c^+ + c^- + 2.608 \cdot 10^4 c_s) - 7.86 \cdot 10^{-8} \frac{\partial^2 \Psi}{\partial y \partial t} \right]_{x, y=y_0, t} dx \right|. \quad (126)$$

As can be seen from the set of governing equations (125), the flow is mainly dominated by the electric body force acting on the mixture. In addition, the electroneutrality condition determined in equation (40) seems to be preserved, except for the ESC regions where the potential Laplacian is significant. The transport of anion and cation species is dominated by all advection, molecular diffusion, and electromigration phenomena, while the molecular diffusion of ink species seems to be negligible. As can be seen from equation (126), the contribution of the displacement current density to the total current density calculation is negligible.

Following the dimensional analysis characterized by the moving DR boundary as introduced in section 5.1.2, the non-dimensional numbers can be calculated for HP Indigo's BID configuration. Considering the characteristic velocity  $u_0$ , as appears in equation (97), and the characteristic length  $l_0$  as the hydraulic diameter  $D_H$  (see equation (51)) of the ME-DR duct (for Reynolds number calculation) or the ME-DR distance  $H$  (for electrostatic screening length calculation), the non-dimensional numbers obtained are as follows:

The Schmidt number, as well as the non-dimensional numbers  $z_i$ ,  $D_i$ , and  $c_i$ , remains the same as for the stationary configuration (see equations (118,122,123) and (124), respectively).

The Reynolds number (see equation (57)) is:

$$\begin{aligned} Re &= \frac{\rho u_0 l_0}{\eta} = \frac{\rho \bar{u}_\theta D_H}{\eta} = \frac{\rho \bar{u}_\theta}{\eta} \frac{4A}{p} = \frac{\rho \bar{u}_\theta}{\eta} \frac{4w(r_2 - r_1)}{2(w + r_2 - r_1)} = \\ &= \frac{765 \cdot 1.213}{1.309 \cdot 10^{-3}} \cdot \frac{4 \cdot 78.5 \cdot 10^{-2} (36.35 - 36) \cdot 10^{-3}}{2(78.5 \cdot 10^{-2} + (36.35 - 36) \cdot 10^{-3})} = 4.962 \cdot 10^2. \end{aligned} \quad (127)$$

The electrohydrodynamic coupling constant (see equation (60)) is:

$$\begin{aligned} \kappa &= \frac{\varepsilon}{\eta D^+} V_T^2 = \frac{\varepsilon_r \varepsilon_0}{\eta D^+} \left( \frac{k_B T}{z^+ e} \right)^2 = \frac{2 \cdot 8.854 \cdot 10^{-12}}{1.309 \cdot 10^{-3} \cdot 4.441 \cdot 10^{-11}} \left( \frac{1.381 \cdot 10^{-23} \cdot (30 + 273.15)}{1.1.602 \cdot 10^{-19}} \right)^2 = \\ &= 0.208. \end{aligned} \quad (128)$$

The electrostatic screening length (see equation (62)) is:

$$\begin{aligned} \epsilon &= \frac{\lambda_D}{l_0} = \frac{1}{H} \sqrt{\frac{\varepsilon k_B T}{2(z^+ e)^2 c_0^+ N_A}} = \frac{1}{r_2 - r_1} \sqrt{\frac{\varepsilon_r \varepsilon_0 k_B T}{2(z^+ e)^2 c_0^+ N_A}} = \\ &= \frac{1}{(36.35 - 36) \cdot 10^{-3}} \sqrt{\frac{2 \cdot 8.854 \cdot 10^{-12} \cdot 1.381 \cdot 10^{-23} \cdot (30 + 273.15)}{2(1.1.602 \cdot 10^{-19})^2 \cdot 6.43 \cdot 10^{-5} \cdot 6.022 \cdot 10^{23}}} = 5.517 \cdot 10^{-4}. \end{aligned} \quad (129)$$

According to equation (117), the non-dimensional voltage applied between the ME and DR is:

$$V = \frac{\Delta V}{V_T} = \frac{\Delta V}{\left( \frac{k_B T}{z^+ e} \right)} = \frac{1000}{\left( \frac{1.381 \cdot 10^{-23} \cdot (30 + 273.15)}{1.1.602 \cdot 10^{-19}} \right)} = 3.828 \cdot 10^4. \quad (130)$$

Substituting the non-dimensional numbers into the governing equations (56) yields:

$$\begin{aligned} \vec{\nabla} \cdot \vec{u} &= 0 \\ \frac{\partial \vec{u}}{\partial t} + \vec{u} \cdot \vec{\nabla} \vec{u} &= -\vec{\nabla} P + 2.015 \cdot 10^{-3} \nabla^2 \vec{u} - 3.602 \cdot 10^{-5} (c^+ - c^- - 3695 c_s) \vec{\nabla} \Psi \\ -6.087 \cdot 10^{-7} \nabla^2 \Psi &= c^+ - c^- - 3695 c_s \\ \frac{\partial c^\pm}{\partial t} &= \vec{\nabla} \cdot (-c^\pm \vec{u} + 5.232 \cdot 10^{-8} \vec{\nabla} c^\pm \pm 5.232 \cdot 10^{-8} c^\pm \vec{\nabla} \Psi) \\ \frac{\partial c_s}{\partial t} &= \vec{\nabla} \cdot (-c_s \vec{u} + 9.994 \cdot 10^{-11} \vec{\nabla} c_s - 3.693 \cdot 10^{-7} c_s \vec{\nabla} \Psi), \end{aligned} \quad (131)$$

and into the electric current density calculation introduced in equation (49):

$$I_y = \left| \frac{1}{AR} \int_{AR} \left[ u_y (c^+ - c^- - 3695c_s) - 5.232 \cdot 10^{-8} \frac{\partial}{\partial y} (c^+ - c^- - 7.059c_s) - \right. \right. \\ \left. \left. 5.232 \cdot 10^{-8} \frac{\partial \Psi}{\partial y} (c^+ + c^- + 2.608 \cdot 10^4 c_s) - 6.087 \cdot 10^{-7} \frac{\partial^2 \Psi}{\partial y \partial t} \right] \right|_{x, y=y_0, t} dx. \quad (132)$$

As can be seen from the set of governing equations (131), the flow is mainly dominated by the mixture pressure. In addition, the electroneutrality condition determined in equation (40) seems to be preserved, except for the ESC regions where the potential Laplacian is significant. The transport of anion, cation, and ink species is dominated by the advection phenomenon. As can be seen from equation (132), the electric current density is dominated by the advective phenomenon, although the  $y$  component (or  $r$  in cylindrical coordinates) of the mixture velocity yields relatively small values.

## 8.2 Assumptions

Several assumptions have to be made when solving the two-way coupled physical model introduced in chapter 5 for HP Indigo's configuration. This section discusses these assumptions, their justification and how well they fit the physics of the problem:

1. Incompressible flow – mixture density is constant in space and time.
2. To compute mixture properties by equation (93), mixture density is assumed to be equal to the density of the liquid oil (see equation (94)).
3. Assumptions related to the mixture method: ink particles and ions are considered as non-inertial particles, and there is no drag force between the species.
4. Newtonian mixture - shear stress is proportional to the flow strain.
5. Constant dynamic viscosity of the mixture.
6. Gravitation force is negligible because of the particles' low mass.
7. Constant permittivity of the mixture.
8. Isothermal flow - constant temperature of the mixture.
9. Any impact of a magnetic field is negligible.
10. No dependence of particles' properties on distribution function is assumed.
11. Average radius of particles and ions is utilized in Stokes-Einstein (39) and molar mass (103-104) equations.

12. Calculation of molecular diffusion coefficient of species is performed by utilizing Stokes-Einstein equation (39) – suitable for low values of Reynolds number, based on the relative velocity.

13. Constant values of molecular diffusion coefficients of all the species are assumed.

14. The equivalent valence of all the species is calculated by the electrical mobility equation (38), employing the previously calculated molecular diffusion coefficients of the species and empirical electrical mobility values (see table 7).

15. Species valences are constant and do not depend on the magnitude of electric field. This assumption means that the initial ionic composition of the solution subjected to the electric field is built a very short time after the charge director was broken up into positive and negative charges.

Assumption 1 is an approximation. In the reality, negatively charged ink particles are attracted to the DR and increase the mixture density in this area. The relative error between solid ink particle density and liquid oil density is:

$$Err_{\rho} = \frac{|\rho_l - \rho_s|}{\rho_l} \cdot 100\% = \frac{|765 - 1000|}{765} \cdot 100\% = 30.72\%, \quad (133)$$

but the initial ink concentration value is relatively small (see equation (105)).

Stokes relaxation time is determined by equation (6) for the ink particles:

$$\tau_p = \frac{\rho_s d_s^2}{18\eta_l} = \frac{1000 \cdot (4 \cdot 10^{-6})^2}{18 \cdot 1.25 \cdot 10^{-3}} = 0.71 \mu\text{s}, \quad (134)$$

which means that the solid ink particles reach their steady velocity (approximately the fluid velocity), very quickly. The non-dimensional Stokes number is defined as the ratio between the characteristic time of a particle determined by equation (6) and a characteristic time of the surrounding flow:

$$Stk = \frac{\tau_p u_0}{l_0}, \quad (135)$$

where  $u_0$  and  $l_0$  are the characteristic velocity of the flow and the characteristic length of the bounding geometry, respectively. Considering  $u_0$  as the tangential DR velocity given by equation (98) and  $l_0$  as the distance between the ME and the DR:

$$Stk = \frac{0.71 \cdot 10^{-6} \cdot 2.262}{350 \cdot 10^{-6}} = 4.6 \cdot 10^{-3}. \quad (136)$$

Alternatively, considering  $u_0$  as the average velocity between the ME and the DR and  $l_0$  as the hydraulic diameter  $D_H$  of the ME-DR duct introduced by equations (97) and (51), respectively:

$$Stk = \frac{0.71 \cdot 10^{-6} \cdot 1.213}{\left( \frac{4 \cdot 78.5 \cdot 10^{-2} \cdot 350 \cdot 10^{-6}}{2(78.5 \cdot 10^{-2} + 350 \cdot 10^{-6})} \right)} = 1.2 \cdot 10^{-3}. \quad (137)$$

A particle with low a Stokes number follows fluid streamlines, which means that it is considered to be a non-inertial particle. From the Stokes relaxation time value presented in equation (134), the relative velocity between the particles and the fluid tends to zero after a short time duration, which means that the drag force between them is negligible. Therefore, considering the mixture method (assumption 3) is well justified.

Assumption 5 is a private case of assumption 4. According to HP Indigo's experimental results, the fluid dynamic viscosity increases significantly (approximately times three) in the dense particle region close to the DR. Therefore, the above assumption can introduce non-negligible imprecisions. First, it is necessary to verify the numerical simulations with this simplifying assumption. In future simulations, this assumption will be omitted.

Assumption 6 is mainly introduced to simplify an understanding of the balance of physical forces in the obtained numerical results.

According to the information provided by HP Indigo's engineers, the mixture permittivity of ISOPAR L is approximately constant for a low mass fraction value of solid particles, which is the case under consideration. Therefore, assumption 7 is well justified.

According to the information provided by HP Indigo's engineers, temperature differences are negligible (assumption 8). Note that taking into account the existence of temperature gradients would significantly increase the complexity of the physical model: a thermal diffusion term would have to be added to the Nernst-Planck equation (36) due to thermophoresis phenomena, and the energy equation (12) would have to be solved.

The Hartmann number is the ratio between the electromagnetic and viscous forces, defined as:

$$Ha = BL \sqrt{\frac{\sigma}{\eta}}, \quad (138)$$

where  $B$  is the magnetic field intensity and  $\sigma$  is the electrical conductivity per unit length. According to HP Indigo's engineers, the electrical conductivity per unit length of the ISOPAR

L mixture is about  $100 \div 250$  pS/cm . Considering a high valued conductivity and a relatively high magnetic field intensity of 1 T, the Hartmann number is obtained as:

$$Ha = Bl_0 \sqrt{\frac{\sigma}{\eta}} \approx 1.350 \cdot 10^{-6} \cdot \sqrt{\frac{250 \cdot 10^{-12} \cdot 10^2}{1.309 \cdot 10^{-3}}} = 1.5 \cdot 10^{-6}. \quad (139)$$

For low Hartmann numbers, the impact of a magnetic field is negligible (assumption 9).

As discussed previously in this section, the relative velocity between the particles and the fluid tends to zero. Therefore, assumption 12 is well justified.

According to the information provided by the HP Indigo's engineers, in the time that passes from the charge director exposure to the electric field until it breaks up and particle and ion valences are determined, the mixture flows nearly the first third of the ME-DR duct length. This means that assumption 15 is weak and can be the culprit of a significant uncertainty of the developed model. Relaxing this assumption will require further development of the model relating to the electric field with the valence of each species. This challenge will be addressed in future work.

### 8.3 QoM Simulations

This section summarizes the simulation results addressing the QoM device shown in figures 28-29. One measurable parameter in the QoM device is the electric current density generated right after an electric field is applied. The current density calculation determined in equation (41) is employed on a surface parallel to the QoM electrodes, located at height  $\tilde{y}_0$  from its bottom. To choose a specific value of  $\tilde{y}_0$ , a transient 1D Matlab simulation utilizing the PNP equations (35-36) (without the contribution of the advective term) for the case of a symmetric binary electrolyte was executed. Dirichlet BCs of zero concentration were employed on both electrodes, while the electric potential difference was set to 1500 V. The ICs within the computational domain were:

$$c_0^\pm = 10^{-5} \frac{\text{mol}}{\text{m}^3}, \quad \Psi = 0. \quad (140)$$

The mixture properties considered are as given in section 8.1. 6000 grid points non-uniformly spaced within a 1 mm height were considered with a time step of 1  $\mu$ s. The current density value calculated due to any height value  $\tilde{y}_0$  within the computational domain is presented in figure 30 for 10 different times. As expected, the current density values decrease according with time as the electrodes discharge. Sharp spikes typical of the flux term distribution close to the boundaries result from the discontinuity in the gradient of species concentration due to the presently utilized zero Dirichlet BC. Another interesting observation can be made with regards to the presence of spikes of negligibly small height separating between the bulk and the adjacent ESC. Next, if the

current density is constant in the whole domain (except for the boundaries) at any time, the specific location of the current density calculation  $\tilde{y}_0$  is not important. Throughout this work, for the sake of simplicity, the current density calculation is employed in the middle section between both the bottom and the top boundaries.

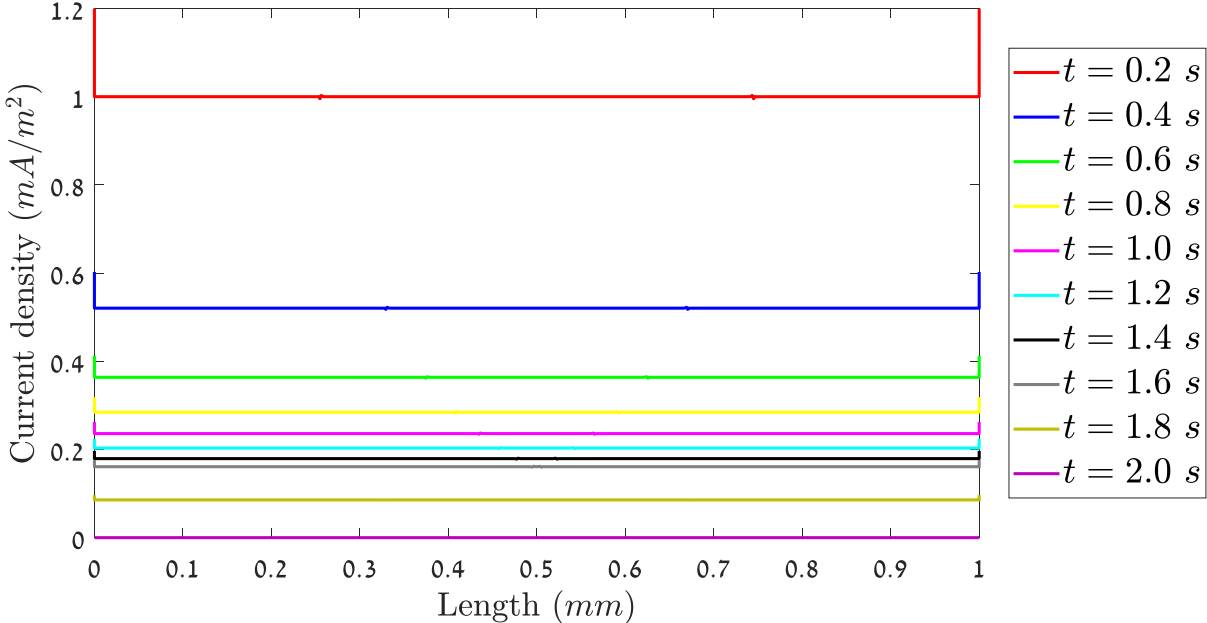


**Figure 30: Absolute current density through any height value  $\tilde{y}_0$  for 10 different times.**

Recently, several QoM experiments were conducted by Indigo's engineers for the symmetric binary electrolyte, including various initial concentrations of positive and negative micelles immersed within the oil medium. The experiments were conducted to validate the numerical simulations. Comparisons between the results obtained by 1D Matlab numerical simulations for 1500V and 500V applied voltages and the corresponding experimental data are shown in figures 31-32, respectively.

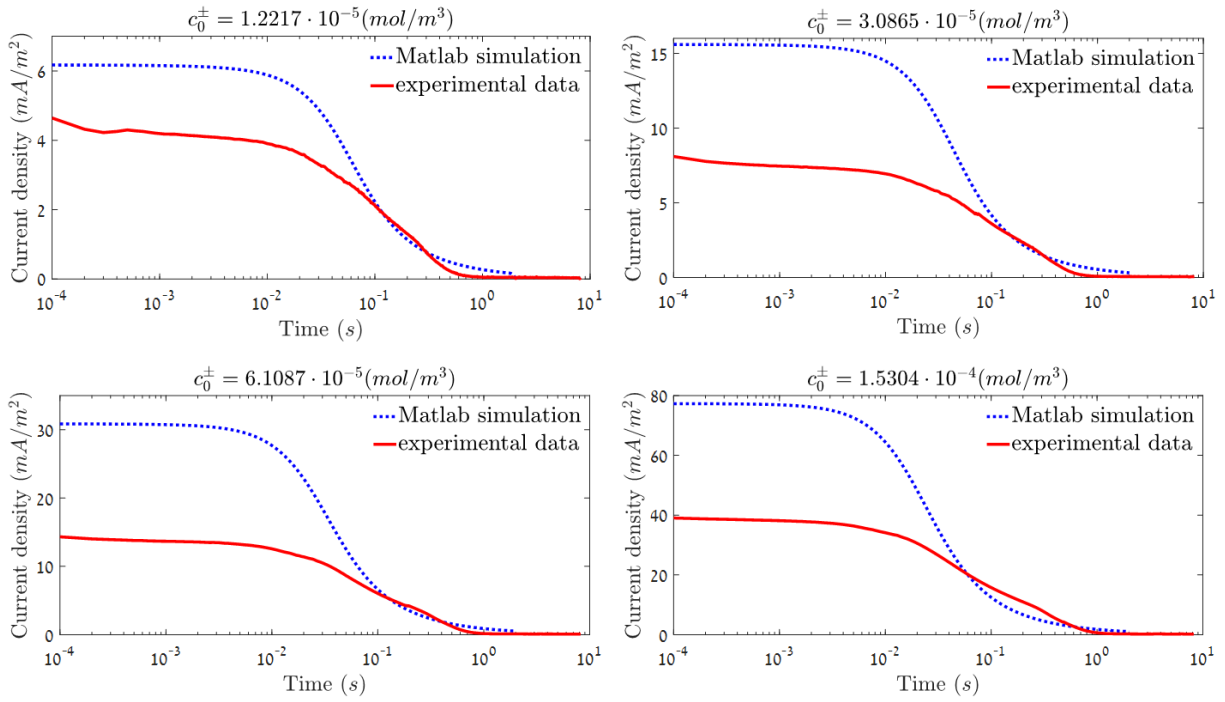


**Figure 31: Current density received due to applied voltage of 1500V for different initial micelles concentration.**

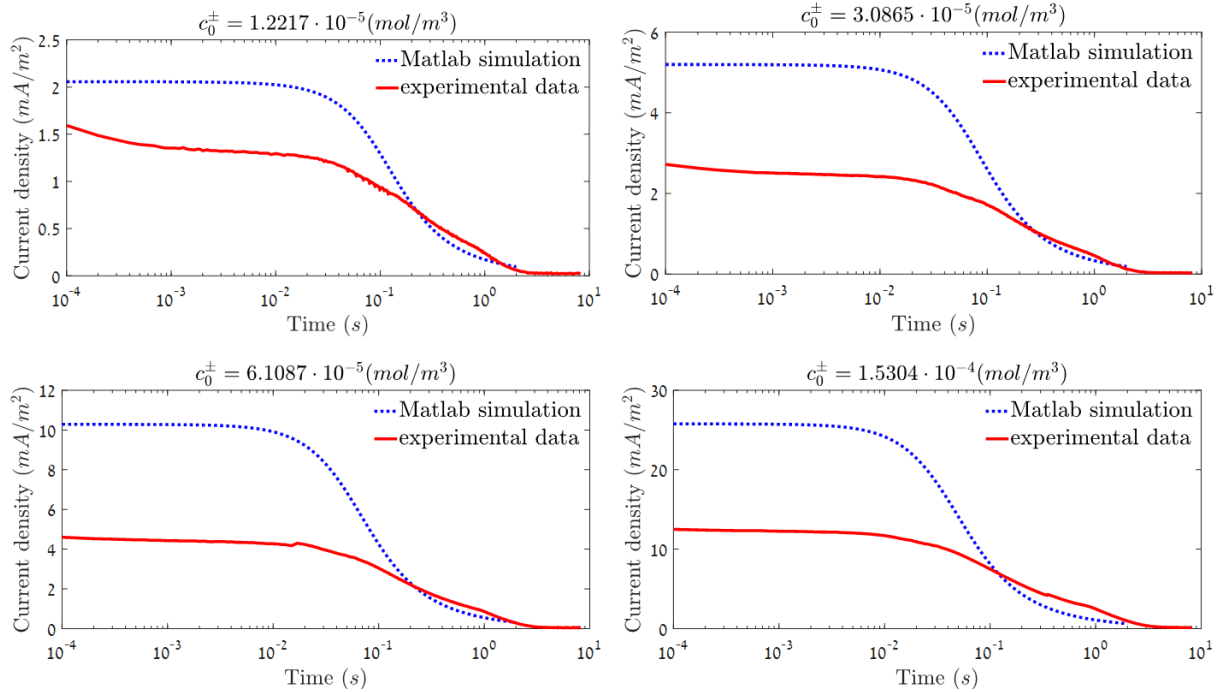


**Figure 32: Current density received due to applied voltage of 500V for different initial micelles concentration.**

The above results display a factor of  $\sim 1.2$ - $2.3$  between the initial current density obtained due to both experimental and numerical approaches. One should note that the current density obtained



from the simulations is proportional to the initial concentration of both species. As mentioned in chapter 7, when considering the first time steps the concentration gradient and the time variation of the electric field are both neglected at the center point of the electrolytic cell. Therefore, the only term that contributes to the electric current density determined in equation (41) at the first time steps is the electromigration term presented in equation (37), which is proportional to the concentration of both species (since the gradient of the electric potential is constant in the bulk at the onset time). There may be several reasons which can cause the differences observed between the experimental and the simulation results:

- The initial concentration values utilized in the Matlab program were calculated in the same way as presented in section 8.1. The calculation is based on the different values of the mass fraction of the charge director and on the assumption of a certain percentage of the effective micelles (see table 7). An imprecise calculation of either the mass fraction of the charge director in the different experiments or the percentage of the effective micelles can change the values of the current density received from the simulations. It should be mentioned that the dynamic viscosity value of the oil carrier, as well as the micelles average diameter and electrical mobility data presented in table 7, can contain high uncertainties.
- The influence of hydrodynamics is not accounted for in the 1D simulations.

Further research should be performed in the future to improve the calibration and accuracy of the above-mentioned parameters (see section 9.2). To calibrate the results provided by the numerical simulation with the given non-precise physical properties, a model of a correction coefficient  $\alpha(c_0^\pm)$  is suggested next. The initial current densities received from 12 different simulations and experimental results are demonstrated in figure 33 as a function of the initial bulk density. Linear curves were fitted to the points representing the simulation results, whereas quadratic curves were fitted to the points representing the experimental results. The fitted curve equations obtained are as follows:

$$\begin{aligned}
 & \text{linear fit: } ax + b \quad ; \quad \text{quadratic fit: } cx^2 + dx + e \\
 \text{simulated 1500V:} & \quad a = 5.0500 \cdot 10^5, \quad b = 3.7733 \cdot 10^{-3}; \\
 \text{simulated 500V:} & \quad a = 1.6836 \cdot 10^5, \quad b = 6.6053 \cdot 10^{-4}; \\
 \text{experimental 1500V:} & \quad c = 2.2615 \cdot 10^8, \quad d = 1.9714 \cdot 10^5, \quad e = 2.0694; \\
 \text{experimental 500V:} & \quad c = 7.3722 \cdot 10^7, \quad d = 6.1443 \cdot 10^4, \quad e = 0.8133.
 \end{aligned} \tag{141}$$

Next, a simple model is suggested to predict the initial current density suitable for any initial bulk concentration:

$$\alpha(x) \cdot (ax + b) = cx^2 + dx + e, \tag{142}$$

where a-e coefficients are determined by the linear or quadratic fitting curves as introduced by equation (141),  $x$  represents the calculated bulk concentration and  $\alpha(x)$  is the correction coefficient. For a given measured initial bulk concentration, the multiplication of the suitable  $\alpha$  value with the calculated bulk concentration (as obtained by the process presented in section 8.1) can serve as an input bulk concentration for the numerical program. This approach ensures equal values of both simulated and experimental initial current densities.  $\alpha$  values obtained by the fitted curves that appear in figure 33 are shown in figure 34.

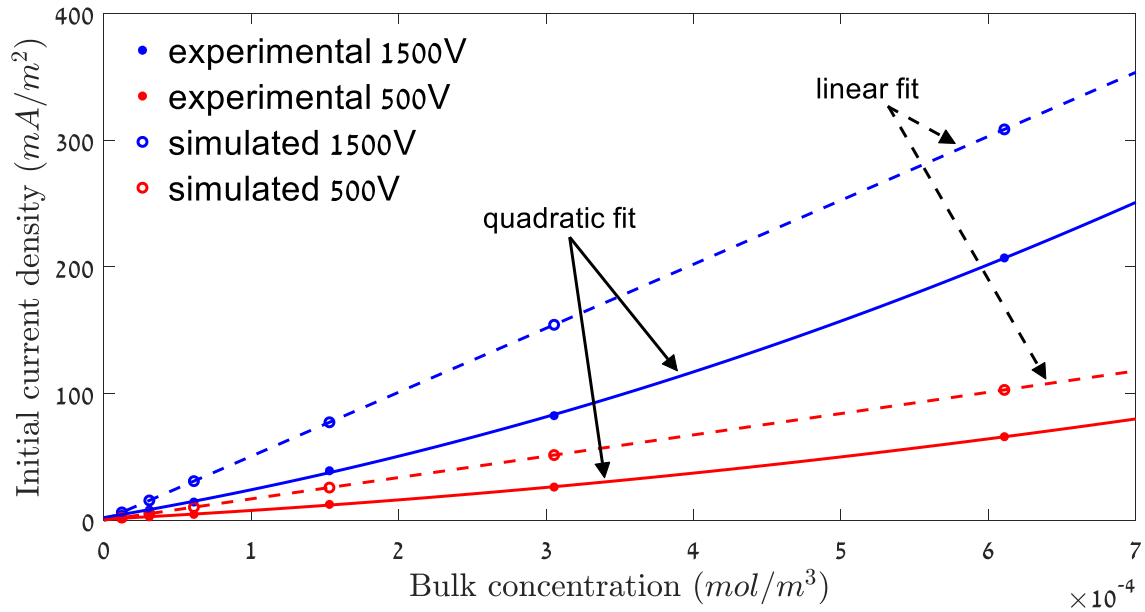


**Figure 33: Fitted curves for initial current density (time  $10^{-4}$  s) obtained by both simulated and experimental results as a function of the micelles bulk concentration.**

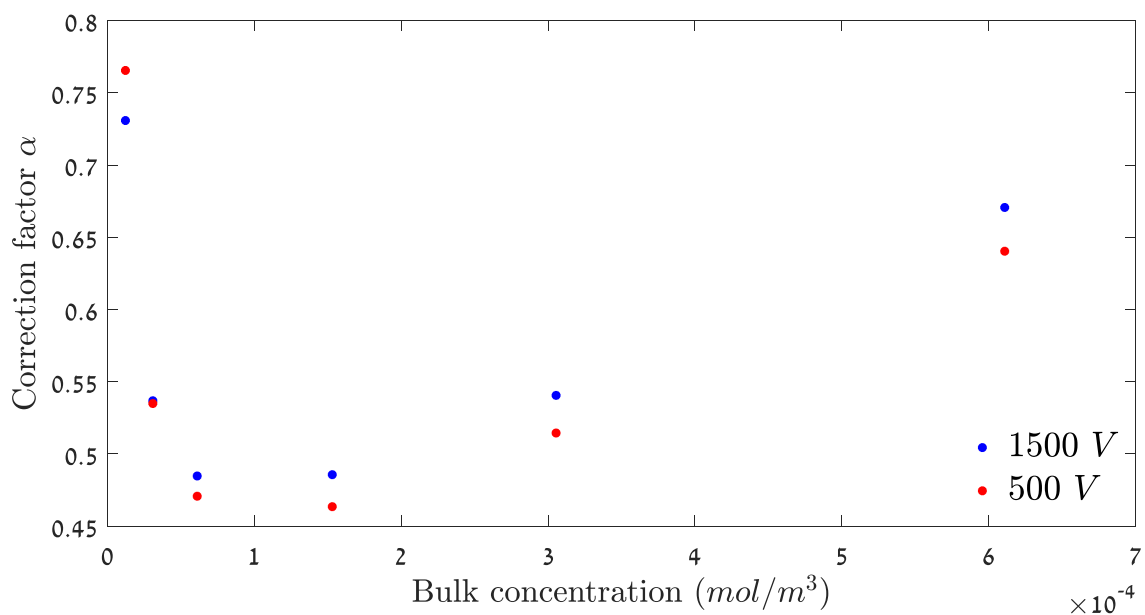


**Figure 34: Values of the correction coefficient  $\alpha$  as a function of the micelles bulk concentration.**

To perform a reliable fitting for the correction coefficient points appearing in figure 34, additional experiments are required. The numerical simulations were re-executed with the corrected bulk concentration values obtained by utilizing the  $\alpha$  values appearing in figure 34. The results of these simulations are compared with the experimental results and shown in figures 35-36:

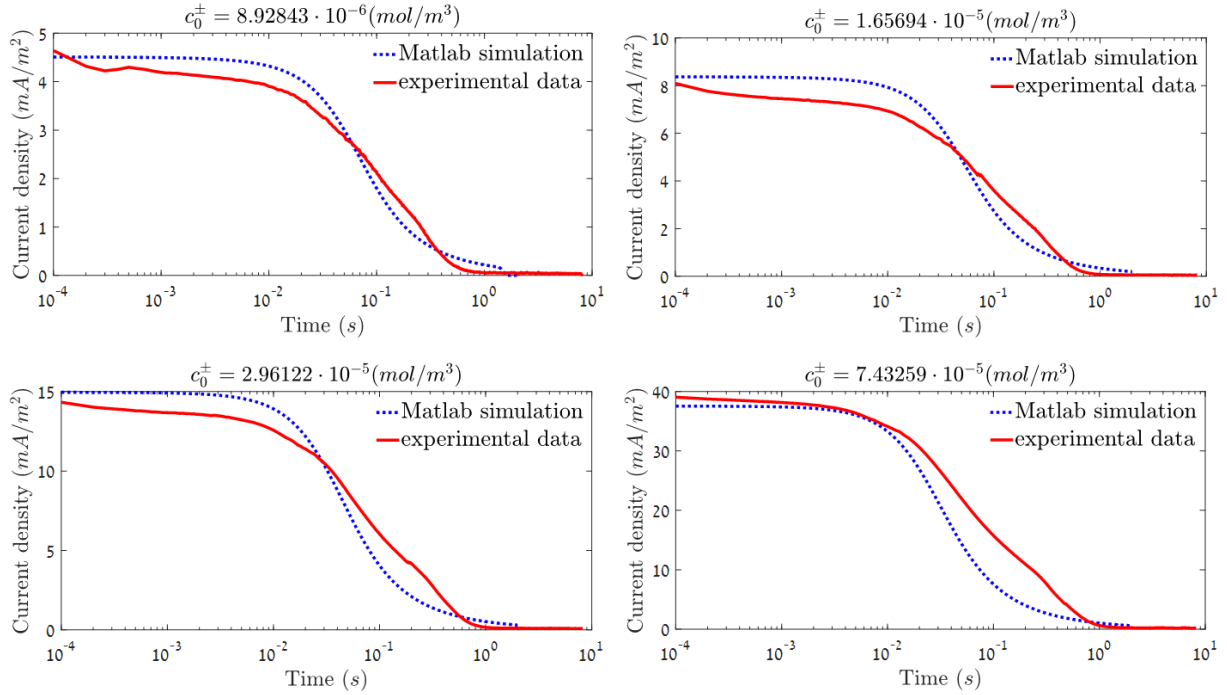


**Figure 35: Corrected current density prediction according to the utilized  $\alpha$  model due to applied voltage of 1500V for different initial micelles concentration.**

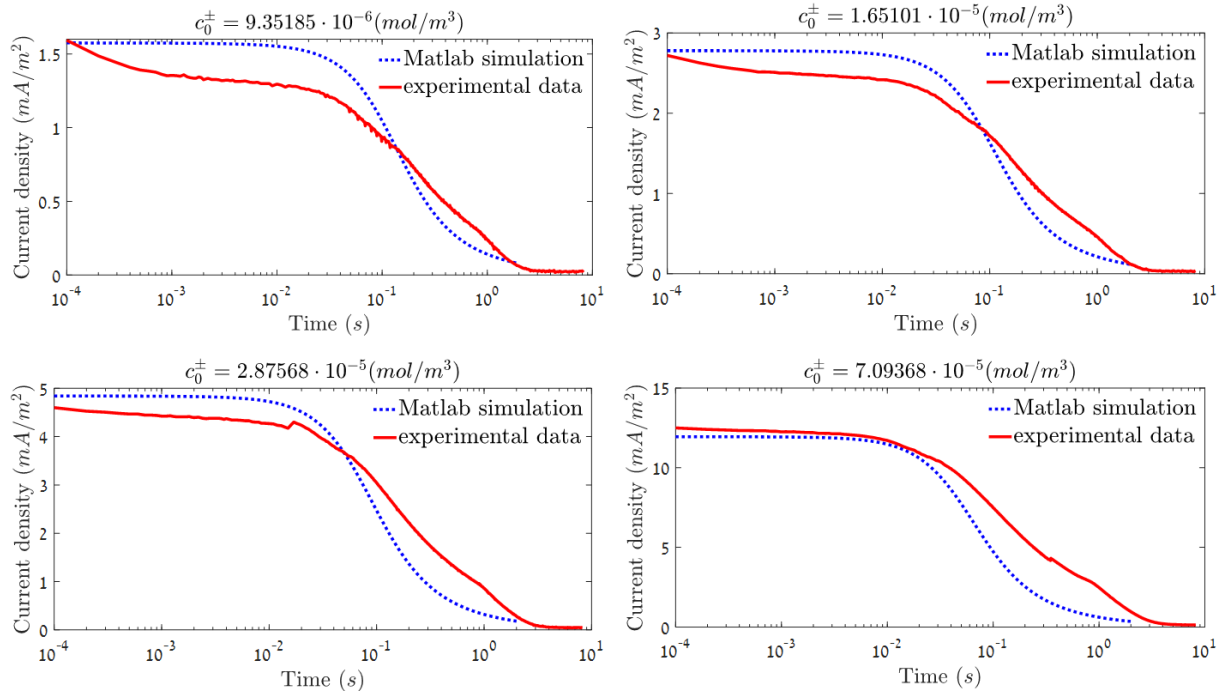


**Figure 36: Corrected current density prediction according to the utilized  $\alpha$  model due to applied voltage of 500V for different initial micelles concentration.**

As can be seen from figures 35-36, the current density predicted by the simulations exhibits a much better fit to the experimental results compared to those presented in figures 31-32.

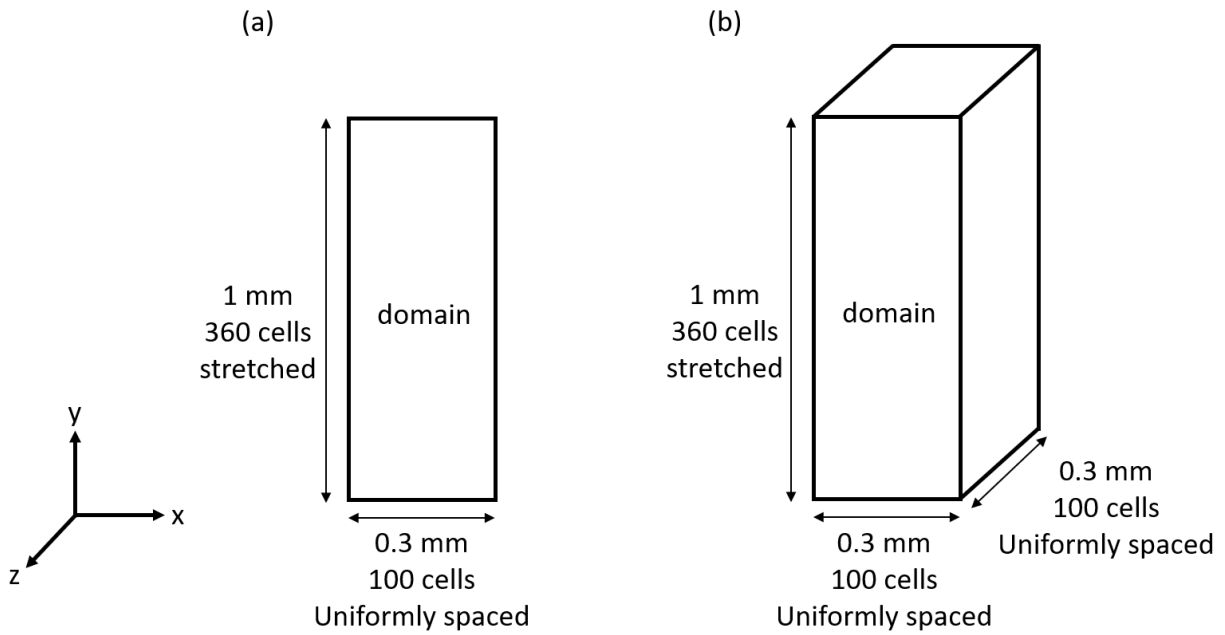
Up to this stage, results were only demonstrated for 1D simulations of the QoM device, considering a symmetric binary electrolyte. We next show results of 2D and 3D QoM simulations through the EC patterns developing in the vicinity of the top and bottom electrodes, operating with both 2 species (no ink) and 3 species (including ink) electrolytes. Considering the 2D geometry and mesh demonstrated in figure 37(a), two simulations were executed addressing the different electrolytes. The set of dimensioned governing equations (26,34-36) is solved with the BCs:

$$\begin{aligned}
\text{2 species: } \tilde{y} = 0: \quad & \frac{\partial \tilde{c}^+}{\partial \tilde{y}} = 0, \quad \tilde{J}_y^- = 0, \quad \tilde{\Psi} = -750 \text{ V}, \quad \tilde{\vec{u}} = \vec{0}, \\
\tilde{y} = H: \quad & \tilde{J}_y^+ = 0, \quad \frac{\partial \tilde{c}^-}{\partial \tilde{y}} = 0, \quad \tilde{\Psi} = 750 \text{ V}, \quad \tilde{\vec{u}} = \vec{0}. \\
\text{3 species: } \tilde{y} = 0: \quad & \frac{\partial \tilde{c}^+}{\partial \tilde{y}} = 0, \quad \tilde{J}_y^- = \tilde{J}_y^{ink} = 0, \quad \tilde{\Psi} = -750 \text{ V}, \quad \tilde{\vec{u}} = \vec{0}, \\
\tilde{y} = H: \quad & \tilde{J}_y^+ = 0, \quad \frac{\partial \tilde{c}^-}{\partial \tilde{y}} = \frac{\partial \tilde{c}^{ink}}{\partial \tilde{y}} = 0, \quad \tilde{\Psi} = 750 \text{ V}, \quad \tilde{\vec{u}} = \vec{0},
\end{aligned} \tag{143}$$

with periodic BCs employed in the  $x$  direction. The ICs within the computational domain are:

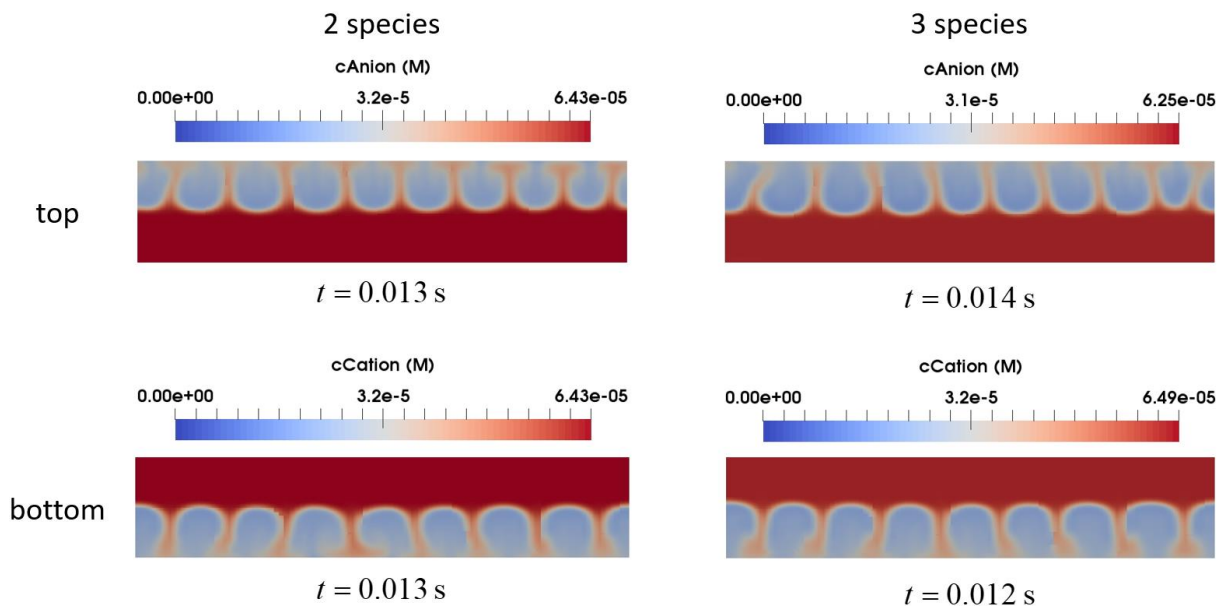
$$\begin{aligned}
\text{2 species: } \quad & c_0^+ = c_0^- = 6.43 \cdot 10^{-5} \frac{\text{mol}}{\text{m}^3}, \quad \Psi = 0, \quad \vec{u} = \vec{0}. \\
\text{3 species: } \quad & c_0^+ = 6.43 \cdot 10^{-5} \frac{\text{mol}}{\text{m}^3}, \quad c_0^- = 6.01 \cdot 10^{-5} \frac{\text{mol}}{\text{m}^3}, \quad c_0^{ink} = 1.137 \cdot 10^{-9} \frac{\text{mol}}{\text{m}^3}, \\
& \Psi = 0, \quad \vec{u} = \vec{0}.
\end{aligned} \tag{144}$$

Figure 38 demonstrates the convective cells containing VP that are developed in the vicinity of the top and bottom electrodes and appear a short time after the ECI onset of the 2D simulations. The anion concentration field is shown in the vicinity of the top electrode, while the cation concentration field is shown in the vicinity of the bottom electrode.



**Figure 37: Geometry dimensions and mesh details of QoM simulations: (a) 2D; (b) 3D.**

Considering the 3D geometry and mesh demonstrated in figure 37(b), two simulations were executed addressing the different electrolytes. The set of dimensioned governing equations (26,34-36) is solved with the BCs and ICs presented in equations (143-144), respectively, where periodic BCs were employed in the  $x$  and  $z$  directions. Figure 39 demonstrates the spatial convective cells that are developed on the top and bottom electrodes and appear a short time after the ECI onset of the 3D simulations. The anion concentration field is shown in the top view, while the cation concentration field is shown in the bottom view.



**Figure 38: Concentration fields of cation and anion species in the vicinity of the bottom and top QoM electrodes, respectively, a short time after the ECI onset. The convective cells containing VP are related to 2D rheoTool simulations.**

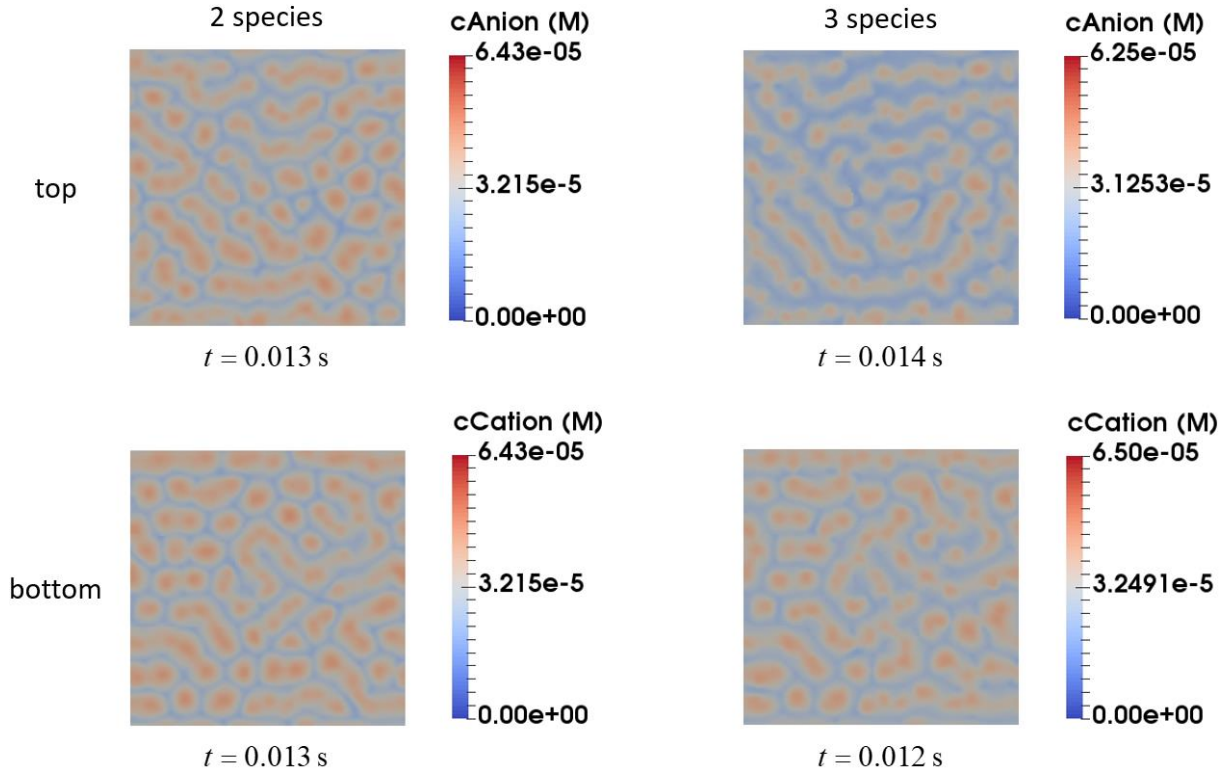


**Figure 39: Concentration fields of cation and anion species on the bottom and top QoM electrodes, respectively, a short time after the ECI onset. The spatial concentration patterns are related to 3D rheoTool simulations.**

As expected from the simulation results of the symmetric binary electrolyte, the onset time of ECI is equal for both cation (bottom electrode) and anion (top electrode) species. As explained in section 7.3 for the 3 species electrolyte, convective cells are first generated in the vicinity of the bottom electrode as a result of the wider ESC region in the vicinity of the bottom electrode. The dimensioned wave numbers of both the bottom and top VP demonstrated in figure 38 were calculated by:

$$\tilde{k} = \frac{N_{VP}}{2L}. \quad (145)$$

Remarkably, for the case of spatial convective cells appearing close to the top and bottom boundaries of the 3D simulations (see figure 39) two different wave numbers were estimated with respect to  $x$  and  $z$  directions. The estimation was performed by counting the concentration peaks along 10 parallel and equally spaced sections taken in the  $x$  and  $z$  directions. The number of concentration peaks was averaged over 10 sections in each direction, and then over 5 successive time instances starting shortly after ECI onset. Table 8 summarizes the wave numbers corresponding to the different configurations and electrolytes.

**Table 8: Wave numbers of vortex pairs addressing 2D and 3D rheoTool simulations of 2 or 3 species electrolytes. Results are related to a short time after the ECI onset while  $\tilde{k}_x$  and  $\tilde{k}_z$  are wave numbers in the  $x$  and  $z$  directions, respectively.**

Wave number (vortex pairs per mm)		2 species		3 species	
2D	top	30		30	
	bottom	26.67		26.67	
3D	top	$\tilde{k}_x$	25.67	$\tilde{k}_x$	25
		$\tilde{k}_z$	25.67	$\tilde{k}_z$	26
	bottom	$\tilde{k}_x$	25	$\tilde{k}_x$	25
		$\tilde{k}_z$	26.67	$\tilde{k}_z$	26.67

As can be seen from table 8, there are minor differences between the wave numbers corresponding to the two considered electrolytes. As expected,  $\tilde{k}_x$  and  $\tilde{k}_z$  values of the 3D configuration are quite similar due to the symmetric geometry and BCs utilized. Table 8 shows that the wave number values obtained by the 3D configuration are a bit lower than those obtained by the 2D configuration, although the differences are not significant.

#### 8.4 BID Simulations

This section summarizes the simulation results addressing the BID unit (figure 5), focusing mainly on the ME-DR gap (figure 6). Considering a rectangular domain of height  $H = r_2 - r_1 = 350 \mu\text{m}$  and  $AR = 5$ , filled by a symmetric binary electrolyte consisting of positively charged cations and negatively charged anions, the effect of an upper moving boundary is next examined. Figure 40 compares the anion concentration field obtained by either a stationary or a moving upper wall, for different representative time instances. The mixture and species properties considered are described in section 8.1. The mesh considered has 710 uniformly spaced cells in the  $x$  direction and 142 non-uniformly spaced cells in the  $y$  direction. The time step utilized is  $\Delta t = 10^{-5}$  s. The set of dimensioned governing equations (26,34-36) is solved with the BCs:

$$\begin{aligned} \tilde{y} = 0: \quad \frac{\partial \tilde{c}^+}{\partial \tilde{y}} = 0, \quad \tilde{J}_y^- = 0, \quad \tilde{\Psi} = -500 \text{ V}, \quad \tilde{u} = \vec{0}, \\ \tilde{y} = H: \quad \tilde{J}_y^+ = 0, \quad \frac{\partial \tilde{c}^-}{\partial \tilde{y}} = 0, \quad \tilde{\Psi} = 500 \text{ V}, \quad \tilde{u} = \vec{0} \text{ or } u_{\text{wall}} \hat{x}, \end{aligned} \quad (146)$$

with periodic BCs employed in the  $x$  direction. The ICs within the computational domain are:

$$c_0^+ = c_0^- = 6.43 \cdot 10^{-5} \frac{\text{mol}}{\text{m}^3}, \quad \Psi = 0, \quad \vec{u} = \vec{0}. \quad (147)$$

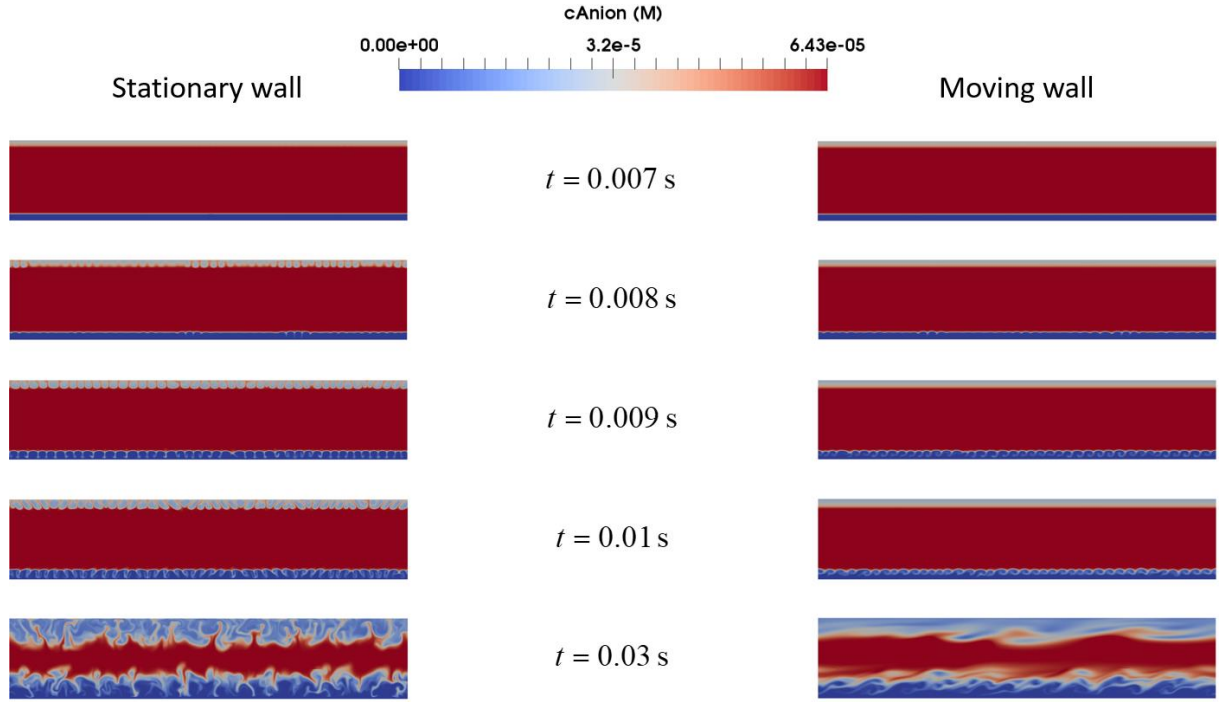


**Figure 40: The effect of moving boundary on ECI.**

In the case of stationary boundaries, Rubinstein-Zaltzman convective cells are generated simultaneously in the vicinity of both top and bottom boundaries, due to symmetry considerations. For the case of a moving top boundary, the instability convective cells are first generated in the vicinity of the stationary bottom boundary, simultaneously with the stationary configuration. However, the shear flow and momentum diffusion delay the onset of instability phenomena in the vicinity of the moving top boundary and render its patterns to be wavy rather than convective cell shapes. Figures 41-42 show the current density as a function of time for the stationary and moving boundary configurations as calculated by equation (41). Both curves are similar up to the ECI onset time. A magnification of figure 42 demonstrates the characteristic pattern of each instability with respect to the time evolution of the corresponding current density. As can be seen, the beginning of wavy behavior of the mixture flow in the moving boundary configuration can be clearly recognized by a significant peak observed in the time evolution of



the current density curve. The integral over time values of both current density curves are displayed in figure 41; these are equivalent to the number of charges leaving the computational domain through its top and bottom boundaries during the time, and deviate by about 7%.

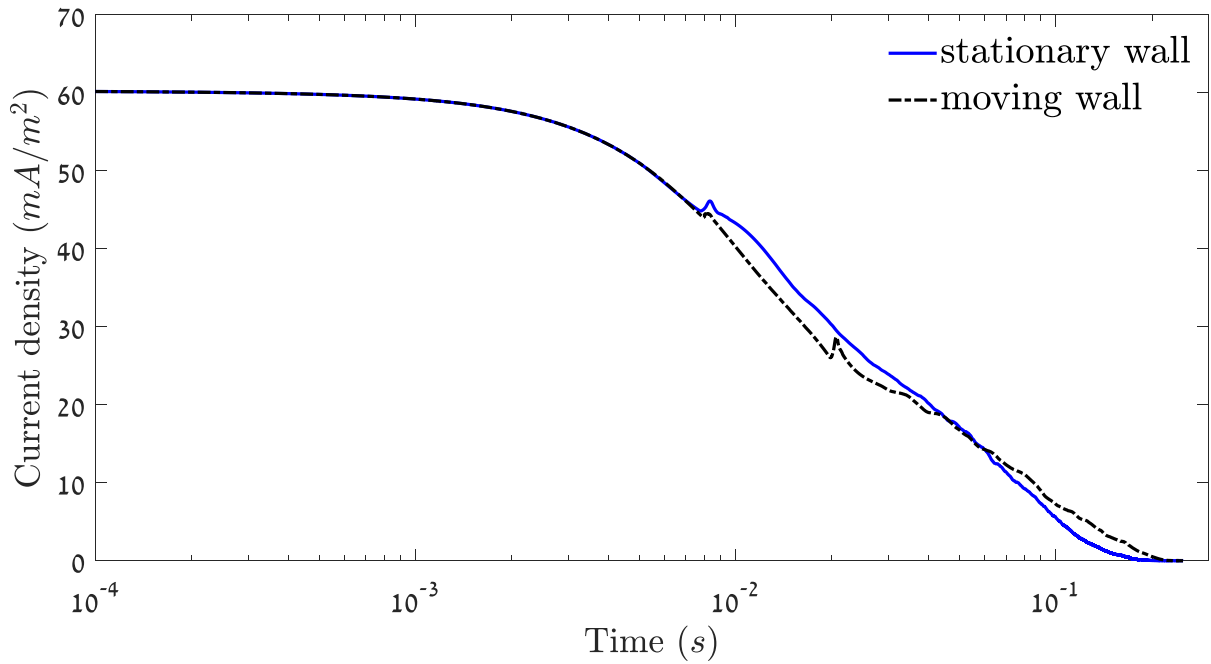


Figure 41: Current density as a function of time for stationary and moving top boundary configurations.

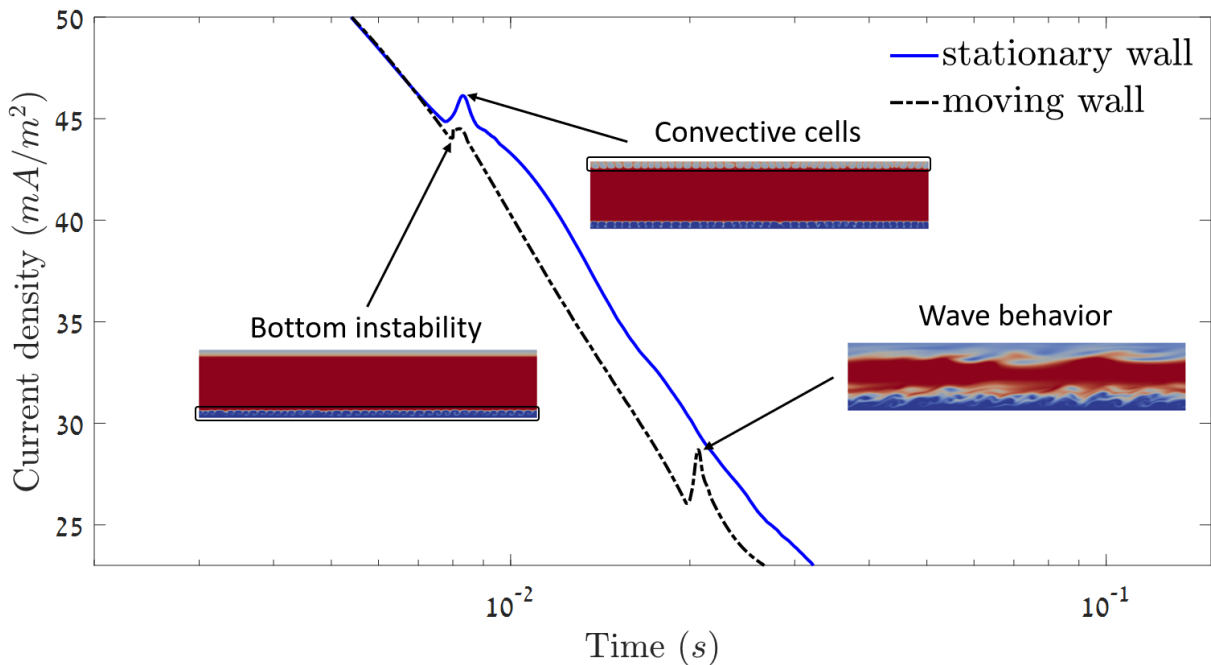


Figure 42: Magnification of figure 41. Instability patterns superimposed with the corresponding time evolution of electric current density.

The above-mentioned rectangular computational domain was extruded by 350  $\mu\text{m}$  along the  $z$  direction, to simulate 3D geometry. In this case, the mesh in the  $x$  and  $y$  directions is similar to the mesh previously used in 2D geometry, whereas in the  $z$  direction it was discretized by 60 equally spaced cells. The simulations were performed for a non-symmetric electrolyte consisting of cation, anion, and ink species, with the properties given in section 8.1. The time step utilized was  $\Delta t = 10^{-5}$  s. The set of dimensioned governing equations (26,34-36) is solved with the BCs:

$$\begin{aligned} \tilde{y} = 0: \quad \frac{\partial \tilde{c}^+}{\partial \tilde{y}} = 0, \quad \tilde{J}_y^- = \tilde{J}_y^{ink} = 0, \quad \tilde{\Psi} = -500 \text{ V}, \quad \tilde{u} = \vec{0}, \\ \tilde{y} = H: \quad \tilde{J}_y^+ = 0, \quad \frac{\partial \tilde{c}^-}{\partial \tilde{y}} = \frac{\partial \tilde{c}^{ink}}{\partial \tilde{y}} = 0, \quad \tilde{\Psi} = 500 \text{ V}, \quad \tilde{u} = u_{wall} \hat{x}, \end{aligned} \quad (148)$$

with periodic BCs employed in the  $x$  direction. The ICs within the computational domain are:

$$c_0^+ = 6.43 \cdot 10^{-5} \frac{\text{mol}}{\text{m}^3}, \quad c_0^- = 6.01 \cdot 10^{-5} \frac{\text{mol}}{\text{m}^3}, \quad c_0^{ink} = 1.137 \cdot 10^{-9} \frac{\text{mol}}{\text{m}^3}, \quad \Psi = 0, \quad \vec{u} = \vec{0}. \quad (149)$$

Figures 43-44 show the 3D concentration fields of anion and ink species, right after the onset of ECI.

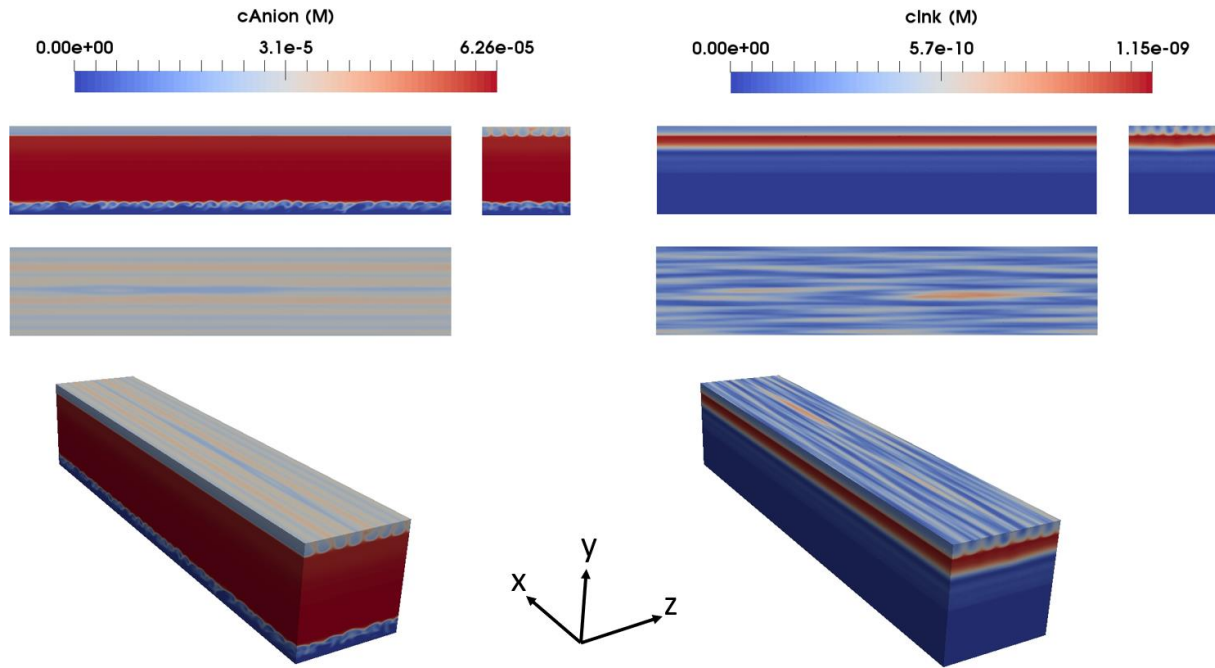


**Figure 43: Isometric view and front, side, and top views of the concentration fields a short time after the ECI onset,  $t=0.01$  s. Left: anion concentration. Right: ink concentration.**

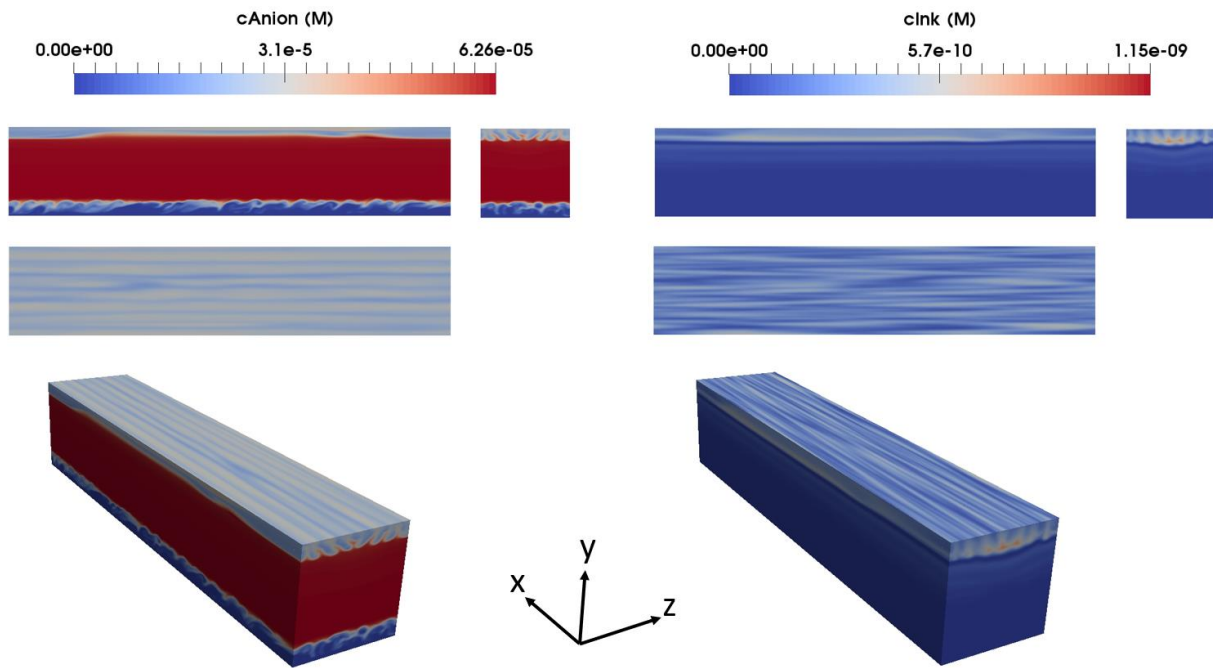


**Figure 44: Isometric view and front, side, and top views of the concentration fields a short time after the ECI onset,  $t=0.012$  s. Left: anion concentration. Right: ink concentration.**

Several insights are obtained by looking at figures 43-44. As expected, the transport of the ink species is more rapid compared with that of the anion species, as a result of the ink's higher electrical mobility. As follows from the front view, the instability onsets in the vicinity of the stationary bottom boundary. After a short time, wavy concentration patterns are exhibited in the vicinity of the top moving wall. Considering the side view, there is no velocity component of the top boundary in the  $z$  direction suppressing the VP. Thus, the ECI in the  $y$ - $z$  plane is exhibited by a series of convective cells simultaneously developing in the vicinity of both top and bottom boundaries. Additionally, the observed convective cells result in developing concentration streaks on the top boundary, as can be recognized by looking at the top view. This behavior of the ECI in the 3D configuration is similar to that observed for 2D simulations presented in figure 40. For this reason, the mechanism driving the ECI in 3D geometry can be qualitatively approximated as a superposition of two independent 2D ECI mechanisms: the first governing the ECI in the  $x$ - $y$  plane with the moving top boundary (front view) and the second governing the ECI in the  $y$ - $z$  plane with all stationary boundaries (side view). The development of concentration streaks on the top boundary has a significant impact on the printing quality of HP Indigo's printers.

## 9. Summary and Conclusions

In this work, the EHD transport of positively charged cations and negatively charged anions, in addition to negatively charged ink particles of high valence, was studied. All the species were placed within an oil medium and subjected to high voltage. An extensive literature review was conducted by surveying three numerical methodologies addressing multiphase flows, three EDF models, and the literature related to physical phenomena typical of a bounded electrolyte subjected to an electrical voltage. A comprehensive physical model coupling the electrostatic and the hydrodynamic phenomena was developed. The model includes a mathematical formulation of the governing conservation equations, constitutive laws, and estimation of the current density value. An extensive dimensional analysis was performed regarding both stationary and moving top boundary configurations. A comprehensive numerical methodology capable of addressing the above multi-physics phenomena was developed utilizing standard techniques of CFD. A simplified physical model was simulated by the Fluent package, comparing analytical solutions with numerical results. Next, the developed fully (two-way) coupled physical model was simulated by open source rheoTool software, based on the popular openFOAM package. Two Matlab scripts simulating 1D transient and steady state ionic transport by the solution of PNP equations were developed as well for verification purposes. The rheoEFoam solver was next extensively verified and utilized for gaining further understanding of the physical phenomena governing the behavior of a strongly non-symmetric electrolyte, and compared with its symmetric counterpart. Additionally, the above-mentioned CFD package has been adapted to simulate Indigo's QoM device. The numerical results were compared and calibrated by utilizing the QoM experimental results. Other 1D, 2D, and 3D simulations relating to the BID unit were executed and post-processed according to Indigo's data. Finally, the CFD model was provided to the HP Indigo company with the aim of further understanding the fundamental mechanism governing the EDF in the BID unit and improving the quality of printing.

## 9.1 Conclusions

General conclusions:

- The electric field distribution within an electrolytic cell is highly affected and screened by the concentration distribution of the charged species within the electrolyte. Thus, the solution of the simplified physical model that considers an approximation of only a constant external electric field may introduce non-negligible imprecisions.
- A zero gradient BC applied to the concentration field enables the exit and entry of species concentrations through the boundary by the electromigration mechanism. In contrast, the zero ionic flux BC does not allow the transport of species concentrations through the boundary. However, for high voltage values, applying this BC at the boundary attracting the charged species results in a non-limited accumulation of species concentration in the vicinity of this boundary, which, in turn, leads to the divergence of the numerical scheme. In order to deal with this difficulty, an additional term accounting for steric effects (molecular packing) is required to modify the Nernst-Planck equation.
- The initial electric current density value obtained for a symmetric binary electrolyte is lower than the initial electric current density value obtained for a strongly non-symmetric electrolyte consisting of 3 charged species and having the same initial amount of positive and negative charges. The current density may be calculated across any plane parallel to the electrodes and placed at  $0 < y_0 < 1$ .
- For the strongly non-symmetric electrolyte mentioned in chapter 7, each of the 3 charged species has a different propagation rate. The propagation rate value of the  $i = 3$  species is larger than that of the two other species due to its higher electrical mobility. The difference in propagation rate between the  $i = 2$  and  $i = 3$  species results in the exclusive "zone 2" where the  $i = 1$  and  $i = 2$  species adjust themselves differently compared to the DL in order to preserve the electrolyte electroneutrality (except for the back front of the  $i = 3$  species that is consistently with a spike in the  $\rho_E$  field).
- Up to the ECI onset time, both the concentration and electric potential distributions, and the transient evolution of the electric current density are similar for both 1D and 2D simulations. Up to the ECI onset time, the interface and the propagation of the interface between the ESC and DL regions resemble those typical of a shock wave. Non-uniformity of the interface and a corresponding peak in the transient current density curve indicate the ECI onset.
- For the strongly non-symmetric electrolyte mentioned in chapter 7, three ESC regions correspond to the three different charged species. The ECI first onsets in the vicinity of the bottom (negatively charged) electrode and then in the vicinity of the top (positively charged) electrode. A secondary ECI associated with the  $i = 3$  species may appear in zone 2.

- A moving boundary suppresses the ECI onset in its vicinity. In this case, the most significant spike in the transient current density curve corresponds to a wavy shape of the ESC-DL interface in the vicinity of the moving boundary.
- A higher  $\epsilon$  value results in a weaker screening effect, in a higher propagation rate of the charged species, in a larger value of the ECI onset time, in a bigger size of VP, and in a lower value of the wave number.
- A higher  $c_r$  value results in a lower propagation rate of the  $i = 1$  and  $i = 3$  species, in a higher propagation rate of the  $i = 2$  species, in a higher value of the initial current density, in a lower value of the ECI onset time, in a higher  $\tau$  value (see equation (90)), and in a larger difference between the high wave number in the vicinity of the top electrode and the low wave number in the vicinity of the bottom electrode.

Conclusions related to HP Indigo's private case:

- The mixture method is suitable for the numerical solution of the problem. The assumption of non-inertial ink particles is well justified.
- The range of voltage values supplied to HP QoM electrodes or to the ME-DR boundaries is well associated with the overlimiting regime (see figure 8).
- In the case of QoM simulation, the inertial term of the NS equation (34) can be neglected. The fluid flow is mainly dominated by the electric body force term while the ink transport is mainly dominated by the electromigration term (see (125)).
- The values of spatial  $\tilde{k}_x$  and  $\tilde{k}_z$  wave numbers obtained by the 3D QoM simulation are quite a bit smaller than the values of the wave number obtained by the corresponding 2D simulations.
- According to the comparison between QoM experimental and numerical results, several mixture and species property values given by HP Indigo are incorrect. The values characterized by the highest uncertainty are the oil viscosity, species diameter and electrical mobility, and the percentage of effective micelles.
- The fluid flow in the ME-DR gap is mainly dominated by the inertial and pressure gradient terms, while the species transport is mainly dominated by the advective term (see (131)). However, the mixture flow within this gap is not turbulent.
- The qualitative characteristics of 3D BID simulation may be understood by approximating them as a superposition of two 2D simulations: the first is a 2D simulation in the x-y plane with a moving top boundary and the second is a 2D simulation in the y-z plane with all stationary boundaries. The ECI developed in the y-z plane in the vicinity of the top DR boundary results in nonuniform streaks of ink concentration on the DR surface, which has a significant effect on the printing quality.

## 9.2 Future Work

The following comprises recommendations for possible extensions of the present study:

- Calibrating the values of the most uncertain parameters (oil viscosity, species electrical mobility, percentage of effective micelles) against QoM experiments and simulation results.
- Implementing the zero ionic flux BC for the anion and ink species on the top DR boundary by utilizing an additional term in the Nernst-Planck equation (36) addressing the steric effects (molecular packing).
- Correlating the mixture viscosity with the ink mass fraction. Correlating the species electrical mobility with the value of the electric field.
- Executing 2D and 3D simulations of the whole ME-DR curved geometry, applying inlet velocity and outlet pressure BCs. Executing 2D and 3D simulations for the BE-DR and neck regions of the BID.
- Applying spatio-temporal alternating electric potential BCs on both top and bottom boundaries as a possible mechanism of suppressing the ECI patterns (streaks).

## Bibliography

- [1] Hagayev, Michael, (2018) "Two-phase modeling of charged particles in an electric field", 4<sup>th</sup> year final project, 18-108, The Department of Mechanical Engineering, Ben-Gurion University of the Negev.
- [2] Luo, Kang, et al. "Efficient lattice Boltzmann method for electrohydrodynamic solid-liquid phase change." *Physical Review E* 100.1 (2019): 013306.
- [3] Kourmatzis, Agisilaos, and John S. Shrimpton. "Characteristics of electrohydrodynamic roll structures in laminar planar Couette flow." *Journal of Physics D: Applied Physics* 49.4 (2015): 045503.
- [4] Bandopadhyay, Aditya, and Uddipta Ghosh. "Electrohydrodynamic Phenomena." *Journal of the Indian Institute of Science* 98.2 (2018): 201-225.
- [5] Wang, Chao, et al. "Modeling electrokinetics in ionic liquids." *Electrophoresis* 38.13-14 (2017): 1693-1705.
- [6] Bahga, Supreet S., Moran Bercovici, and Juan G. Santiago. "Robust and high-resolution simulations of nonlinear electrokinetic processes in variable cross-section channels." *Electrophoresis* 33.19-20 (2012): 3036-3051.
- [7] Flores-Rivera, Ciro-Filemon. "Modeling and Behavior Analysis of a Membraneless Fuel Cell." *International Scholarly Research Notices* 2012 (2012).
- [8] Pimenta, Francisco, and Manuel A. Alves. "Numerical simulation of electrically-driven flows using OpenFOAM." *arXiv preprint arXiv: 1802.02843* (2018).
- [9] Forgacs, Peter, and Albert Teishev. "Electro-Rheological Model of HP Indigo ElectroInk." *Journal of Imaging Science and Technology* 57.3 (2013): 30403-1.
- [10] Adobe Spark Page, "Understanding the HP Indigo 5000".
- [11] HP Indigo, (2012), "HP Indigo Digital Offset Colour Technology".
- [12] Tagansky, Boaz. "HP-Indigo Technology and its Application to Photo Printing." *International Symposium on Technologies for Digital Photo Fulfillment*. Vol. 2012. No. 1. Society for Imaging Science and Technology, 2012.
- [13] Tagansky, Boaz. "Ink development in HP Indigo digital presses." *NIP & Digital Fabrication Conference*. Vol. 2008. No. 2. Society for Imaging Science and Technology, 2008.
- [14] Gidaspow, Dimitri. *Multiphase Flow and Fluidization: Continuum and Kinetic Theory Descriptions*. Elsevier, 2012: 1-60.
- [15] Schmid, Hans-Joachim, and Lutz Vogel. "On the modelling of the particle dynamics in electro-hydrodynamic flow-fields: I. Comparison of Eulerian and Lagrangian modelling approach." *Powder Technology* 135 (2003): 118-135.
- [16] Johnson, Richard W., ed. *Handbook of Fluid Dynamics*. CRC Press, 1998.: 4-18.
- [17] Ansys Fluent guidebook, version 16.2, 2016, "Species Transport Equations", chapter 7.1.1.



- [18] Chen, Wei, Ying Ren, and Lifeng Zhang. "Large eddy simulation on the two-phase flow in a water model of continuous casting strand with gas injection." *steel research international* 90.4 (2019): 1800287.
- [19] Spandan, Vamsi, et al. "Drag reduction in numerical two-phase Taylor–Couette turbulence using an Euler–Lagrange approach." *Journal of fluid mechanics* 798 (2016): 411-435.
- [20] Price, Matthew A., et al. "An Euler–Lagrange particle approach for modeling fragments accelerated by explosive detonation." *International Journal for Numerical Methods in Engineering* 106.11 (2016): 904-926.
- [21] Blais, Bruno, et al. "CFD-DEM simulations of early turbulent solid–liquid mixing: Prediction of suspension curve and just-suspended speed." *Chemical Engineering Research and Design* 123 (2017): 388-406.
- [22] Fontes, Douglas Hector, et al. "Improved hybrid model applied to liquid jet in crossflow." *International Journal of Multiphase Flow* 114 (2019): 98-114.
- [23] Sardina, Gaetano, et al. "Assessing the ability of the Eulerian-Eulerian and the Eulerian-Lagrangian frameworks to capture meso-scale dynamics in bubbly flows." *Chemical engineering science* 201 (2019): 58-73.
- [24] Du, Shaohua, and Lijun Liu. "A local cluster-structure-dependent drag model for Eulerian simulation of gas-solid flow in CFB risers." *Chemical Engineering Journal* 368 (2019): 687-699.
- [25] Li, Yong, Jianping Zhang, and Liang-Shih Fan. "Numerical simulation of gas–liquid–solid fluidization systems using a combined CFD-VOF-DPM method: bubble wake behavior." *Chemical Engineering Science* 54.21 (1999): 5101-5107.
- [26] Li, Yubai, et al. "The effects of particle concentration and various fluxes on the flow of a fluid-solid suspension." *Applied Mathematics and Computation* 358 (2019): 151-160.
- [27] d'Auzay, Charles Turquand, et al. "Statistics of progress variable and mixture fraction gradients in an open turbulent jet spray flame." *Fuel* 247 (2019): 198-208.
- [28] RheoTool user guide, version 3, 2018, "Electrically-driven flow models", chapter 3.6.
- [29] Shi, Dongyang, and Huaijun Yang. "Superconvergence analysis of finite element method for Poisson–Nernst–Planck equations." *Numerical Methods for Partial Differential Equations* 35.3 (2019): 1206-1223.
- [30] Sprocati, Riccardo, et al. "Modeling electrokinetic transport and biogeochemical reactions in porous media: A multidimensional Nernst–Planck–Poisson approach with PHREEQC coupling." *Advances in water resources* 127 (2019): 134-147.
- [31] Liu, Rui, et al. "Pore-scale study of dynamic ion adsorption process in porous electrodes of capacitive deionization using lattice Boltzmann method." *International Journal of Heat and Mass Transfer* 135 (2019): 769-781.
- [32] Li, Jiao, Jinyong Ying, and Dexuan Xie. "On the analysis and application of an ion size-modified Poisson–Boltzmann equation." *Nonlinear Analysis: Real World Applications* 47 (2019): 188-203.

- [33] Wang, Qiming, Manman Ma, and Michael Siegel. "Deformation and stability of a viscous electrolyte drop in a uniform electric field." *Physical Review Fluids* 4.5 (2019): 053702.
- [34] Robinson, A. P. L. "Nonlinear screening in moderate-Z hot dense matter." *Plasma Physics and Controlled Fusion* 61.6 (2019): 065013.
- [35] Druzgalski, C. L., M. B. Andersen, and A. Mani. "Direct numerical simulation of electroconvective instability and hydrodynamic chaos near an ion-selective surface." *Physics of Fluids* 25.11 (2013): 110804.
- [36] Dukhin, Stanislav S. "Electrokinetic phenomena of the second kind and their applications." *Advances in colloid and interface science* 35 (1991): 173-196.
- [37] Zholkovskij, Emilij K., Michail A. Vorotyntsev, and Eberhard Staude. "Electrokinetic instability of solution in a plane-parallel electrochemical cell." *Journal of colloid and interface science* 181.1 (1996): 28-33.
- [38] Squires, Todd M., and Martin Z. Bazant. "Induced-charge electro-osmosis." arXiv preprint physics/0304090 (2003).
- [39] Rubinstein, Isaak, Boris Zaltzman, and Irina Lerman. "Electroconvective instability in concentration polarization and nonequilibrium electro-osmotic slip." *Physical review E* 72.1 (2005): 011505.
- [40] Pundik, Tamara, Isaak Rubinstein, and Boris Zaltzman. "Bulk electroconvection in electrolyte." *Physical Review E* 72.6 (2005): 061502.
- [41] Zaltzman, Boris, and Isaak Rubinstein. "Electro-osmotic slip and electroconvective instability." *Journal of Fluid Mechanics* 579 (2007): 173.
- [42] Druzgalski, Clara, and Ali Mani. "Statistical analysis of electroconvection near an ion-selective membrane in the highly chaotic regime." *Physical Review Fluids* 1.7 (2016): 073601.
- [43] Buck, Richard P. "Steady-state space charge effects in symmetric cells with concentration polarized electrodes." *Journal of Electroanalytical Chemistry and Interfacial Electrochemistry* 46.1 (1973): 1-23.
- [44] Rubinstein, Isaak, and Boris Zaltzman. "Electro-osmotically induced convection at a permselective membrane." *Physical Review E* 62.2 (2000): 2238.
- [45] Rubinstein, Isaak, and Boris Zaltzman. "Wave number selection in a nonequilibrium electro-osmotic instability." *Physical Review E* 68.3 (2003): 032501.
- [46] Mishchuk, Nataliya A. "Concentration polarization of interface and non-linear electrokinetic phenomena." *Advances in Colloid and Interface Science* 160.1-2 (2010): 16-39.
- [47] Nikonenko, Victor V., et al. "Desalination at overlimiting currents: State-of-the-art and perspectives." *Desalination* 342 (2014): 85-106.
- [48] Abu-Rjal, Ramadan, et al. "Equilibrium electro-convective instability in concentration polarization: The effect of non-equal ionic diffusivities and longitudinal flow." *Russian Journal of Electrochemistry* 53.9 (2017): 903-918.

- [49] Mani, Ali, and Karen May Wang. "Electroconvection Near Electrochemical Interfaces: Experiments, Modeling, and Computation." *Annual Review of Fluid Mechanics* 52 (2020): 509-529.
- [50] Kim, Jeonglae, Scott Davidson, and Ali Mani. "Characterization of chaotic electroconvection near flat inert electrodes under oscillatory voltages." *Micromachines* 10.3 (2019): 161.
- [51] Abu-Rjal, R., et al. "Signature of electroconvective instability in transient galvanostatic and potentiostatic modes in a microchannel-nanoslot device." *Physical Review Fluids* 4.8 (2019): 084203.
- [52] Probstein, Ronald F. *Physicochemical hydrodynamics: an introduction*. John Wiley & Sons, 2005.
- [53] Khair, Aditya S. "Concentration polarization and second-kind electrokinetic instability at an ion-selective surface admitting normal flow." *Physics of Fluids* 23.7 (2011): 072003.
- [54] Dydek, E. Victoria, et al. "Overlimiting current in a microchannel." *Physical review letters* 107.11 (2011): 118301.
- [55] Davidson, Scott M., Mathias B. Andersen, and Ali Mani. "Chaotic induced-charge electro-osmosis." *Physical review letters* 112.12 (2014): 128302.
- [56] Demekhin, E. A., N. V. Nikitin, and V. S. Shelistov. "Direct numerical simulation of electrokinetic instability and transition to chaotic motion." *Physics of Fluids* 25.12 (2013): 122001.
- [57] Shi, Pengpeng, and Wei Liu. "Length-dependent instability of shear electroconvective flow: From electroconvective instability to Rayleigh-B'nard instability." *Journal of Applied Physics* 124.20 (2018): 204304.
- [58] Mishchuk, N., and P. Takhistov. "Electroosmosis of the second kind and current through curved interface." *Colloids and Surfaces A: Physicochemical and Engineering Aspects* 181.1-3 (2001): 131-144.
- [59] Rubinstein, Shmuel M., et al. "Direct observation of a nonequilibrium electro-osmotic instability." *Physical review letters* 101.23 (2008): 236101.
- [60] Demekhin, E. A., G. S. Ganchenko, and E. N. Kalaydin. "Transition to electrokinetic instability near imperfect charge-selective membranes." *Physics of Fluids* 30.8 (2018): 082006.
- [61] Demekhin, E. A., N. V. Nikitin, and V. S. Shelistov. "Three-dimensional coherent structures of electrokinetic instability." *Physical Review E* 90.1 (2014): 013031.
- [62] Karatay, Elif, Clara L. Druzgalski, and Ali Mani. "Simulation of chaotic electrokinetic transport: Performance of commercial software versus custom-built direct numerical simulation codes." *Journal of colloid and interface science* 446 (2015): 67-76.
- [63] Andersen, Mathias B., et al. "Confinement effects on electroconvective instability." *Electrophoresis* 38.5 (2017): 702-711.

- [64] Rubinstein, I., and B. Zaltzman. "Equilibrium electroconvective instability." *Physical review letters* 114.11 (2015): 114502.
- [65] Abu-Rjal, Ramadan, Isaak Rubinstein, and Boris Zaltzman. "Driving factors of electroconvective instability in concentration polarization." *Physical Review Fluids* 1.2 (2016): 023601.
- [66] Rubinstein, I., and B. Zaltzman. "Equilibrium electro-osmotic instability in concentration polarization at a perfectly charge-selective interface." *Physical Review Fluids* 2.9 (2017): 093702.
- [67] Green, Michael Enoch, and Masao Yafuso. "Noise spectra associated with hydrochloric acid transport through some cation-exchange membranes." *The Journal of Physical Chemistry* 75.5 (1971): 654-662.
- [68] Stern, Stephen H., and Michael E. Green. "Noise generated during sodium and hydrogen ion transport across a cation exchange membrane." *The Journal of Physical Chemistry* 77.12 (1973): 1567-1572.
- [69] Fang, Yifei, Qinglin Li, and Michael E. Green. "Noise spectra of transport at an anion membrane-solution interface." *Journal of Colloid and Interface Science* 86.1 (1982): 185-190.
- [70] Rubinstein, I., E. Staude, and O. Kedem. "Role of the membrane surface in concentration polarization at ion-exchange membrane." *Desalination* 69.2 (1988): 101-114.
- [71] Maletzki, F., H-W. Rösler, and E. Staude. "Ion transfer across electrodialysis membranes in the overlimiting current range: stationary voltage current characteristics and current noise power spectra under different conditions of free convection." *Journal of membrane science* 71.1-2 (1992): 105-116.
- [72] Peskir, Goran. "On the diffusion coefficient: The Einstein relation and beyond." (2003): 383-405.
- [73] Gagnon, Frédérick, Donald Ziegler, and Mario Fafard. "Electrochemical modelling using electroneutrality equation as a constraint." *Journal of Applied Electrochemistry* 44.3 (2014): 361-381.
- [74] Manzanares, J. A., et al. "Numerical simulation of the nonequilibrium diffuse double layer in ion-exchange membranes." *The Journal of Physical Chemistry* 97.32 (1993): 8524-8530.
- [75] Feicht, Sarah E., Alexandra E. Frankel, and Aditya S. Khair. "Discharging dynamics in an electrolytic cell." *Physical Review E* 94.1 (2016): 012601.
- [76] Yochelis, Arik. "Spatial structure of electrical diffuse layers in highly concentrated electrolytes: a modified Poisson–Nernst–Planck approach." *The Journal of Physical Chemistry C* 118.11 (2014): 5716-5724.
- [77] Flanagan, Michael Thomas. "Michael thomas flanagan's java scientific library - "Class GouyChapmanStern: Models the Gouy-Chapman and Gouy-Chapman-Stern Equations." (2007).

- [78] Chabay, Ruth W., and Bruce A. Sherwood. Matter and interactions. John Wiley & Sons, 2011, p. 923.
- [79] Weller, Henry G., et al. "A tensorial approach to computational continuum mechanics using object-oriented techniques." *Computers in physics* 12.6 (1998): 620-631.
- [80] Patankar, Suhas V., and D. Brian Spalding. "A calculation procedure for heat, mass and momentum transfer in three-dimensional parabolic flows." *Numerical prediction of flow, heat transfer, turbulence and combustion*. Pergamon, 1983. 54-73.
- [81] Green, Yoav, and Gilad Yossifon. "Dynamical trapping of colloids at the stagnation points of electro-osmotic vortices of the second kind." *Physical Review E* 87.3 (2013): 033005.
- [82] Shelistov, V. S., et al. "A sequence of electrokinetic-instability bifurcations resulting in a chaotic-flow regime." *Doklady Physics*. Vol. 59. No. 4. Pleiades Publishing, 2014.
- [83] Serway, A. Raymond. *Physics for scientist and engineers: with modern physics*. Saunders College Publishing, 1996, fourth edition, p. 687.

## Appendix A – Dimensional Analysis

### First Configuration

Dimensional mass conservation equation for incompressible flow (26):

$$\vec{\nabla} \cdot \tilde{\vec{u}} = 0. \quad (\text{I})$$

Substituting relations (42-43) into equation (I):

$$\begin{aligned} \frac{1}{l_0} \vec{\nabla} \cdot (u_0 \vec{u}) &= 0 \\ \vec{\nabla} \cdot \vec{u} &= 0. \end{aligned} \quad (\text{II})$$

Dimensional momentum conservation equation (34):

$$\rho \left( \frac{\partial \tilde{\vec{u}}}{\partial \tilde{t}} + \tilde{\vec{u}} \cdot \vec{\nabla} \tilde{\vec{u}} \right) = -\vec{\nabla} \tilde{P} + \eta \nabla^2 \tilde{\vec{u}} - F \left( \sum_{i=1}^n z_i \tilde{c}_i \right) \vec{\nabla} \tilde{\Psi}. \quad (\text{III})$$

Substituting relations (42-43) into equation (III):

$$\begin{aligned} \rho \left( \frac{\partial (u_0 \vec{u})}{\partial (t_0 t)} + u_0 \vec{u} \cdot \frac{1}{l_0} \vec{\nabla} (u_0 \vec{u}) \right) &= -\frac{1}{l_0} \vec{\nabla} (P_0 P) + \frac{\eta}{l_0^2} \nabla^2 (u_0 \vec{u}) - \frac{F}{l_0} \left( \sum_{i=1}^n z_i c_0^+ c_i \right) \vec{\nabla} (V_T \Psi) \\ \rho \left( \frac{\varepsilon}{\eta l_0} V_T^2 \frac{D^+}{l_0^2} \frac{\partial \vec{u}}{\partial t} + \frac{1}{l_0} \left( \frac{\varepsilon}{\eta l_0} V_T^2 \right)^2 \vec{u} \cdot \vec{\nabla} \vec{u} \right) &= \\ &= -\frac{\eta}{l_0^2} \frac{\varepsilon}{\eta l_0} V_T^2 \vec{\nabla} P + \frac{\eta}{l_0^2} \frac{\varepsilon}{\eta l_0} V_T^2 \nabla^2 \vec{u} - \frac{F c_0^+ V_T}{l_0} \left( \sum_{i=1}^n z_i c_i \right) \vec{\nabla} \Psi \quad /: \frac{\eta}{l_0^2} \frac{\varepsilon}{\eta l_0} V_T^2 \end{aligned} \quad (\text{IV})$$

$$\frac{\rho D^+}{\eta} \left( \frac{\partial \vec{u}}{\partial t} + \frac{\varepsilon}{\eta D^+} V_T^2 \vec{u} \cdot \vec{\nabla} \vec{u} \right) = -\vec{\nabla} P + \nabla^2 \vec{u} - \frac{F c_0^+ l_0^2}{\varepsilon V_T} \left( \sum_{i=1}^n z_i c_i \right) \vec{\nabla} \Psi$$

$$\frac{1}{Sc} \left( \frac{\partial \vec{u}}{\partial t} + Pe \vec{u} \cdot \vec{\nabla} \vec{u} \right) = -\vec{\nabla} P + \nabla^2 \vec{u} - \frac{1}{2 \varepsilon^2 z^+} \left( \sum_{i=1}^n z_i c_i \right) \vec{\nabla} \Psi$$

$$\frac{1}{Sc} \left( \frac{\partial \vec{u}}{\partial t} + Pe \vec{u} \cdot \vec{\nabla} \vec{u} \right) = -\vec{\nabla} P + \nabla^2 \vec{u} - \frac{1}{2 \varepsilon^2} \left( \sum_{i=1}^n z_{r_i} c_i \right) \vec{\nabla} \Psi.$$

Dimensional Poisson's equation for the electric potential (35):

$$\nabla^2 \tilde{\Psi} = -\frac{F}{\varepsilon} \left( \sum_{i=1}^n z_i \tilde{c}_i \right). \quad (\text{V})$$

Substituting relations (42-43) into equation (V):

$$\begin{aligned}\frac{1}{l_0^2} \nabla^2 (V_T \Psi) &= -\frac{F}{\varepsilon} \left( \sum_{i=1}^n z_i c_0^+ c_i \right) \\ -\frac{\varepsilon V_T}{l_0^2 F c_0^+ z^+} \nabla^2 \Psi &= \frac{1}{z^+} \left( \sum_{i=1}^n z_i c_i \right) \\ -2 \varepsilon^2 \nabla^2 \Psi &= \sum_{i=1}^n z_{r_i} c_i.\end{aligned}\quad (\text{VI})$$

Dimensional Nernst-Planck equation (20):

$$\frac{\partial \tilde{c}_i}{\partial \tilde{t}} = -\vec{\nabla} \cdot \tilde{\vec{J}}_i. \quad (\text{VII})$$

Substituting relations (42-43) into equation (VII):

$$\begin{aligned}\frac{\partial (c_0^+ c_i)}{\partial (t_0 t)} &= -\frac{1}{l_0} \vec{\nabla} \cdot (J_0 \vec{J}_i) \\ \frac{c_0^+ D^+}{l_0^2} \frac{\partial c_i}{\partial t} &= -\frac{c_0^+ D^+}{l_0^2} \vec{\nabla} \cdot \vec{J}_i \\ \frac{\partial c_i}{\partial t} &= -\vec{\nabla} \cdot \vec{J}_i.\end{aligned}\quad (\text{VIII})$$

Dimensional ionic flux of the  $i^{\text{th}}$  species for isothermal flow determined by equation (21):

$$\tilde{\vec{J}}_i = \tilde{c}_i \tilde{\vec{u}} - D_i \vec{\nabla} \tilde{c}_i - \left( D_i \frac{z_i e}{k_B T} \vec{\nabla} \tilde{\Psi} \right) \tilde{c}_i. \quad (\text{IX})$$

Substituting relations (42-43) into equation (IX):

$$\begin{aligned}J_0 \vec{J}_i &= c_0^+ c_i u_0 \vec{u} - \frac{D_i}{l_0} \vec{\nabla} (c_0^+ c_i) - \frac{D_i z_i V_T c_0^+}{l_0 V_T z^+} c_i \vec{\nabla} \Psi \\ \frac{c_0^+ D^+}{l_0} \vec{J}_i &= \frac{c_0^+ \varepsilon}{\eta l_0} V_T^2 c_i \vec{u} - \frac{c_0^+ D_i}{l_0} \vec{\nabla} c_i - \frac{D_i z_i c_0^+}{l_0 z^+} c_i \vec{\nabla} \Psi \\ \vec{J}_i &= Pec_i \vec{u} - D_{r_i} \vec{\nabla} c_i - D_{r_i} z_{r_i} c_i \vec{\nabla} \Psi.\end{aligned}\quad (\text{X})$$

Dimensional current density in the  $y$  direction determined in equation (41):

$$\tilde{I}_y = \left| \frac{1}{2L} \int_L \left[ F \left( \sum_{i=1}^n z_i (\tilde{J}_i)_y \right) - \varepsilon \frac{\partial^2 \tilde{\Psi}}{\partial \tilde{y} \partial \tilde{t}} \right] \Big|_{\tilde{x}, \tilde{y}=\tilde{y}_0, \tilde{t}} d\tilde{x} \right|. \quad (\text{XI})$$

Substituting relations (42-43) into equation (XI):

$$\begin{aligned}
I_0 I_y &= \left| \frac{1}{2L} \int_{2L} \left[ F \left( \sum_{i=1}^n z_i J_0 (J_i)_y \right) - \varepsilon \frac{\partial^2 (V_T \Psi)}{\partial (l_0 y) \partial (t_0 t)} \right] \right|_{l_0 x, l_0 y = l_0 y_0, t_0 t} d(l_0 x) \\
\frac{F z^+ c_0^+ D^+}{l_0} I_y &= \left| \frac{l_0}{2L_{AR}} \int_{AR} \left[ F \left( \sum_{i=1}^n z_i \frac{c_0^+ D^+}{l_0} (J_i)_y \right) - \frac{\varepsilon V_T D^+}{l_0^3} \frac{\partial^2 \Psi}{\partial y \partial t} \right] \right|_{x, y = y_0, t} dx \\
I_y &= \left| \frac{1}{AR} \int_{AR} \left[ \frac{1}{z^+} \left( \sum_{i=1}^n z_i (J_i)_y \right) - \frac{\varepsilon V_T}{l_0^2 F z^+ c_0^+} \frac{\partial^2 \Psi}{\partial y \partial t} \right] \right|_{x, y = y_0, t} dx \\
I_y &= \left| \frac{1}{AR} \int_{AR} \left[ \left( \sum_{i=1}^n z_{r_i} (J_i)_y \right) - 2 \varepsilon^2 \frac{\partial^2 \Psi}{\partial y \partial t} \right] \right|_{x, y = y_0, t} dx.
\end{aligned} \tag{XII}$$

## Second Configuration

Non-dimensional mass conservation equation for incompressible flow, Poisson's equation for the electric potential, Nernst-Planck equation for species concentration and the calculation for current density in the  $y$  direction remain the same as presented in equations (II, VI, VIII) and (XII), respectively.

Dimensional momentum conservation equation (34):

$$\rho \left( \frac{\partial \tilde{u}}{\partial \tilde{t}} + \tilde{u} \cdot \tilde{\nabla} \tilde{u} \right) = -\tilde{\nabla} \tilde{P} + \eta \nabla^2 \tilde{u} - F \left( \sum_{i=1}^n z_i \tilde{c}_i \right) \tilde{\nabla} \tilde{\Psi}. \tag{XIII}$$

Substituting relations (52,43) into equation (XIII):

$$\begin{aligned}
\rho \left( \frac{\partial (u_0 \bar{u})}{\partial (t_0 t)} + u_0 \bar{u} \cdot \frac{1}{l_0} \tilde{\nabla} (u_0 \bar{u}) \right) &= -\frac{1}{l_0} \tilde{\nabla} (P_0 P) + \frac{\eta}{l_0^2} \nabla^2 (u_0 \bar{u}) - \frac{F}{l_0} \left( \sum_{i=1}^n z_i c_0^+ c_i \right) \tilde{\nabla} (V_T \Psi) \\
\rho \left( \frac{u_0^2}{l_0} \frac{\partial \bar{u}}{\partial t} + \frac{u_0^2}{l_0} \bar{u} \cdot \tilde{\nabla} \bar{u} \right) &= -\frac{\rho u_0^2}{l_0} \tilde{\nabla} P + \frac{\eta u_0}{l_0^2} \nabla^2 \bar{u} - \frac{F c_0^+ V_T}{l_0} \left( \sum_{i=1}^n z_i c_i \right) \tilde{\nabla} \Psi \\
\frac{\partial \bar{u}}{\partial t} + \bar{u} \cdot \tilde{\nabla} \bar{u} &= -\tilde{\nabla} P + \frac{\eta}{\rho u_0 l_0} \nabla^2 \bar{u} - \frac{F c_0^+ V_T}{\rho u_0^2} \left( \sum_{i=1}^n z_i c_i \right) \tilde{\nabla} \Psi \\
\frac{\partial \bar{u}}{\partial t} + \bar{u} \cdot \tilde{\nabla} \bar{u} &= -\tilde{\nabla} P + \frac{1}{Re} \nabla^2 \bar{u} - \frac{\kappa}{2 \varepsilon^2 Re^2 Sc} \left( \sum_{i=1}^n z_i c_i \right) \tilde{\nabla} \Psi.
\end{aligned} \tag{XIV}$$



Dimensional ionic flux of the  $i^{th}$  species for isothermal flow determined by equation (21):

$$\tilde{\vec{J}}_i = \tilde{c}_i \tilde{\vec{u}} - D_i \vec{\nabla} \tilde{c}_i - \left( D_i \frac{z_i e}{k_B T} \vec{\nabla} \tilde{\Psi} \right) \tilde{c}_i. \quad (\text{XV})$$

Substituting relations (52,43) into equation (XV):

$$\begin{aligned} J_0 \vec{J}_i &= c_0^+ c_i u_0 \vec{u} - \frac{D_i}{l_0} \vec{\nabla} (c_0^+ c_i) - \frac{D_i z_i V_T c_0^+}{l_0 V_T z^+} c_i \vec{\nabla} \Psi \\ c_0^+ u_0 \vec{J}_i &= c_0^+ u_0 c_i \vec{u} - \frac{c_0^+ D_i}{l_0} \vec{\nabla} c_i - \frac{D_i z_i c_0^+}{l_0 z^+} c_i \vec{\nabla} \Psi \\ \vec{J}_i &= c_i \vec{u} - \frac{D_i}{l_0 u_0} \vec{\nabla} c_i - \frac{D_i z_i}{l_0 u_0 z^+} c_i \vec{\nabla} \Psi \\ \vec{J}_i &= c_i \vec{u} - \frac{D_i}{Re Sc} (\vec{\nabla} c_i + z_r c_i \vec{\nabla} \Psi). \end{aligned} \quad (\text{XVI})$$

## Appendix B – Conservation Equations in Cartesian and Cylindrical Coordinates

Mass conservation equation for incompressible flow (26):

$$\begin{aligned}\vec{\nabla} \cdot \vec{u} &= \frac{\partial u_x}{\partial x} + \frac{\partial u_y}{\partial y} + \frac{\partial u_z}{\partial z} = 0 \\ \vec{\nabla} \cdot \vec{u} &= \frac{\partial u_r}{\partial r} + \frac{u_r}{r} + \frac{1}{r} \frac{\partial u_\theta}{\partial \theta} + \frac{\partial u_z}{\partial z} = 0.\end{aligned}\tag{XVII}$$

Components of momentum conservation vector equation (27) in Cartesian form:

$$\begin{aligned}\rho \left( \frac{\partial u_x}{\partial t} + u_x \frac{\partial u_x}{\partial x} + u_y \frac{\partial u_x}{\partial y} + u_z \frac{\partial u_x}{\partial z} \right) &= -\frac{\partial P}{\partial x} + \eta \left( \frac{\partial^2 u_x}{\partial x^2} + \frac{\partial^2 u_x}{\partial y^2} + \frac{\partial^2 u_x}{\partial z^2} \right) + F_x \\ \rho \left( \frac{\partial u_y}{\partial t} + u_x \frac{\partial u_y}{\partial x} + u_y \frac{\partial u_y}{\partial y} + u_z \frac{\partial u_y}{\partial z} \right) &= -\frac{\partial P}{\partial y} + \eta \left( \frac{\partial^2 u_y}{\partial x^2} + \frac{\partial^2 u_y}{\partial y^2} + \frac{\partial^2 u_y}{\partial z^2} \right) + F_y \\ \rho \left( \frac{\partial u_z}{\partial t} + u_x \frac{\partial u_z}{\partial x} + u_y \frac{\partial u_z}{\partial y} + u_z \frac{\partial u_z}{\partial z} \right) &= -\frac{\partial P}{\partial z} + \eta \left( \frac{\partial^2 u_z}{\partial x^2} + \frac{\partial^2 u_z}{\partial y^2} + \frac{\partial^2 u_z}{\partial z^2} \right) + F_z,\end{aligned}\tag{XVIII}$$

and in cylindrical form:

$$\begin{aligned}\rho \left( \frac{\partial u_r}{\partial t} + u_r \frac{\partial u_r}{\partial r} + \frac{u_\theta}{r} \frac{\partial u_r}{\partial \theta} - \frac{u_\theta^2}{r} + u_z \frac{\partial u_r}{\partial z} \right) &= \\ -\frac{\partial P}{\partial r} + \eta \left( \frac{\partial^2 u_r}{\partial r^2} + \frac{1}{r} \frac{\partial u_r}{\partial r} - \frac{u_r}{r^2} + \frac{1}{r^2} \frac{\partial^2 u_r}{\partial \theta^2} - \frac{2}{r^2} \frac{\partial u_\theta}{\partial \theta} + \frac{\partial^2 u_r}{\partial z^2} \right) + F_r \\ \rho \left( \frac{\partial u_\theta}{\partial t} + u_r \frac{\partial u_\theta}{\partial r} + \frac{u_\theta}{r} \frac{\partial u_\theta}{\partial \theta} + \frac{u_\theta u_r}{r} + u_z \frac{\partial u_\theta}{\partial z} \right) &= \\ -\frac{1}{r} \frac{\partial P}{\partial \theta} + \eta \left( \frac{\partial^2 u_\theta}{\partial r^2} + \frac{1}{r} \frac{\partial u_\theta}{\partial r} - \frac{u_\theta}{r^2} + \frac{1}{r^2} \frac{\partial^2 u_\theta}{\partial \theta^2} + \frac{2}{r^2} \frac{\partial u_r}{\partial \theta} + \frac{\partial^2 u_\theta}{\partial z^2} \right) + F_\theta \\ \rho \left( \frac{\partial u_z}{\partial t} + u_r \frac{\partial u_z}{\partial r} + \frac{u_\theta}{r} \frac{\partial u_z}{\partial \theta} + u_z \frac{\partial u_z}{\partial z} \right) &= \\ -\frac{\partial P}{\partial z} + \eta \left( \frac{\partial^2 u_z}{\partial r^2} + \frac{1}{r} \frac{\partial u_z}{\partial r} + \frac{1}{r^2} \frac{\partial^2 u_z}{\partial \theta^2} + \frac{\partial^2 u_z}{\partial z^2} \right) + F_z.\end{aligned}\tag{XIX}$$

Nernst-Planck conservation equation in Cartesian and cylindrical forms:

$$\frac{\partial c_i}{\partial t} + \frac{\partial(c_i u_x)}{\partial x} + \frac{\partial(c_i u_y)}{\partial y} + \frac{\partial(c_i u_z)}{\partial z} = D_i \left( \frac{\partial^2 c_i}{\partial x^2} + \frac{\partial^2 c_i}{\partial y^2} + \frac{\partial^2 c_i}{\partial z^2} \right) - \frac{D_i z_i e}{k_B T} \left( \frac{\partial(c_i E_x)}{\partial x} + \frac{\partial(c_i E_y)}{\partial y} + \frac{\partial(c_i E_z)}{\partial z} \right) \quad (\text{XX})$$

$$\frac{\partial c_i}{\partial t} + \frac{1}{r} \frac{\partial(c_i u_r)}{\partial r} + \frac{1}{r} \frac{\partial(c_i u_\theta)}{\partial \theta} + \frac{\partial(c_i u_z)}{\partial z} = D_i \left( \frac{\partial^2 c_i}{\partial r^2} + \frac{1}{r} \frac{\partial c_i}{\partial r} + \frac{1}{r^2} \frac{\partial^2 c_i}{\partial \theta^2} + \frac{\partial^2 c_i}{\partial z^2} \right) - \frac{D_i z_i e}{k_B T} \left[ \frac{1}{r} \frac{\partial}{\partial r} (r c_i E_r) + \frac{1}{r} \frac{\partial}{\partial \theta} (c_i E_\theta) + \frac{\partial}{\partial z} (c_i E_z) \right].$$

## Appendix C – Analytical Approach

### One Phase Couette-Poiseuille Flow – Velocity Profile

Mass conservation equation for incompressible flow:

$$\vec{\nabla} \cdot \tilde{\mathbf{u}} = \frac{\partial \tilde{u}_x}{\partial \tilde{x}} + \frac{\partial \tilde{u}_y}{\partial \tilde{y}} + \frac{\partial \tilde{u}_z}{\partial \tilde{z}} = 0. \quad (\text{XXI})$$

Considering fully developed laminar flow, the continuity equation (XXI) reduces to:

$$\frac{\partial \tilde{u}_x}{\partial \tilde{x}} = 0. \quad (\text{XXII})$$

Momentum conservation equation for a Newtonian incompressible fluid in  $x$  direction:

$$\rho \left( \frac{\partial \tilde{u}_x}{\partial \tilde{t}} + \tilde{u}_x \frac{\partial \tilde{u}_x}{\partial \tilde{x}} + \tilde{u}_y \frac{\partial \tilde{u}_x}{\partial \tilde{y}} + \tilde{u}_z \frac{\partial \tilde{u}_x}{\partial \tilde{z}} \right) = -\frac{\partial \tilde{P}}{\partial \tilde{x}} + \eta \left( \frac{\partial^2 \tilde{u}_x}{\partial \tilde{x}^2} + \frac{\partial^2 \tilde{u}_x}{\partial \tilde{y}^2} + \frac{\partial^2 \tilde{u}_x}{\partial \tilde{z}^2} \right) + \tilde{F}_x. \quad (\text{XXIII})$$

The left hand side (LHS) of this equation is canceled: the first term due to the steady state assumption, the second term due to the continuity equation (XXII), and the third and fourth terms due to the fully developed laminar flow assumption. Several terms are canceled on the right hand side (RHS) as well: the second term due to the continuity equation (XXII), the fourth term due to the 2D configuration, and the last term due to the assumption of no external body forces. The remaining terms of the momentum equation are:

$$0 = -\frac{\partial \tilde{P}}{\partial \tilde{x}} + \eta \frac{\partial^2 \tilde{u}_x}{\partial \tilde{y}^2} \quad (\text{XXIV})$$

$$\frac{\partial^2 \tilde{u}_x}{\partial \tilde{y}^2} = \frac{1}{\eta} \frac{\partial \tilde{P}}{\partial \tilde{x}}.$$

Double integration results in the velocity profile that appears in equation (68):

$$\tilde{u}_x(\tilde{y}) = \left( \frac{1}{2\eta} \frac{\partial \tilde{P}}{\partial \tilde{x}} \right) \tilde{y}^2 + c_1 \tilde{y} + c_2 = A \tilde{y}^2 + c_1 \tilde{y} + c_2. \quad (\text{XXV})$$

Substituting the BCs determined in equation (69) provides the values of the  $c_1$  and  $c_2$  constants:

$$\tilde{u}_x(\tilde{y} = 0) = 0 \quad \Rightarrow c_2 = 0$$

$$\tilde{u}_x(\tilde{y} = H) = u_{wall} \quad \Rightarrow c_1 = \frac{u_{wall}}{H} - HA, \quad (\text{XXVI})$$

so the analytical velocity profile in the fully developed flow region reads:

$$\tilde{u}_x(\tilde{y}) = A\tilde{y}^2 + \left( \frac{u_{wall}}{H} - HA \right) \tilde{y}. \quad (XXVII)$$

## Mixture Flow Through a Curved Duct – Velocity Profile

Cylindrical form of the mass conservation equation for incompressible mixture flow:

$$\vec{\nabla} \cdot \tilde{\mathbf{u}} = \frac{\partial \tilde{u}_r}{\partial \tilde{r}} + \frac{\tilde{u}_r}{\tilde{r}} + \frac{1}{\tilde{r}} \frac{\partial \tilde{u}_\theta}{\partial \tilde{\theta}} + \frac{\partial \tilde{u}_z}{\partial \tilde{z}} = 0. \quad (XXVIII)$$

Considering fully developed laminar flow, the continuity equation (XXVIII) reduces to:

$$\frac{\partial \tilde{u}_\theta}{\partial \tilde{\theta}} = 0. \quad (XXIX)$$

Momentum conservation equation for Newtonian incompressible mixture in the  $\theta$  direction:

$$\rho \left( \frac{\partial \tilde{u}_\theta}{\partial t} + \tilde{u}_r \frac{\partial \tilde{u}_\theta}{\partial \tilde{r}} + \frac{\tilde{u}_\theta}{\tilde{r}} \frac{\partial \tilde{u}_\theta}{\partial \tilde{\theta}} + \frac{\tilde{u}_\theta \tilde{u}_r}{\tilde{r}} + \tilde{u}_z \frac{\partial \tilde{u}_\theta}{\partial \tilde{z}} \right) = \quad (XXX)$$

$$- \frac{1}{\tilde{r}} \frac{\partial \tilde{P}}{\partial \tilde{\theta}} + \eta \left( \frac{\partial^2 \tilde{u}_\theta}{\partial \tilde{r}^2} + \frac{1}{\tilde{r}} \frac{\partial \tilde{u}_\theta}{\partial \tilde{r}} - \frac{\tilde{u}_\theta}{\tilde{r}^2} + \frac{1}{\tilde{r}^2} \frac{\partial^2 \tilde{u}_\theta}{\partial \tilde{\theta}^2} + \frac{2}{\tilde{r}^2} \frac{\partial \tilde{u}_r}{\partial \tilde{\theta}} + \frac{\partial^2 \tilde{u}_\theta}{\partial \tilde{z}^2} \right) + \tilde{F}_\theta.$$

LHS of this equation is canceled: the first term due to the steady state assumption, the second, fourth, and fifth terms due to the fully developed laminar flow assumption, and the third term due to the continuity equation (XXIX). Several terms are canceled in the RHS as well: fourth, fifth, and last shear stress terms due to the continuity equation (XXIX), fully developed laminar flow, and 2D configuration assumptions, respectively. Additionally, there are no external body forces. Remaining terms of the momentum equation are:

$$0 = - \frac{1}{\tilde{r}} \frac{\partial \tilde{P}}{\partial \tilde{\theta}} + \eta \left( \frac{\partial^2 \tilde{u}_\theta}{\partial \tilde{r}^2} + \frac{1}{\tilde{r}} \frac{\partial \tilde{u}_\theta}{\partial \tilde{r}} - \frac{\tilde{u}_\theta}{\tilde{r}^2} \right) \quad (XXXI)$$

$$\frac{\partial^2 \tilde{u}_\theta}{\partial \tilde{r}^2} + \frac{1}{\tilde{r}} \frac{\partial \tilde{u}_\theta}{\partial \tilde{r}} - \frac{\tilde{u}_\theta}{\tilde{r}^2} = \frac{1}{\tilde{r}\eta} \frac{\partial \tilde{P}}{\partial \tilde{\theta}} = \frac{B}{\tilde{r}}.$$

For convenience, the momentum equation can be rewritten as:

$$\frac{\partial^2 \tilde{u}_\theta}{\partial \tilde{r}^2} + \frac{1}{\tilde{r}} \frac{\partial \tilde{u}_\theta}{\partial \tilde{r}} - \frac{\tilde{u}_\theta}{\tilde{r}^2} = \frac{B}{\tilde{r}} \rightarrow y'' + \frac{1}{x} y' - \frac{1}{x^2} y = \frac{B}{x}. \quad (XXXII)$$

This is an inhomogeneous second-order linear differential equation. To solve this kind of equation, one should superpose the homogeneous equation result with a private inhomogeneous equation result:

$$y = y_h + y_p. \quad (\text{XXXIII})$$

The homogeneous form of equation (XXXII) is:

$$y_h'' + \frac{1}{x} y_h' - \frac{1}{x^2} y_h = 0 \quad (\text{XXXIV})$$

$$x^2 y_h'' + x y_h' - y_h = 0.$$

Equation (XXXIV) is a homogeneous Euler's differential equation. Proposing solutions of the form  $\varphi(x) = x^n$  we get:

$$n(n-1)x^2 \cdot x^{n-2} + nx \cdot x^{n-1} - x^n = 0 \quad /: x^n \neq 0$$

$$n(n-1) + n - 1 = 0 \quad (\text{XXXV})$$

$$n_{1,2} = \pm 1 \Rightarrow \varphi_{1,2}(x) = x^{\pm 1},$$

and the homogeneous solution becomes:

$$y_h = c_1 \varphi_1(x) + c_2 \varphi_2(x) = c_1 x + c_2 \frac{1}{x}. \quad (\text{XXXVI})$$

Solution via variation of parameters approach:

$$y = C_1(x) \varphi_1(x) + C_2(x) \varphi_2(x). \quad (\text{XXXVII})$$

To find  $C_1(x)$ ,  $C_2(x)$  one should solve the following system of equations:

$$C_1'(x) \varphi_1(x) + C_2'(x) \varphi_2(x) = 0 \quad (\text{XXXVIII})$$

$$C_1'(x) \varphi_1'(x) + C_2'(x) \varphi_2'(x) = f(x),$$

where  $f(x)$  is the inhomogeneous term of the original equation (XXXII). Using Cramer's rule:

$$\begin{aligned}
C_1'(x) &= \frac{\det \begin{pmatrix} 0 & \varphi_2(x) \\ f(x) & \varphi_2'(x) \end{pmatrix}}{\det \begin{pmatrix} \varphi_1(x) & \varphi_2(x) \\ \varphi_1'(x) & \varphi_2'(x) \end{pmatrix}} = \frac{\det \begin{pmatrix} 0 & \varphi_2(x) \\ f(x) & \varphi_2'(x) \end{pmatrix}}{W(\varphi_1, \varphi_2; x)} = -\frac{f(x)\varphi_2(x)}{W(\varphi_1, \varphi_2; x)} \\
C_2'(x) &= \frac{\det \begin{pmatrix} \varphi_1(x) & 0 \\ \varphi_1'(x) & f(x) \end{pmatrix}}{\det \begin{pmatrix} \varphi_1(x) & \varphi_2(x) \\ \varphi_1'(x) & \varphi_2'(x) \end{pmatrix}} = \frac{\det \begin{pmatrix} \varphi_1(x) & 0 \\ \varphi_1'(x) & f(x) \end{pmatrix}}{W(\varphi_1, \varphi_2; x)} = \frac{f(x)\varphi_1(x)}{W(\varphi_1, \varphi_2; x)},
\end{aligned} \tag{XXXIX}$$

where  $W(\varphi_1, \varphi_2; x)$  is the Wronskian of  $\varphi_1(x)$  and  $\varphi_2(x)$  solutions. After integration,  $C_1(x)$  and  $C_2(x)$  are obtained as:

$$\begin{aligned}
C_1(x) &= c_1 - \int \frac{f(x)\varphi_2(x)}{W(\varphi_1, \varphi_2; x)} dx \\
C_2(x) &= c_2 + \int \frac{f(x)\varphi_1(x)}{W(\varphi_1, \varphi_2; x)} dx.
\end{aligned} \tag{XL}$$

For the current parameters:

$$\begin{aligned}
W(\varphi_1, \varphi_2; x) &= \varphi_2' \varphi_1 - \varphi_1' \varphi_2 = -\frac{1}{x^2} \cdot x - 1 \cdot \frac{1}{x} = -\frac{2}{x} \\
C_1(x) &= c_1 - \int \frac{\frac{B}{x} \cdot \frac{1}{x}}{-\frac{2}{x}} dx = c_1 + \frac{B}{2} \ln x \\
C_2(x) &= c_2 + \int \frac{\frac{B}{x} \cdot x}{-\frac{2}{x}} dx = c_2 - \frac{Bx^2}{4}.
\end{aligned} \tag{XLI}$$

Substituting equation (XLI) into equation (XXXVII), we obtain a result analogous to that introduced by equation (71):

$$y = \left( c_1 + \frac{B}{2} \ln x \right) \cdot x + \left( c_2 - \frac{Bx^2}{4} \right) \cdot \frac{1}{x} = \underbrace{c_1 x + \frac{c_2}{x}}_{y_h} + \underbrace{\frac{Bx}{2} \left( \ln x - \frac{1}{2} \right)}_{y_p}. \tag{XLII}$$

Substituting the BCs (72):

$$\begin{aligned}
\tilde{u}_\theta(\tilde{r} = r_1) &= u_{\theta\_wall} \Rightarrow y(x = x_1) = y_{wall} \\
\tilde{u}_\theta(\tilde{r} = r_2) &= 0 \Rightarrow y(x = x_2) = 0
\end{aligned} \tag{XLIII}$$

into equation (XLII), the following system of equations is obtained:

$$y_{wall} = c_1 x_1 + \frac{c_2}{x_1} + \frac{Bx_1}{2} \left( \ln x_1 - \frac{1}{2} \right) \quad (\text{XLIV})$$

$$0 = c_1 x_2 + \frac{c_2}{x_2} + \frac{Bx_2}{2} \left( \ln x_2 - \frac{1}{2} \right),$$

and by solving this system of equations:

$$c_1 = \frac{-2y_{wall}x_1^2 - Bx_1 \left[ (x_2^2 - x_1^2) \left( \ln x_1 - \frac{1}{2} \right) + x_2^2 (\ln x_2 - \ln x_1) \right]}{2x_1(x_2^2 - x_1^2)} \quad (\text{XLV})$$

$$c_2 = \frac{2y_{wall}x_1x_2^2 + Bx_1^2x_2^2 (\ln x_2 - \ln x_1)}{2(x_2^2 - x_1^2)}.$$

Substituting these constants into equation (XLII) and performing several algebraic operations:

$$y(x) = \frac{Bx^2 \left[ x_2^2 \ln \left( \frac{x}{x_2} \right) - x_1^2 \ln \left( \frac{x}{x_1} \right) \right] + Bx_1^2x_2^2 \ln \left( \frac{x_2}{x_1} \right) + 2y_{wall}x_1(x_2^2 - x^2)}{2x(x_2^2 - x_1^2)}, \quad (\text{XLVI})$$

which corresponds to the analytical mixture velocity profile obtained for the fully developed region (see equation (73)):

$$\tilde{u}_\theta(\tilde{r}) = \frac{B\tilde{r}^2 \left[ r_2^2 \ln \left( \frac{\tilde{r}}{r_2} \right) - r_1^2 \ln \left( \frac{\tilde{r}}{r_1} \right) \right] + Br_1^2r_2^2 \ln \left( \frac{r_2}{r_1} \right) + 2u_{\theta\_wall}r_1(r_2^2 - \tilde{r}^2)}{2\tilde{r}(r_2^2 - r_1^2)}. \quad (\text{XLVII})$$

## Mixture Flow Through a Curved Duct Without the Action of an Electric Field – Particles Concentration Profile

As stated before, the continuity equation for this case is given by equation (XXIX). Fick's law of diffusion for the solid particle species in cylindrical coordinates:

$$\frac{\partial \tilde{c}_s}{\partial \tilde{t}} + \frac{1}{\tilde{r}} \frac{\partial (\tilde{u}_r \tilde{c}_s)}{\partial \tilde{r}} + \frac{1}{\tilde{r}} \frac{\partial (\tilde{u}_\theta \tilde{c}_s)}{\partial \tilde{\theta}} + \frac{\partial (\tilde{u}_z \tilde{c}_s)}{\partial \tilde{z}} = D_s \left( \frac{\partial^2 \tilde{c}_s}{\partial \tilde{r}^2} + \frac{1}{\tilde{r}} \frac{\partial \tilde{c}_s}{\partial \tilde{r}} + \frac{1}{\tilde{r}^2} \frac{\partial^2 \tilde{c}_s}{\partial \tilde{\theta}^2} + \frac{\partial^2 \tilde{c}_s}{\partial \tilde{z}^2} \right). \quad (\text{XLVIII})$$

The LHS of this equation is canceled: the first term due to the steady state assumption, the second and fourth terms due to the fully developed laminar flow assumption, and the third term is rewritten as:



$$\frac{1}{\tilde{r}} \frac{\partial(\tilde{u}_\theta \tilde{c}_s)}{\partial \tilde{\theta}} = \frac{1}{\tilde{r}} \left[ \tilde{u}_\theta \frac{\partial \tilde{c}_s}{\partial \tilde{\theta}} + \tilde{c}_s \frac{\partial \tilde{u}_\theta}{\partial \tilde{\theta}} \right], \quad (\text{XLIX})$$

while the first term in the RHS of equation (XLIX) is canceled due to the fully developed flow assumption and the second due to the continuity equation (XXIX). The third and fourth terms in the RHS of equation (XLVIII) are canceled due to the fully developed laminar flow assumption. Remaining terms of the particle species conservation equation are:

$$0 = D_s \left( \frac{\partial^2 \tilde{c}_s}{\partial \tilde{r}^2} + \frac{1}{\tilde{r}} \frac{\partial \tilde{c}_s}{\partial \tilde{r}} \right) \quad (\text{L})$$

$$\frac{\partial^2 \tilde{c}_s}{\partial \tilde{r}^2} + \frac{1}{\tilde{r}} \frac{\partial \tilde{c}_s}{\partial \tilde{r}} = 0.$$

For convenience, the concentration equation can be rewritten as:

$$\frac{\partial^2 \tilde{c}_s}{\partial \tilde{r}^2} + \frac{1}{\tilde{r}} \frac{\partial \tilde{c}_s}{\partial \tilde{r}} = 0 \quad \rightarrow \quad y'' + \frac{1}{x} y' = 0 \quad (\text{LI})$$

$$x^2 y'' + xy' = 0.$$

This is a homogeneous Euler's differential equation. Proposing solutions of the form  $\varphi(x) = x^n$  we get:

$$n(n-1)x^2 \cdot x^{n-2} + nx \cdot x^{n-1} = 0 \quad /: x^n \neq 0$$

$$n(n-1) + n = 0 \quad (\text{LII})$$

$$n_{1,2} = 0 \quad \Rightarrow \quad \varphi_1(x) = \ln x, \quad \varphi_2(x) = 1,$$

and the solution becomes:

$$y(x) = a_1 \ln x + a_2 \quad (\text{LIII})$$

which is analogous to equation (74). Substituting the BCs (75):

$$\frac{\partial \tilde{c}_s}{\partial \tilde{r}}(\tilde{r} = r_1) = 0 \quad \rightarrow \quad \frac{\partial y}{\partial x}(x = x_1) = 0 \quad (\text{LIV})$$

$$\frac{\partial \tilde{c}_s}{\partial \tilde{r}}(\tilde{r} = r_2) = 0 \quad \rightarrow \quad \frac{\partial y}{\partial x}(x = x_2) = 0$$

into equation (LIII), solution (76) is obtained:

$$y = a_2 \quad \rightarrow \quad \tilde{c}_s = \text{const}, \quad (\text{LV})$$

which means that the particle species concentration gets a constant value and does not depend on the radial coordinate.

## Approximated Expression of the Electric Field Vector

Gauss's law states that "the net electric flux through any hypothetical closed surface is equal to  $1/\epsilon_0$  times the net electric charge within that closed surface" [83]:

$$\tilde{\Phi} = \oint_{\tilde{A}} \tilde{\vec{E}} \cdot \hat{n} d\tilde{A} = \frac{\tilde{Q}_{in}}{\epsilon_0}. \quad (\text{LVI})$$

Utilizing this integral form of Gauss's law for a curved channel, with internal boundary radius  $r_1$  and external boundary radius  $r_2$  concentric to each other, requires a complete cylinder perimeter assumption for the internal boundary. Such conditions enable generation of a symmetric Gaussian surface around the cylinder, as shown in figure I:

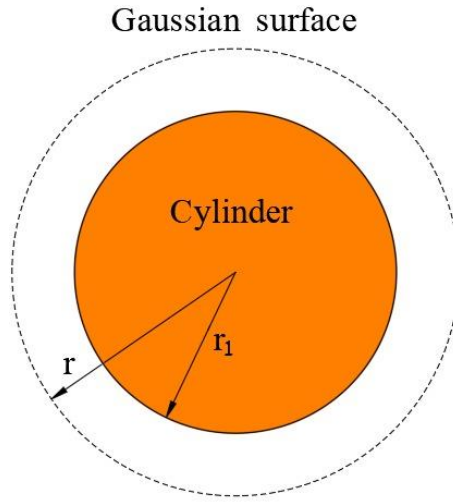


Figure I: A Gaussian surface around a complete cylinder.

Considering constant charge density (electric charge per unit length)  $\tilde{\lambda}$  on the cylinder perimeter:

$$\tilde{\lambda} = \frac{\tilde{Q}_{in}}{2\pi r_1} \left[ \frac{\text{C}}{\text{m}} \right], \quad (\text{LVII})$$

the direction of electric field lines is radial, perpendicular to the Gaussian surface. Substitution of the previous relations into equation (LVI) yields:

$$\begin{aligned} \tilde{\vec{E}}_r \cdot 2\pi\tilde{r} &= \frac{\tilde{\lambda} \cdot 2\pi r_1}{\epsilon_0} \\ \tilde{\vec{E}}_r(\tilde{r}) &= \frac{\tilde{\lambda} r_1}{\epsilon_0 \tilde{r}} \rightarrow \tilde{\lambda} = \frac{\epsilon_0 \tilde{r} \tilde{\vec{E}}_r}{r_1}. \end{aligned} \quad (\text{LVIII})$$

Integrating equation (30) over the radial coordinate yields:

$$\tilde{V}(\tilde{r}) = -\int \tilde{E}_r(\tilde{r}) d\tilde{r}, \quad (\text{LIX})$$

where  $\tilde{V}$  relates to voltage. The electric potential difference  $\Delta V$  between  $r_1$  and  $r_2$  is obtained as:

$$\Delta V = -\int_{r_2}^{r_1} \frac{\tilde{\lambda} r_1}{\varepsilon_0 \tilde{r}} d\tilde{r} = \frac{\tilde{\lambda} r_1}{\varepsilon_0} \ln\left(\frac{r_2}{r_1}\right). \quad (\text{LX})$$

Substituting the charge density expression presented in equation (LVIII) into equation (LX) yields:

$$\begin{aligned} \Delta V &= \frac{\tilde{\lambda} r_1}{\varepsilon_0} \ln\left(\frac{r_2}{r_1}\right) = \frac{\varepsilon_0 \tilde{r} \tilde{E}_r}{r_1} \cdot \frac{r_1}{\varepsilon_0} \ln\left(\frac{r_2}{r_1}\right) = \tilde{r} \tilde{E}_r \ln\left(\frac{r_2}{r_1}\right) \\ \tilde{E}_r(\tilde{r}) &= \frac{\Delta V}{\tilde{r} \ln\left(\frac{r_2}{r_1}\right)}, \end{aligned} \quad (\text{LXI})$$

so the obtained electric field vector is equal to the expression given in equation (78):

$$\tilde{\vec{E}}(\tilde{r}) = \frac{\Delta V}{\tilde{r} \ln\left(\frac{r_2}{r_1}\right)} \hat{r}. \quad (\text{LXII})$$

Note that this approach corresponds with the charge density of the approximated inner boundary only, without the influence of charged species within the mixture.

## Mixture Flow Through a Curved Duct Under the Action of Constant Approximated Electric Field – Particles Concentration Profile

As stated before, the continuity equation for this case is given by equation (XXIX). In the absence of magnetic potential, the cylindrical form of the Nernst-Planck equation (XX) for the particle species yields:

$$\begin{aligned} \frac{\partial \tilde{c}_s}{\partial \tilde{t}} + \frac{1}{\tilde{r}} \frac{\partial(\tilde{u}_r \tilde{c}_s)}{\partial \tilde{r}} + \frac{1}{\tilde{r}} \frac{\partial(\tilde{u}_\theta \tilde{c}_s)}{\partial \tilde{\theta}} + \frac{\partial(\tilde{u}_z \tilde{c}_s)}{\partial \tilde{z}} &= D_s \left( \frac{\partial^2 \tilde{c}_s}{\partial \tilde{r}^2} + \frac{1}{\tilde{r}} \frac{\partial \tilde{c}_s}{\partial \tilde{r}} + \frac{1}{\tilde{r}^2} \frac{\partial^2 \tilde{c}_s}{\partial \tilde{\theta}^2} + \frac{\partial^2 \tilde{c}_s}{\partial \tilde{z}^2} \right) \\ &\quad - \frac{D_s z_s e}{k_B T} \left[ \frac{1}{\tilde{r}} \frac{\partial}{\partial \tilde{r}} (\tilde{r} \tilde{c}_s \tilde{E}_r) + \frac{1}{\tilde{r}} \frac{\partial}{\partial \tilde{\theta}} (\tilde{c}_s \tilde{E}_\theta) + \frac{\partial}{\partial \tilde{z}} (\tilde{c}_s \tilde{E}_z) \right]. \end{aligned} \quad (\text{LXIII})$$

For the same reasons as in the previous section, the LHS of equation (LXIII), as well as the third and fourth terms on the RHS, are canceled. Also, the last two terms on the RHS are canceled as the electric field vector introduced in equation (LXII) addresses only a radial component. Remaining terms of the Nernst-Planck equation are:

$$0 = D_s \left( \frac{\partial^2 \tilde{c}_s}{\partial \tilde{r}^2} + \frac{1}{\tilde{r}} \frac{\partial \tilde{c}_s}{\partial \tilde{r}} \right) - \frac{D_s z_s e}{k_B T} \left[ \frac{1}{\tilde{r}} \frac{\partial}{\partial \tilde{r}} \left( \tilde{r} \tilde{c}_s \cdot \frac{\Delta V}{\tilde{r} \ln \left( \frac{r_2}{r_1} \right)} \right) \right] \quad (\text{LXIV})$$

$$\frac{\partial^2 \tilde{c}_s}{\partial \tilde{r}^2} + \frac{1-G}{\tilde{r}} \frac{\partial \tilde{c}_s}{\partial \tilde{r}} = 0 \quad ; \quad G \equiv \frac{z_s e \Delta V}{k_B T \ln \left( \frac{r_2}{r_1} \right)}.$$

For convenience, the concentration equation can be rewritten as:

$$\frac{\partial^2 \tilde{c}_s}{\partial \tilde{r}^2} + \frac{1-G}{\tilde{r}} \frac{\partial \tilde{c}_s}{\partial \tilde{r}} = 0 \quad \rightarrow \quad y'' + \frac{1-G}{x} y' = 0 \quad (\text{LXV})$$

$$x^2 y'' + (1-G) x y' = 0.$$

This is a homogeneous Euler's differential equation. Proposing solutions of the form  $\varphi(x) = x^n$  we get:

$$n(n-1)x^2 \cdot x^{n-2} + n(1-G)x \cdot x^{n-1} = 0 \quad /: x^n \neq 0$$

$$n(n-1) + n(1-G) = 0 \quad (\text{LXVI})$$

$$n(n-G) = 0$$

$$n_1 = G, \quad n_2 = 0 \quad \Rightarrow \quad \varphi_1(x) = x^G, \quad \varphi_2(x) = 1,$$

and the solution becomes:

$$y(x) = a_1 x^G + a_2 \quad (\text{LXVII})$$

which is analogous to equation (79). Substituting the BCs (80):

$$\tilde{c}_s(\tilde{r} = r_1) = c_{\max} \quad \Rightarrow \quad y(x = x_1) = y_{\max} \quad (\text{LXVIII})$$

$$\tilde{c}_s(\tilde{r} = r_2) = 0 \quad \Rightarrow \quad y(x = x_2) = 0$$

into equation (LXVII), the following system of equations is obtained:

$$y_{\max} = a_1 x_1^G + a_2 \quad (\text{LXIX})$$

$$0 = a_1 x_2^G + a_2,$$

and by solving this system of equations:

$$a_1 = \frac{y_{\max}}{x_1^G - x_2^G} \quad ; \quad a_2 = -\frac{y_{\max} x_2^G}{x_1^G - x_2^G}. \quad (\text{LXX})$$

Substituting these constants into equation (LXVII) and performing several algebraic operations:

$$y(x) = \frac{y_{\max} (x^G - x_2^G)}{(x_1^G - x_2^G)}, \quad (\text{LXXI})$$

which corresponds to the analytical particles concentration profile obtained for the fully developed region (see equation (81)):

$$\tilde{c}_s(\tilde{r}) = \frac{c_{\max} (\tilde{r}^G - r_2^G)}{(r_1^G - r_2^G)}. \quad (\text{LXXII})$$

Author's e-mail address: [Arnonr@post.bgu.ac.il](mailto:Arnonr@post.bgu.ac.il)

## תקציר

מטרת מסמך זה הינה הצגת סיכום העבודה אשר בוצעה במסגרת הדרוש להשלמת תואר מגיסטר בהנדסה (M.Sc.) במחלקה להנדסת מכונות, אוניברסיטת בן-גוריון בנגב. בעבודה זו בוצע מחקר תאורטי הנוגע לזרימה רב-פאזית של חלקיקי מוצק טעונים המצויים באלקטרוליט הנתון לשדה חשמלי. המוטיבציה למחקר זה מגיעה מהתגלותן של מספר בעיות איכות הדפסה במהלך פעולתן של מדפסות לייזר המיוצרות ע"י חברת HP Indigo. עבודה זו מהווה המשך לפרויקט של מיכאל חגיב [1] אשר כלל סקר ספרות, הצעת מודל פיזיקלי מפורט, והרצת מספר סימולציות נומריות המתארות את הדינמיקה של זורם חד-פאזי אשר איננו טעון חשמלית.

יעדה המרכזי של העבודה הנוכחית הינו פיתוח מתודולוגיה נומרית רחבה המאפשרת מידול תאורטי של זרימה רב-פאזית בהשפעת שדה חשמלי, זאת באמצעות טכניקות סטנדרטיות מתחום המדע החישובי בזרימה. שיתוף הפעולה בין חברת HP Indigo לאוניברסיטת בן-גוריון עתיד להימשך גם בשנה העוקבת לפרסום תזה זו.

דוח זה כולל:

- רקע מודולרי הנוגע לרכיבי חברת HP Indigo הרלוונטיים למחקר הנוכחי.
- סקר ספרות נרחב הכולל גישות לפתרון בעיות זרימה רב-פאזיות ומודלים לתנועת זורם ע"י כוחות חשמליים. כמו כן, כולל סקר הספרות רקע תאורטי הנוגע לתופעות הפיזיקליות האופייניות באלקטרוליט המצוי תחת השפעת מפל מתח.
- הרחבה על מטרות המחקר.
- מודל פיזיקלי נרחב הכולל את המשוואות המצומדות השולטות בבעיה הפיזיקלית, הגדרות, משוואות מצב ואנליזה מימדית.
- השוואה בין פתרונות אנליטיים לתוצאות סימולציות נומריות דו-מימדיות עבור מודל פיזיקלי מפורט. התוצאות מתמקדות בזרימת קוואט-פואסי לזורם חד-פאזי, זרימה דו-פאזית של פאזות לא טעונות חשמלית, וזרימה דו-פאזית המכילה חלקיקים טעונים תחת השפעת שדה חשמלי קבוע.
- פתרון המודל הפיזיקלי המלא (הכולל משוואות מצומדות) באמצעות תוכנות זרימה חישוביות, ביצוע וריפיקציה, ואפיון זרימה של אלקטרוליט לא סימטרי המונע באמצעות כוחות חשמליים.
- מודל פיזיקלי הרלוונטי לנתוני מדפסות הלייזר של חברת HP Indigo: מימדים גיאומטריים, נתונים מספריים, הנחות ותוצאות סימולציות נומריות.
- סיכום, מסקנות והמלצות להמשך עבודה עתידי.

למילות מפתח בתזה ראה תקציר בשפה האנגלית המופיע בתחילת מסמך זה.

אוניברסיטת בן-גוריון בנגב

הפקולטה למדעי ההנדסה

המחלקה להנדסת מכונות



זרימת נוזל וחלקיקים טעונים בהשפעת שדה

חשמלי

חיבור זה מהווה חלק מהדרישות לקבלת תואר מגיסטר בהנדסה

מאת : ארנון רצבי

מנחים : פרופ' אבי לוי


ד"ר יורי פלדמן

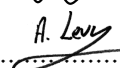
תאריך : 30/9/2020

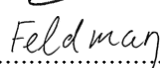
תאריך : 30/9/2020

תאריך : 30/9/2020

תאריך : 30/9/2020

..... חתימת המחבר : 

..... אישור המנחים : 

..... 

..... אישור יו"ר ועדת תואר שני מחלקתית :

ספטמבר 2020